

# X-ray fluorescence imaging: experimental and numerical analysis of a crystal based concept

Dissertation

zur Erlangung des akademischen Grades

**doctor rerum naturalium (Dr. rer. nat.)**

genehmigt durch die Fakultät für Naturwissenschaften der  
Otto-von-Guericke-Universität Magdeburg

von M.Sc. Tanja Rosentreter  
geboren am 26.12.1985 in Dernbach

Gutachter: Prof. Dr. Christoph Hoeschen  
Prof. Dr. Birgit Kanngießner

eingereicht am: 13.06.2020  
verteidigt am: 09.02.2021



## Zusammenfassung

Hintergrund und Ziele: Diagnostische Bildgebung auf Basis von Röntgenfluoreszenz (XRF für *X-ray fluorescence*) ist ein nicht-invasives bildgebendes Verfahren welches sowohl molekulare als auch morphologische Bildinformationen liefern kann. Mit geringen Mengen an Kontrastmittel soll die Detektorempfindlichkeit und die räumliche Auflösung verbessert werden, was für den Bereich der vorklinischen Forschung von besonderem Interesse ist. Um die Sensitivität und Auflösung zu erhöhen müssen jedoch noch lange Scanzeiten in Kauf genommen werden, die auf die üblicherweise geringen Detektorflächen zurückzuführen sind, welche nur einen geringen Raumwinkelanteil des isotropisch emittierten XRF-Signals einfangen können. Eine weitere Beeinträchtigung stellt der hohe Anteil an einfach- und mehrfachgestreuten Hintergrundphotonen im resultierenden XRF-Spektrum dar, welche mit steigender Phantomgröße (Phantom: speziell hergestellter *Prüfkörper* zur Überprüfung der Leistung von bildegebenden Instrumenten) das XRF-Signal zunehmend überdeckt. Beide Defizite können deutlich verringert werden, indem monochromatische Röntgenstrahlung verwendet wird, so wie sie von Synchrotrons bereitgestellt wird. Diese sind jedoch mit hohen Kosten und einem nur begrenzten Zugang verbunden. Andere Herangehensweisen, um die oben genannten Probleme zu lösen, konzentrieren sich primär auf die Verbesserung der Systeme zur Detektion/Rekonstruktion und die Entwicklung neuer geeigneter monochromatischer Röntgenquellen. Die vorliegende Arbeit widmet sich den genannten Problemen mit den vorhandenen Mitteln einer industriellen polychromatischen Röntgenröhre und einem energieaufgelösten Röntgendetektor. Ziel ist es, großflächige Detektoren (großer Raumwinkel) mit reduzierter Energieauflösung zusammen mit energieselektierenden HOPG/HAPG Kristallen (Reduktion von kontaminierenden Hintergrundphotonen) mit intrinsischer Mosaizität hinsichtlich ihrer Anwendbarkeit in der XRF-Bildgebung zu untersuchen.

Materialien und Methoden: Zur Untersuchung der XRF-Bildgebung wurde ein experimenteller Aufbau mit folgenden Elementen entworfen: Industrielle polychromatische Röntgenquelle, HOPG Kristall (Mosaizität:  $0,4^\circ$ ), kleinflächiger CdTe-basierter Detektor mit hoher Energieauflösung und einer Bingröße von ca. 86 eV, und Jod als Kontrastmittel, mit  $K_\alpha$ -Emissionslinie bei etwa 28,6 keV. Für die Durchführung einer Messserie mit/ohne HOPG wurde ein einfaches Teströhrchen-Phantom und ein PMMA-Phantom in der Größe einer Maus verwendet, welche mit mehreren Kontrastmittelkonzentrationen befüllt wurden. Die Verteilung der Hintergrundphotonen wurde mit einem zusätzlichen Phantom gemessen und die zugeführte Röntgendosis (Luftkerma) wurde mit zwei Ionisationskammern erfasst. Um die resultierenden XRF-Spektren von fehlerhaften Anteilen, die von Detektoreffekten herrühren, zu bereinigen, wurde ein umfangreicher Korrekturalgorithmus (*stripping algorithm*) entwickelt und angewendet. Die experimentellen Ergebnisse wurden mit einem XRF-Monte-Carlo-Code, welcher mit GEANT4 entwickelt wurde, simuliert und validiert. Weitere Effekte, die die Mosaizität des Kristalls und die Detektor-Charakteristika berücksichtigen, wurden mithilfe eines weiteren Korrekturalgorithmus realisiert. Der XRF-Code wurde außerdem verwendet, um den Einfluss auf das XRF-Signal durch Detektorgröße, Bingröße, intrinsische Energieauflösung und Kristall-Mosaizität zu untersuchen.

Ergebnisse und Schlussfolgerungen: Der Einsatz von energiewählenden HOPG/HAPG Kristallen in ein System zur XRF-Bildgebung bewirkt, dass der Energiebereich des XRF-Signals im resultierenden Spektrum hervorgehoben wird, während die übrigen Energiebereiche unterdrückt werden. Für große Binngößen ist das Verhältnis von XRF-Signal zu Streuuntergrund unter Einsatz des HOPGs gegenüber dem Setup ohne Kristall deutlich verbessert. Selbst bei reduzierter intrinsischer Energieauflösung, welche mit einer Verringerung des XRF-Signals einhergeht, liefert ein Setup mit HOPG-Kristall bei großen Binngößen bessere Ergebnisse, als ein Setup ohne HOPG-Kristall. Zusätzlich wird das XRF-Signal durch den Einsatz von HOPG/HAPG-Kristallen mit noch geringeren Mosaizitäten verstärkt. Demnach ermöglicht die Verwendung von HOPG/HAPG Kristallen den Einsatz von Detektoren mit reduzierter Energieauflösung und großen Binngößen für die XRF-Bildgebung. Die Übertragung dieser Ergebnisse auf tomographische bildgebende Methoden würde es ermöglichen, Bilder zu generieren, welche nicht nur geometrische, sondern auch molekulare Strukturen abbilden könnten. Des Weiteren würde die Strahlzeit und demnach auch die zugeführte Röntgendosis signifikant reduziert, was den Weg dafür ebnet, großflächige Detektoren für *in vivo* diagnostische XRF-Bildgebung einzusetzen.

---

## Summary

Background and aim: Diagnostic imaging based on X-ray fluorescence (XRF) is a non-invasive imaging technique with the capability to provide molecular and morphological information with very low tracer concentrations (nanoparticles; NPs) and high spatial resolution and is thus of great interest in preclinical research. However, in order to further increase the detector sensitivity and spatial resolution, XRF imaging still requires unacceptably large irradiation times and/or high tracer contrast agent concentrations. The reason for this is the small sensitive area of suitable XRF detectors that only cover a minimum fraction of the solid angle of the isotropically emitted XRF signal. Also, contaminating single or multiple scattered background photons in the resulting XRF spectrum hide the XRF signal. The larger the phantom size (phantom: a specially designed object used for performance tests of various imaging devices), the more spurious photons deteriorate the XRF signal yield. Both deficiencies can be considerably reduced by implementing monochromatic initial X-radiation such as provided by synchrotron facilities, which however are impractical for diagnostic and therapeutic approaches in daily medical practice due to their high costs and limited access. Other approaches aiming to reduce the radiation dose while maintaining high sensitivity and resolution images predominantly focus on improving the detection/reconstruction system or on advancing the research for generating new suitable and accessible monochromatic X-ray sources. This thesis tackles the above-mentioned challenges by using the existing resources of polychromatic X-rays and an energy resolved X-ray detector. The aim is to investigate the feasibility of XRF imaging of large area detectors (large angular coverage) with moderate energy resolution together with an energy-selective filtering system (reduction of spurious background photons) of mosaic HOPG/HAPG crystals.

Materials and Methods: A proof-of-principle XRF imaging setup was developed using an industrial polychromatic X-ray source, an HOPG crystal with  $0.4^\circ$  mosaicity, a small area semiconductor CdTe-based detector with high energy resolution and bin size of  $\approx 86$  keV, and iodine as contrast agent with a  $K_\alpha$  emission line at  $\approx 28.6$  keV. A series of XRF measurements with/without HOPG with a simple test tube phantom and a mouse sized PMMA phantom was conducted using various contrast agent concentrations. The background photon distribution was studied with an additional PMMA phantom and the applied X-ray dose (air kerma) was recorded with two ionisation chambers. For cleansing the XRF spectra from spurious counts due to detector effects, a comprehensive spectrum correction *stripping algorithm* was developed and applied. The experimental findings were simulated and validated with an XRF Monte Carlo code developed with GEANT4. Additional effects accounting for crystal mosaicity and realistic detector characteristics were realised in a supplementary spectrum correction code. The XRF code was further promoted in order to scrutinise the influence on the XRF signal of detector size, bin size, intrinsic energy resolution, and crystal mosaicity.

Results and Conclusion: Implementing energy-selecting mosaic HOPG/HAPG crystals in an XRF imaging setup, elevates the energy region of interest (XRF signal region) and suppresses all other energy regions in the resulting XRF spectra. The consider-

able reduction of spurious background photons thus relaxes the high demands on the detection system in terms of intrinsic energy resolution and bin size. In particular for large bin sizes the HOPG substantially outperforms an imaging setup without mosaic crystal. A decrease in the energy resolution correlates with a decline of the XRF signal yield, which however for large bin sizes still shows better results in a setup including the crystal than for a setup omitting it. Implementing HOPG/HAPG crystals with lower mosaicities further significantly improves the XRF signal yield. Mosaic crystals therefore facilitate the application of large area detectors with reduced intrinsic energy resolution and large bin sizes in the framework of XRF imaging. Integrating these findings into tomographic imaging methods would generate images with geometrical and molecular features. Moreover, the irradiation time and consequently the applied X-ray dose could be considerably reduced, thus paving the way for *in vivo* diagnostic XRF imaging.

# Contents

<b>Introduction</b>	<b>1</b>
<b>Structure and outline of this thesis</b>	<b>5</b>
<b>I Fundamentals of diagnostic X-ray spectroscopy</b>	<b>7</b>
<b>1 Generation of X-rays for diagnostic imaging</b>	<b>11</b>
1.1 X-ray tubes . . . . .	11
1.2 Radioisotopic sources . . . . .	15
1.3 Synchrotron radiation sources . . . . .	15
<b>2 Interaction of X-rays with matter</b>	<b>18</b>
2.1 Rayleigh scattering . . . . .	19
2.2 Compton scattering . . . . .	20
2.3 Photoelectric effect . . . . .	21
<b>3 Detection of X-rays and detector characteristics</b>	<b>24</b>
3.1 Basic properties of X-ray detectors for XRF imaging . . . . .	24
3.1.1 Detector sensitivity and detector response function . . . . .	25
3.1.2 Detection efficiency . . . . .	25
3.1.3 Energy resolution . . . . .	27
3.1.4 Dead time . . . . .	29
3.2 Common X-ray detectors . . . . .	30
3.2.1 Gas detectors . . . . .	30
3.2.2 Scintillation detectors . . . . .	31
3.2.3 Semiconductor detectors . . . . .	31
<b>4 X-ray diffraction optics and mosaic crystals</b>	<b>34</b>

4.1	Bragg diffraction of mosaic crystals . . . . .	35
4.2	Physical and geometrical properties of HOPG/HAPG . . . . .	36
<b>5</b>	<b>Data processing and analysis</b>	<b>38</b>
5.1	Fitting of XRF signal and background . . . . .	38
5.2	Signal-to-noise ratio (SNR) . . . . .	39
<b>II</b>	<b>Experimental investigation</b>	<b>41</b>
<b>6</b>	<b>Materials and methods</b>	<b>45</b>
6.1	Experimental setup . . . . .	45
6.1.1	X-ray source and spectrum . . . . .	46
6.1.2	Phantoms . . . . .	49
6.1.3	HOPG crystal . . . . .	49
6.1.4	CdTe semiconductor detection system . . . . .	50
6.2	X-ray dose measurement and estimation . . . . .	52
6.2.1	Dose measurement with ionisation chamber . . . . .	52
6.2.2	Dose estimation via calculation with SpekCalc . . . . .	54
6.3	Spectrum correction methods . . . . .	55
6.3.1	The stripping algorithm . . . . .	55
<b>7</b>	<b>Results: measurements of X-ray spectra</b>	<b>59</b>
7.1	Preliminary measurements with various beam qualities . . . . .	59
7.1.1	Influence of applied high voltage $U_A$ . . . . .	59
7.1.2	Influence of X-ray tube filtering . . . . .	64
7.1.3	Influence of angular detector configuration . . . . .	67
7.2	Measurements of various iodine concentrations . . . . .	68
7.2.1	PMMA/mouse phantom (phantom 2) . . . . .	69
7.2.2	Eppendorf phantom (phantom 1) . . . . .	70
7.3	Air kerma measurements with ionisation chambers . . . . .	73
<b>III</b>	<b>Monte Carlo simulation GEANT4</b>	<b>75</b>
<b>8</b>	<b>Introduction to the GEANT4 toolkit</b>	<b>79</b>
8.1	The Monte Carlo method in GEANT4 . . . . .	79



---

8.2	Structure, design and architecture of GEANT4 . . . . .	80
8.2.1	Geometry and materials . . . . .	81
8.2.2	Particles and their interaction with matter . . . . .	81
8.2.3	Tracking and event generation . . . . .	82
8.2.4	Detector - hits and digits . . . . .	82
8.2.5	User interface and visualisation . . . . .	82
8.2.6	Data analysis . . . . .	83
8.3	(Pseudo) random number generator (PRNG) . . . . .	83
8.4	Parallelisation . . . . .	84
<b>9</b>	<b>Methods for simulating X-ray fluorescence and HOPG reflection</b>	<b>85</b>
9.1	Implementation of the X-ray source . . . . .	85
9.2	Implementation of the detector . . . . .	85
9.3	Data processing and analysis . . . . .	86
9.3.1	HOPG crystal reflection curve – XOP v2.4 . . . . .	86
9.3.2	Detector resolution . . . . .	88
<b>10</b>	<b>Results: Comparison of simulated and experimental results</b>	<b>89</b>
10.1	Simulations of various iodine concentrations . . . . .	89
10.1.1	PMMA/mouse phantom (phantom 2) . . . . .	90
10.1.2	Eppendorf phantom (phantom 1) . . . . .	92
10.1.3	Contributions of multiple scattered photons . . . . .	95
10.2	Simulation of the background distribution . . . . .	96
<b>11</b>	<b>Influence of detector characteristics and mosaicity</b>	<b>97</b>
11.1	Detector size and bin size . . . . .	99
11.2	Influence of intrinsic detector resolution . . . . .	104
11.3	Influence of crystal mosaicity . . . . .	105
<b>IV</b>	<b>Summary and conclusion</b>	<b>109</b>
<b>V</b>	<b>APPENDIX</b>	<b>117</b>
<b>A.</b>	<b>Excerpt of Stripping algorithm</b>	<b>119</b>
<b>B.</b>	<b>SNRs for 1.0 mg/ml iodine concentration</b>	<b>124</b>

<b>List of figures</b>	<b>127</b>
<b>List of tables</b>	<b>131</b>
<b>List of abbreviations and acronyms</b>	<b>133</b>
<b>List of symbols</b>	<b>135</b>
<b>Bibliography</b>	<b>136</b>

# Introduction

Biomedical imaging includes methodologies for preclinical research, i.e. *in vitro* and *in vivo* laboratory animal testing of drugs, procedures or medical treatment in animals [1], as well as for medical imaging for diagnostics and treatment monitoring [2]. Nowadays, it is getting more and more important to observe molecular processes within living subjects (*in vivo*) with the highest possible spatial resolution and with decisive molecular or functional information [3]. The main clinical molecular imaging technologies are positron emission tomography (PET) and single-photon emission computed tomography (SPECT). Both nuclear imaging modalities employ synthetic radiolabeled molecules (*radiopharmaceuticals*) to assess specific molecular processes such as an abnormally increased glucose uptake, which is often a biomarker of cancer. Radiopharmaceuticals emit gamma-ray signals which allow for relatively deep penetration depths of about 30 cm and afford a high sensitivity due to the low gamma signature of the surrounding tissue. A large diversity and ongoing development of radiopharmaceuticals gives nuclear imaging a high specificity. The central drawback of PET and SPECT is the low spatial resolution compared to other molecular imaging modalities ( $\sim 4 - 8$  mm for PET and  $\sim 10$  mm for SPECT [4]). Other disadvantages include the high expenses of the facilities and the production of radiopharmaceuticals. Also, the low temporal resolution (tens of seconds to minutes for PET and even less for SPECT) limits the number of measurements per individual and leads to long measurement times. Other less prominent molecular imaging tools based on optical imaging such as bioluminescence [5] or optical fluorescence [6] achieve very high spatial resolutions, which are however limited to near surface structures. The reason for this is that an increasing penetration depth induces an increased amount of optical scatter, leaving optical imaging technologies for whole-body human examinations unfeasible. Magnetic resonance imaging (MRI) is also gaining new applications towards functional imaging with spatial resolutions of mm and sub-mm size in humans and mice respectively. The drawback of the application of MRI to functional and molecular imaging is its intrinsic low sensitivity, which could only be compensated by very long scan times.

X-rays and computed tomography (CT) meet the demands of high spatial resolution (sub-mm in humans and 0.1 mm in mice), but are limited to morphological information based on absorption contrast. Nevertheless, CT is an indispensable imaging tool in current clinical practice, delivering fundamental information for diagnostics, disease assessment and treatment planning. The ongoing development in new source and detection schemes potentially improves the spatial resolution in X-ray CT down to about  $10 \mu\text{m}$  [7], which further improves the precision of diagnostics and treatment planning. Further advances in image contrast and quality are realised by applying con-

trast agents based on elements with a high atomic number ( $Z$ ), such as iodine, gold, or gadolinium: The general correlation between an increasing X-ray energy and penetration depth followed by a continuous decrease in X-ray absorption, is interrupted by the so-called *K-edge*. The K-edge is a phenomenon based on atomic processes and is characterised by a sudden discrete and discontinuous increase in X-ray attenuation. Tuning the X-ray source to the K-edge of the applied high- $Z$  contrast agent can considerably raise the X-ray absorption efficiency and yield improved images in terms of contrast and quality. Heavy atomic elements exhibit a K-edge in the diagnostic X-ray energy range of a few 10 keV, which makes it exploitable for imaging biological probes [8,9]. In brief, absorption-based CT imaging achieves the best spatial resolution among all imaging modalities, but falls short in providing functional/molecular features. Aiming to supply absorption-based X-ray imaging with functional/molecular imaging capability, nanoparticles (NPs) have been used as alternatives to conventional contrast media [10]. In particular gold nanoparticles (AuNPs) have potential as a functional/molecular contrast agent due to their biocompatibility [11–13]. Also they have successfully been conjugated to certain bio-molecules yielding reconstruction images of specific tumors [14–16].

Molecular imaging based on X-ray fluorescence (XRF) could provide sensitive and quantitative detection of NPs and other high-contrast media and is thus a suitable non-invasive candidate to meet the above-mentioned demands on spatial resolution and sensitivity. XRF imaging is based on the *Photoelectric effect* and works as follows: An object containing a high atomic number contrast agent distribution is irradiated by a primary X-ray source, which induces an excitation of the high- $Z$  tracer atoms followed by an emission of secondary X-rays. These secondary X-rays are referred to as *X-ray fluorescence*. An energy resolving detector traditionally placed at a  $90^\circ$  angle to the X-ray source records the isotropically emitted XRF signal. Positioning the detector in the beamline would lead to count-rate and dead-time problems of the detector and would obscure the desired fluorescence signal. The recorded XRF spectrum exhibits the energies of XRF photons and those of background scatter photons (mainly Compton scattering), which however can be spectrally discriminated such that the resulting net signal reveals quantitative information about the tracer concentration of the object of investigation.

Combining CT imaging with the XRF method, also referred to as *X-ray computed tomography* (XFCT) [17–19], enables functionalised CT imaging with a spatial resolution in the sub-mm (or less) range since the spatial resolution is solely determined by the diameter of the applied X-ray pencil beam. A few of the first studies translating XRF applications to human scale objects of interest were carried out in synchrotron facilities in order to determine the amount of different tracer agents in breast tissue [20–22]. Using monochromatic X-radiation considerably reduces the amount of single- and multiple scattered Compton photons in the resulting XRF spectrum, thus improving the XRF signal yield. Current research, however, is generally limited to conventional X-ray sources such as conventional CT devices or industrial X-ray tubes.

The generation of tomographic images based on XRF and NPs together with conventional X-ray tubes has experimentally and theoretically been scrutinised in phantoms [23–31], and even in mice [32,33]. A phantom is a specially designed object

used for performance tests of various imaging devices. The goal of all of these studies is to push the limits in terms of sensitivity, spatial resolution, X-ray dose and scan times. Spatial resolutions of typically a few mm, could be reduced to 200  $\mu\text{m}$  [33], and detectable NPs concentrations of about 0.25-4% could be reduced to 0.1% [26].

However, a major drawback remains the long scan times (hours per slice) and high radiation dose (more than several hundred mGy), which are far from being practical for clinical use. These constraints are a consequence of the low usable X-ray flux of conventional X-ray tubes and the large amount of Compton background photons, impairing their sensitivity [29]. An approach for distinguishing XRF photons from the vast number of background photons could be the implementation of an advanced spatial and spectral filtering scheme [31].

The choice of the detection device itself is crucial for XRF imaging. Semiconductor detector systems including compound materials such as HPGe and CdTe exhibit the highest energy resolution among all XRF detectors ( $< 1$  keV [FWHM] as opposed to several keV in e.g. scintillators), and thus are the preferred choice for the energy-selective detection of XRF imaging. The major drawback, however, is the limited size of the sensitive area of typically  $\approx 1$  cm<sup>2</sup>, which causes an immense loss of fluorescence information considering the isotropic emission of XRF photons. A reduced angular coverage correlates with decreased counting statistics and thus demands increased exposure times and larger amounts of contrast agents in order to compensate the loss of information. The application of arrays including multiple detectors with adequate detector resolution [25, 34], as well as the implementation of an advanced spatial filtering scheme [31] could be a solution to the problem, but would be associated with high costs.

An approach of relaxing the demands on the detection system would be filtering of the XRF signal before hitting the detector's sensitive area. Suitable optical devices are energy-selective analyser crystals that isolate the energy region of the XRF signal while suppressing other energy regions and thus enable the application of large area detectors with moderate energy resolution. One of the first studies implementing an energy-selective crystal for XRF measurements was proposed for synchrotron X-ray sources exploiting the Bragg reflection of a single bent Laue crystal [35]. Single crystals, however, exhibit narrow reflection curves and therefore only allow limited tolerance for angular deviations of incoming XRF photons. A more promising solution for energy selection of isotropically emitted XRF photons is the implementation of mosaic crystals such as synthetically generated, highly oriented/annealed pyrolytic graphite crystals (HOPG/HAPG) [36, 37]. Preliminary XRF studies with polychromatic X-radiation and an HOPG crystal [38, 39] suggest that a suitable energy selection of XRF photons prior to hitting the sensitive area of the detector minimises the importance of the detector's energy resolution.

This thesis aims to tackle the general problem of high X-ray doses and contrast agent concentrations in XRF imaging by pursuing the implementation of energy-selective mosaic HOPG/HAPG crystals. Experimental investigations as well as extensive Monte Carlo simulations will deal with the detection of iodine fluorescence photons ( $K_{\alpha}$ ) emitted by a phantom with the size of a mouse and induced by polychromatic X-rays of an industrial X-ray tube. As a practical outcome, the integration of HOPG/HAPG crys-

tals show that constraints on energy resolution of the detection system can be relaxed, while maintaining acceptable imaging parameters such as scanning time, radiation dose, and sensitivity. The implementation of large area detectors with moderate energy resolution thus seems conceivable for XRF imaging. The main steps taken to fulfil the aim of this thesis are outlined in the following section.

# Structure and outline of this thesis

This section summarises the parts of the thesis and main steps taken to fulfil the objective of this thesis, namely to pave the way to large area detector implementation in the context of diagnostic XRF imaging.

- Part I **Fundamentals of X-ray spectroscopy** provides the theoretical background for this thesis and summarises the fundamental principals and applications of X-ray spectroscopy including the generation of X-rays for diagnostic imaging (chapter 1), the interaction of X-rays with matter (chapter 2), and the detection of X-rays with common X-ray detectors for XRF imaging (chapter 3). Chapter 4 summarises the basic aspects of X-ray diffraction optics and introduces the HOPG/HAPG mosaic crystal. Chapter 5 concludes with the methods of data processing and analysis used in this thesis.
- Part II **Experimental investigation** deals with the experimental realisation of the proposed imaging setup with energy-selective mosaic HOPG/HAPG crystals. Chapter 6 provides detailed information on the materials and methods that were used including the industrial X-ray source, phantoms, the HOPG/HAPG crystal and the used semiconductor detector. Moreover, a measurement and estimation scheme for the applied X-ray dose (*air kerma*) is introduced. This chapter concludes with an essential spectrum correction method (*stripping algorithm*) which is indispensable for a genuine XRF data analysis and comparison to simulated results. The results of the XRF and dose measurements are summarised in chapter 7. The findings form the basis for building the powerful Monte Carlo code for XRF simulations presented in part III of the thesis.
- Part III **Monte Carlo Simulation GEANT4** deals with the computational realisation of the proposed XRF imaging setup and investigates the feasibility of an extended XRF imaging setup. Chapter 8 introduces the underlying Monte Carlo code GEANT4 which was used to build the extensive XRF code used for all simulations in this thesis. All relevant aspects for realising XRF simulations and in particular the computational realisation of HOPG/HAPG properties and detector characteristics are explained in chapter 9. Chapter 10 compares the simulated data to the experimental results of chapter 7 (part II) and demonstrates the practicability of the developed Monte Carlo XRF code. An analysis of the potential implementation of large area detectors, scrutinising resolution limiting aspects such as bin size, intrinsic detector resolution, and crystal mosaicity are discussed in chapter 11.

- Part IV **Summary and conclusion** summarises the results of this thesis and discusses the consequences and outlook in the context of current research.
- Part V **Appendix** supplies additional material not included in the main text of the thesis, such as code sequences and tables. This part is followed by the lists of figures and tables, the lists of abbreviations, acronyms and symbols and the bibliography. It concludes with the acknowledgments and the declaration of honor.



# Part I

## Fundamentals of diagnostic X-ray spectroscopy



Part I provides the theoretical background to all important aspects relevant for XRF imaging and is primarily organised according to the book by Beckhoff et al. [40]. Chapter 1 deals with sources of artificial generation of X-radiation, particularly those commonly used for the generation of XRF in research. Since this work is based on experiments using a polychromatic X-ray source, there will be a particular focus on industrial X-ray tubes. Chapter 2 recapitulates the interaction of X-rays with matter and chapter 3 summarises the characteristics of detection devices commonly used in XRF imaging. The properties of semiconductor detectors are treated in detail, since they have been shown to be the most promising choice in XRF signal detection. Chapter 4 summarises all relevant aspects regarding X-ray optics and HOPG/HAPG crystals. Finally, chapter 5 gives a brief overview of the applied methods for data processing and analysis.



# 1. Generation of X-rays for diagnostic imaging

X-rays are electromagnetic waves that first have been described in 1895 by the German physicist and first nobel prize winner for physics Conrad Wilhelm Röntgen [41]. He used the name *X-Strahlung* (German for *X-radiation*) in order to specify an unknown type of radiation. With wavelengths ranging from about 10 nm ( $\approx 124$  eV) to less than 10 pm ( $\approx 124$  keV) [40], X-rays are situated in the electromagnetic spectrum between extreme ultraviolet (EUV) light (soft X-rays) and  $\gamma$ -radiation (hard X-rays), even overlapping to some extent with the wavelength range of the latter (figure 1.1). Each photon carries an energy proportional to its frequency  $\nu$  and inversely proportional to its wavelength  $\lambda$ :

$$E = h \cdot \nu = \frac{h \cdot c}{\lambda}, \quad (1.1)$$

where  $h$  is Planck's constant,  $c$  is the speed of light and  $\lambda$  is the wavelength of the photon<sup>1</sup>. Therefore X- and  $\gamma$ -radiation are distinguished by their origin: X-rays are a consequence of high-energy electron processes, whereas  $\gamma$ -rays are generated via processes within the atomic nucleus.

This chapter gives a short overview of the principles of artificial X-ray sources, namely X-ray tubes, radionuclide sources and synchrotron radiation. All sources are described in terms of their feasibility for X-ray diagnostics. There is a focus on the generation of X-rays via X-ray tubes, since this work deals with XRF imaging induced by industrial X-ray tube facilities.

## 1.1 X-ray tubes

### Physical Principle

In X-ray tubes, electrons are emitted from a cathode and accelerated towards an anode in an electric field provided by a positive potential  $U_A$  ( $\hat{=}$  *acceleration voltage* or *high voltage*) of the anode relative to the cathode. These electrons strike the anode and interact with the target material in various processes, which leads to a deceleration and hence energy loss of the incident electrons. The majority of incident electrons scatters on the shell electrons of the target material, transferring only a small part of their energy that is then dissipated as heat. Only a small fraction of electrons undergo inelastic scattering, which is followed by a continuous deceleration in the Coulomb field

---

<sup>1</sup>Planck's constant:  $h = 6.626 \cdot 10^{-34}$  Js; Speed of light in vacuum:  $c = 2.998 \cdot 10^8$  m/s

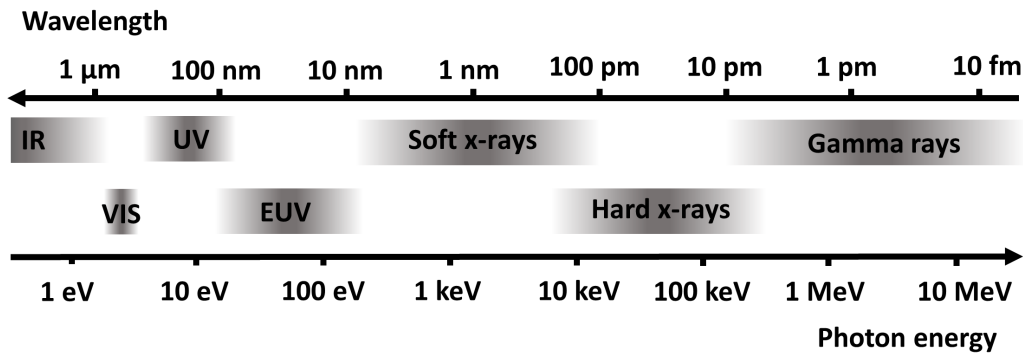


**Figure 1.1:** Classification of X-rays within the electromagnetic spectrum in logarithmic scale (IR, infrared; VIS, visible light; UV, ultraviolet; EUV, extreme ultraviolet).

generated by the nuclei of the target material. This slowing down process generates *bremstrahlung* (from German, literally meaning *braking radiation*). Bremsstrahlung is typically emitted as a *continuous spectrum*, since free electrons are not bound and therefore do not occupy orbits with specific quantised energy levels. The maximum photon energy is determined by the acceleration voltage  $U_A$  given by the X-ray tube and is reached when the incident electron transfers its whole kinetic energy  $E_{kin}$  to the photon:

$$E_{max} = E_{kin} = e \cdot U_A, \quad (1.2)$$

where  $e$  is the elementary or electron charge<sup>2</sup>. Using the Duane-Hunt law [42] and equation 1.1 an upper limit for the photon frequency  $\nu_{max}$  and consequently a lower limit for the photon wave length  $\lambda_{min}$  can be calculated:

$$\nu_{max} = \frac{E_{max}}{h} = \frac{e \cdot U_A}{h}, \quad (1.3)$$

$$\lambda_{min} = \frac{c \cdot h}{E_{max}} = \frac{c \cdot h}{e \cdot U_A}. \quad (1.4)$$

X-rays are also generated by electron transitions between inner electron shells within the atom, resulting in so-called *characteristic X-radiation*, which is a discrete line emission that can unambiguously be attributed to the target element.

Every X-ray spectrum generated by an X-ray tube is a superposition of a continuous part and characteristic lines (figure 1.2). The maximum energy, shape and intensity of the continuous spectrum are determined by the value of the high voltage  $U_A$ , whereas the position of the characteristic lines depends on the anode material. For each line, there exists an excitation threshold, that is equal to the corresponding absorption edge of the anode material. Therefore the characteristic line is not present in the emission spectrum, if the value of  $U_A$  remains below this threshold.

<sup>2</sup>Electron charge:  $e = 1.602 \cdot 10^{-19}$  C

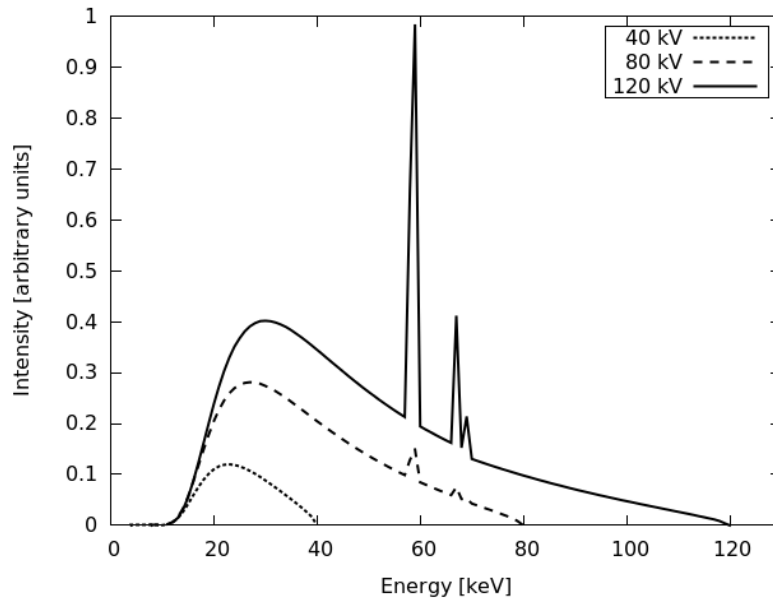


**Figure 1.2:** Spectra using various acceleration voltages  $U_A$  produced by an X-ray tube with tungsten anode and a filter of 1 mm aluminium (Al). The energy spectra are a superposition of continuous and characteristic X-rays. The characteristic emission lines, as a consequence of electron transitions from the atomic L-shell to K-shell ( $K_\alpha \approx 58.0$  keV) and from M-shell to K-shell ( $K_\beta \approx 67.2$  keV), are clearly visible. If the applied high voltage lies below the absorption edge of tungsten ( $E_{\text{edge}}(W) \approx 69.5$  keV), no characteristic lines are present in the emission spectra (cp.  $U_A = 40$  kV). All spectra were calculated using SpekCalc [74] (cp. section 6.2.2).

## Efficiency

The total emitted X-ray power  $P$  [kW] can be estimated with the empirical relation [43, 44]

$$P = c \cdot Z \cdot I \cdot U_A^2, \quad (1.5)$$

where  $Z$  is the atomic number of the anode material,  $I$  the anode electric current [A],  $U_A$  the acceleration voltage [kV], and  $c$  a constant of order  $10^{-6}$  [kV $^{-1}$ ]. From this relation the efficiency coefficient for X-ray production is derived as:

$$\eta \equiv \frac{P}{U_A \cdot I} \approx 10^{-6} Z \cdot U_A [\text{kV}]. \quad (1.6)$$

According to this expression the amount of X-rays produced by X-ray tubes is very low. For a tungsten anode ( $Z = 74$ ) and an applied high voltage of  $U_A = 160$  kV, the efficiency of X-ray generation amounts to approximately 1%, meaning that about 99% of the kinetic energy from the incident electrons is released as waste heat. This exposes the anode to very high thermal energy dissipation, making anode cooling a serious issue.

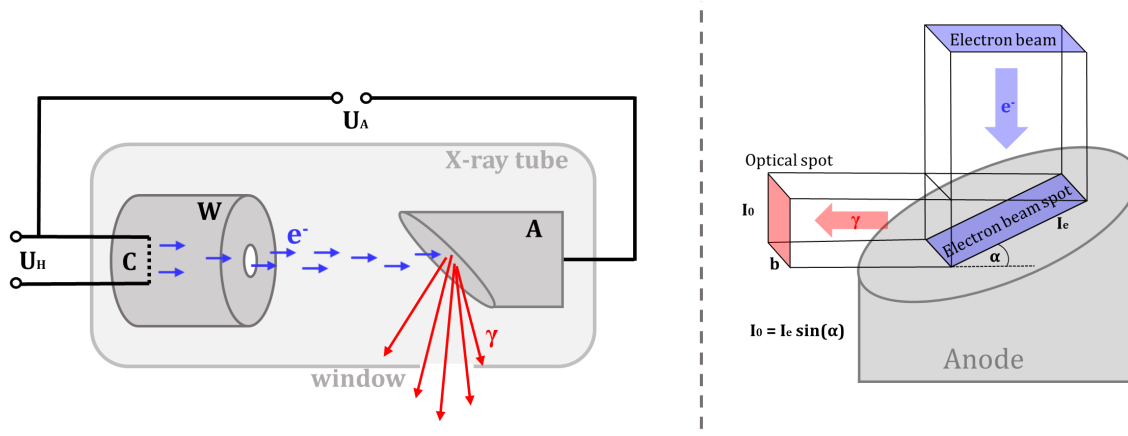


**Figure 1.3:** Left: Basic design of an X-ray tube. An applied high voltage  $U_A$  accelerates electrons  $e^-$  from the cathode towards the anode, where they interact with the target material and generate X-ray photons  $\gamma$ . ( $U_H$ , heating voltage for dissolving electrons from the cathode; C, cathode; W, Wehnelt electrode;  $U_A$ , accelerating/high voltage; A, anode).

Right: Schematic representation of the relation between electron beam spot and optical focal spot for a specific anode angle  $\alpha$ .

## General Design

The basic design of an X-ray tube is shown in figure 1.3 (left), where a directly heated electron emitter (cathode) is arranged in a so-called Wehnelt electrode, which enables focusing of electrons towards the anode [45]. The cathode is usually made of tungsten, and common anode materials are chromium, copper, molybdenum and tungsten. Imbedding the disk-shaped anode into a copper block enables dissipated heat to be conducted away from the target. Also, implementing rotating anodes promotes heat conduction, where a disk-shaped anode rotates under a spatially fixed electron beam so that the heat load is distributed over a larger circular area [40]. Both cathode and anode are mounted in a high vacuum chamber in order to preserve high voltage isolation. Although X-rays are emitted isotropically, they can only leave the X-ray tube through a certain exit window, which also functions as an inherent filter to minimise the amount of low energy X-rays. This reduces the amount of unnecessary exposure of the irradiated object, in that low energy X-rays are likely to be absorbed by the target and do not contribute to the resulting image anyway. The size of the optical focal spot is determined via the angle between the anode surface and the normal to the exit window (figure 1.3, right). This angle generates a difference in size between the electron beam and optical spot and thus deals with the immense heat dissipation from the anode when generating small optical spot sizes. Some X-ray tubes allow for switching between small and large focal spots, so that for the latter higher electron currents can be used, since the number of incident electrons can be distributed over a larger area on the anode without running into cooling problems. However, small focal spot sizes are preferred in applications together with X-ray optics such as capillary optics, Fresnel and Fresnel-Bragg optics as well as for HOPG crystals (cp. chapter 4), since their efficiency depends crucially on the *brilliance* of the X-ray source. Brilliance is a measure of the X-ray beam quality, which is dependent on the angular divergence, cross-sectional area and monochromaticity.



## 1.2 Radioisotopic sources

Radioisotopic sources are devices in the shape of disks or rings where radioactive material is sealed in capsules made of material that is tuned to the type of emitted radiation, the chemical properties of the radionuclide and the condition of application (cp. figure 1.4, left). In particular annular shaped devices provide sufficiently large photon fluxes necessary for XRF applications. The advantage of using radioisotopic sources is that they are small in size, reasonably priced and independent of external power supply. A major disadvantage, however, arises from the potential radiation hazard due to their continuous radiation emission.

Radioactive material decays via various processes of which only  $\alpha$ -decay,  $\beta^\pm$ -decay and K-capture are relevant for XRF. For a detailed description of the various decay processes the reader is referred to [46] or [47]. Nuclear decay can be followed by an emission of  $\gamma$ -radiation or X-radiation (also referred to as  $\gamma$ -decay), or internal conversion. For direct excitation in XRF applications mainly  $\gamma$ -radiating isotopes are used, which operates by K-electron capture followed by the emission of K- and L-shell X-ray photons. This is particularly beneficial since the resulting spectrum is dominated by spectral lines (cp. figure 1.4, right) as opposed to the spectrum produced by X-ray tubes where the total spectrum is a composite of spectral lines and a continuous part (figure 1.2). The excitation of material using only (quasi-)monochromatic radiation significantly reduces the amount of noise in the resulting XRF spectrum.

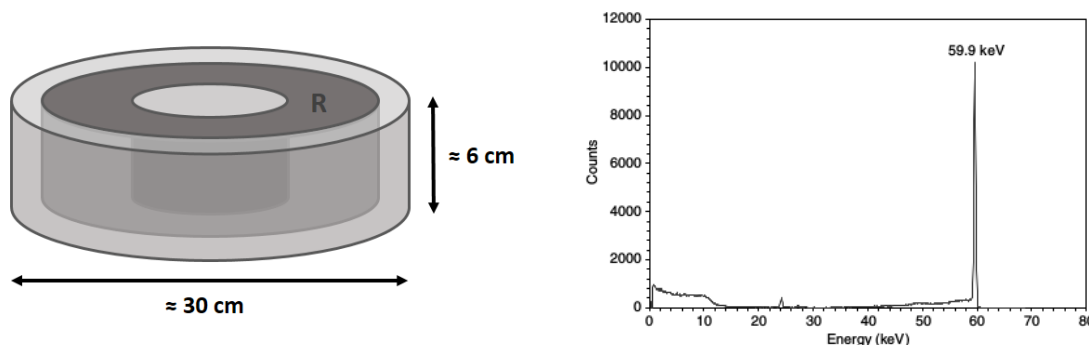


**Figure 1.4:** *Left: Example of the shape and dimensions of a typical radioisotopic source. R: Radioisotopic material within and annular container. Right: X-Ray Spectrum of the radioisotope  $^{241}\text{Am}$  (Americium). The linear spectrum is beneficial for XRF applications since due to the lack of a continuous part, background noise is significantly suppressed. The graphic is taken from [40].*

## 1.3 Synchrotron radiation sources

In synchrotron radiation facilities X-rays are generated via the centripetal acceleration of charged particles moving in strong magnetic fields. Particularly known is the synchrotron radiation emitted by accelerated electrons and positrons in storage rings or similar circular high energy particle accelerators (figure 1.5, top). The high-speed electrons are forced on a closed path by strong magnetic fields where they lose

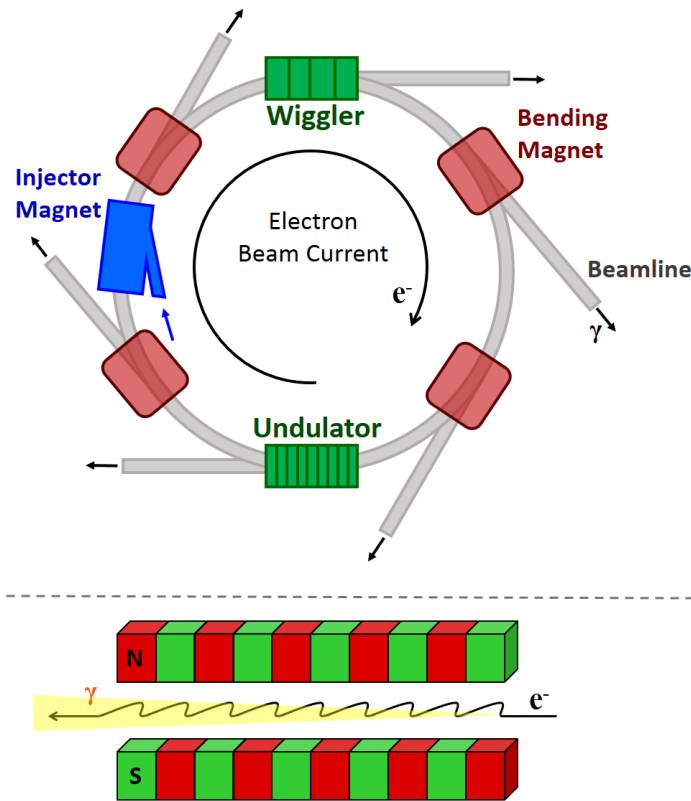


**Figure 1.5:** *Top: Design of a typical third-generation synchrotron with the following components: Bending magnets keep the electrons on the track, but lead to an energy loss in the form of electromagnetic radiation; Undulators and wigglers are components introduced with the third-generation of synchrotrons and function as accelerating devices; The beamline constitutes the exit of the highly brilliant radiation beam.*

*Bottom: Schematic structure of a wiggler or undulator: Electrons traversing the periodic structure of dipole magnets undergo oscillations and radiate intense and concentrated energy.*

energy as electromagnetic radiation. First-generation synchrotron facilities used bending electromagnets; however in order to achieve higher radiation intensities, insertion devices, so-called *wigglers* and *undulators*, are employed in modern third-generation synchrotrons. These insertion devices are situated at the entrance of straight sections tangentially arranged at openings in the storage ring, to let the electromagnetic radiation exit into *beamlines*. Many tens or hundreds of alternating S and N pole magnets (*wiggles*) force the electrons onto a sinusoidal or helical path, thus multiplying the total intensity of the beam. A *wiggler* can be approximated to be a series of aligned bending magnets, delivering a broad energy bandwidth where the intensity is proportional to the number of magnetic poles (figure 1.5, bottom). In contrast, the undulator intensity scales with the square of the number of poles and the bandwidth is relatively narrow, which makes the use of undulators very attractive for applications using high energy monochromatic polarised light. The advantage of the implementation of synchrotron radiation sources in medical context is the high brilliance of the beam, which is many orders of magnitude higher than that of conventional X-ray tubes. In fact, the first published XRF experiments in terms of medical diagnostics

were performed in synchrotron facilities [17, 20]. Another advantageous aspect is that the applied monochromators are able to tune the resulting X-ray energy to a wide range of monochromatic energies extending from the sub-eV range up to the MeV range. Nevertheless, the utilisation is impractical in daily research routine and especially in medical routine applications, since synchrotron radiation facilities demand large amounts of space, are limited in access, and are associated with high costs.

## 2. Interaction of X-rays with matter

Photons, as well as charged or uncharged particles, traversing a thin slice of matter  $dx$  [cm] have a certain probability  $dW$  to interact with the atomic nuclei or electrons of that target material. This probability is related to the amount of scattering sources  $n$  within an arbitrary volume  $V$  and the cross section  $\sigma_{tot}$  [cm<sup>2</sup>]:

$$dW = \frac{n}{V} \cdot \sigma_{tot} dx = N \cdot \sigma_{tot} dx, \quad (2.1)$$

where  $N$  is the amount of scattering centres per unit volume in matter. This equation holds for any kind of particle and electromagnetic radiation, but for reasons of simplicity this chapter will focus on the latter, in particular on the interaction of X-radiation with matter. A target particle can interact with other particles in various ways. Depending on the energy and angle of incidence, an X-ray photon can be scattered elastically or inelastically off the atom shell or nucleus, be deflected without energy transfer or could leave the atom in an excited state. There are four different types of interaction, namely Rayleigh scattering, Compton scattering, the Photoelectric effect and pair production. However, for X-ray photons with energies ranging between a few hundred eV and a few hundred keV, only the first three types of interaction can occur. Therefore in this work, pair production is not considered. The contributions of each kind of interaction type are described by their corresponding *partial cross section*  $\sigma_i$ , which is a measure of probability that this particular process will occur. The partial cross section depends on the atomic number  $Z$  of the target material and the photon energy  $E_\gamma$ . All partial cross sections of the above-mentioned interaction types ( $\sigma_R$  for Rayleigh scattering,  $\sigma_C$  for Compton scattering and  $\sigma_P$  for the Photoelectric effect) sum up to the total cross section  $\sigma_{tot}$ :

$$\sigma_{tot} = \sigma_R + \sigma_C + \sigma_P. \quad (2.2)$$

Together with the number of atoms per volume element  $n$ , this total cross section multiplies to the linear attenuation coefficient  $\mu = n \cdot \sigma_{tot}$  with dimension [length]<sup>-1</sup>, which is a crucial quantity for the attenuation of electromagnetic radiation passing through material. As the X-ray beam traverses a slice of matter  $dx$  the change in beam intensity  $\mathcal{I}$  satisfies the following condition:

$$d\mathcal{I} = -\mu \mathcal{I} dx. \quad (2.3)$$

Dividing both sides of this equation by  $\mathcal{I}$  and subsequently integrating yields:

$$\mathcal{I} = \mathcal{I}(x) = c e^{-\mu x}, \quad (2.4)$$

where  $c$  is a constant defining the initial condition. Setting the initial condition as  $c = \mathcal{I}(x = 0) = \mathcal{I}_0$  yields the expression for the intensity of the unscattered photon beam and its mean free path:

$$\mathcal{I}(x) = \mathcal{I}_0 e^{-\mu x}. \quad (2.5)$$

This relation is known as Beer-Lambert law or exponential attenuation law [50, 51]. Substituting the *mass attenuation coefficient*  $\mu/\rho$ , where  $\rho$  is the density of the penetrated material, for the linear attenuation coefficient  $\mu$  allows us to express this in terms of the attenuator density:

$$\mathcal{I}(x) = \mathcal{I}_0 e^{(-x\rho \frac{\mu}{\rho})}. \quad (2.6)$$

The mass attenuation coefficient is proportional to the cross section and with equation 2.1 it follows:

$$\frac{\mu}{\rho} = \frac{1}{\rho} \frac{n}{V} \sigma_{tot} = \frac{1}{\rho} \frac{\rho V}{V \frac{m_a}{N_A}} \sigma_{tot} = \frac{N_A}{m_a} \sigma_{tot}, \quad (2.7)$$

where  $m_a$  denotes the atomic mass number of the material and  $N_A$  the Avogadro constant<sup>3</sup>. Figure 2.1 shows the mass attenuation coefficients for photons in water. In the energy range considered for diagnostic XRF imaging ( $\approx 1$  keV - 100 keV) the dominant interaction types are coherent (Rayleigh) scattering, incoherent (Compton) scattering and photoelectric absorption. With increasing energy, the probability for Compton scattering increases becoming the predominant interaction modality in water.

## 2.1 Rayleigh scattering

Rayleigh (coherent) scattering describes the primarily elastic scattering of electromagnetic radiation off target particles, whose diameter is significantly smaller than the wavelength  $\lambda$  of the incident photons. The interaction occurs on bound electrons in the atomic shell without energy transfer or absorption, leaving the atom neither excited nor ionised. Consequently, this process is more probable for low photon energies and high  $Z$  target materials. This type of interaction mainly scatters photons in forward directions:

$$\sigma_R \propto \frac{Z^2}{E_\gamma^2}. \quad (2.8)$$

---

<sup>3</sup>Avogadro constant:  $N_A \approx 6.022 \cdot 10^{23} \text{ mol}^{-1}$

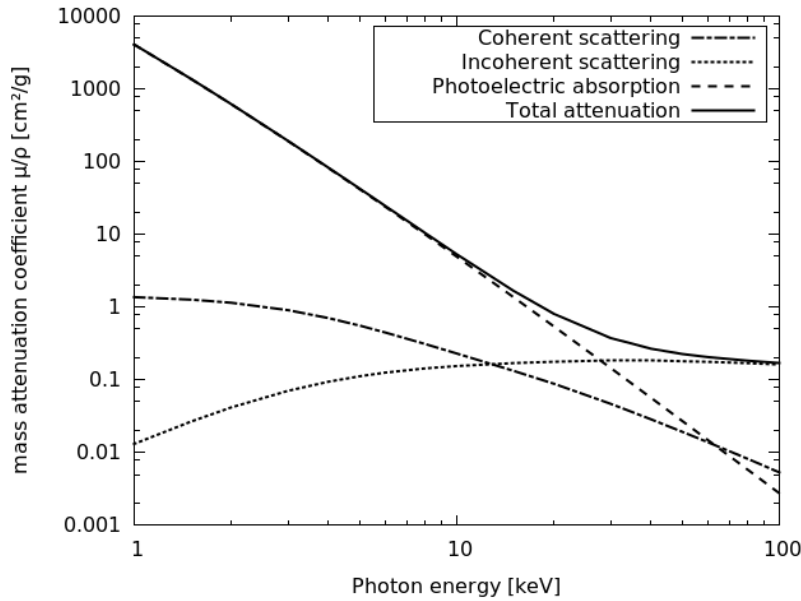


**Figure 2.1:** Photon mass attenuation coefficients for water in the energy range between 1 keV and 100 keV. The data is taken from the NIST webpage [www.nist.gov](http://www.nist.gov).

## 2.2 Compton scattering

Compton (incoherent) scattering is the inelastic interaction of a photon with a weakly bound (quasi-free) electron of the atomic shell. As a result of the interaction the incident photon is deflected from its original direction and transfers part of its energy and momentum to the recoiling electron. If the photon energy is considerably larger than the binding energy of the recoil electron, the electron is ejected from the atom while the atom is left ionised. The energy of the resulting photon  $E'_\gamma$  can be derived via the laws of energy and momentum conservation. Assuming the electron becomes unbound and approximating its energy with its rest mass energy of  $E_e = E_0 = m_0c^2 = 511 \text{ keV}^1$ , the energy of the emitted photon is:

$$E'_\gamma = \frac{E_\gamma}{1 + \frac{E_\gamma}{m_0c^2}(1 - \cos(\psi))}, \quad (2.9)$$

where  $E_\gamma$  is the energy of the primary photon and  $\psi$  denotes the angle of the scattered photon.

A model for the angular distribution of scattered photons is given by the Klein-Nishina formula [53] for the differential cross section of Compton scattering:

$$\frac{d\sigma_C}{d\Omega} = \frac{\alpha^2}{2} \left( \frac{E'_\gamma}{E_\gamma} \right)^2 \left( \frac{E'_\gamma}{E_\gamma} + \frac{E_\gamma}{E'_\gamma} - \sin^2(\psi) \right), \quad (2.10)$$

where  $\Omega$  is the solid angle and  $\alpha$  is the fine-structure constant<sup>2</sup>. Figure 2.2 shows

<sup>1</sup> $m_0$ : Electron rest mass

<sup>2</sup> $\alpha \approx 1/137$  [dimensionless]

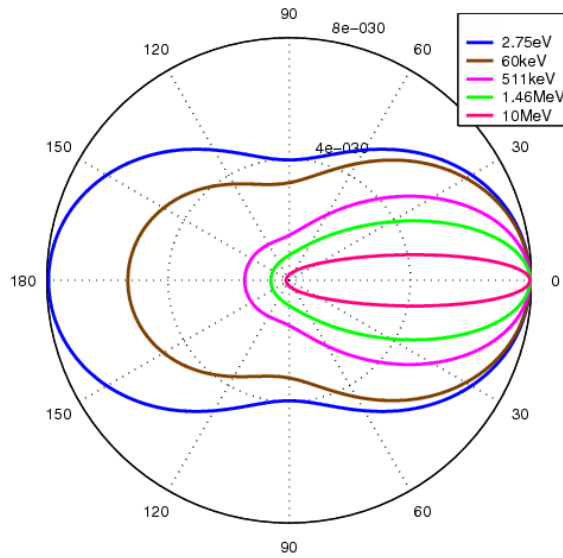


**Figure 2.2:** Klein-Nishina cross section  $\sigma_C$  for photon scattering angles at different incident photon energies  $E_\gamma$ . For incident energies significantly below the electron rest mass energy, the resulting scatter profile is nearly isotropic. Increasing initial energies lead to a shift towards larger amounts of forward scattering. This image is taken from [wikimedia.org](https://commons.wikimedia.org/wiki/File:Klein-Nishina_Cross_Section.png) (retrieved 1 May 2019).

the dependency of the photon scattering angle on the incident photon energy. For incident photon energies much below the electron rest mass energy the scatter profile is nearly isotropic and backscattering is as probable as forward scattering. Larger photon energies generally result in forward scattering. The corresponding Compton cross section is proportional to the quotient of the atomic number of the target material and the incident photon energy:

$$\sigma_C \propto \frac{Z}{E_\gamma}. \quad (2.11)$$

## 2.3 Photoelectric effect

The photoelectric effect is schematically explained in figure 2.3: An incident photon with energy  $E_\gamma$  is entirely absorbed by an atom of the target material. The photon energy is transferred to an orbital electron, which consequently either moves to a higher energy level or is ejected from the atom. The latter case can only occur if the photon energy is larger than the binding energy of the electron shell. In this case, the ejected electron is called a *photoelectron* and escapes the atom with a kinetic energy of

$$E_{kin} = E_\gamma - E_I, \quad (2.12)$$

where  $E_I$  ( $I = K, L, M, \text{etc.}$ ) is the ionisation energy, or binding energy of the corresponding electron shell. As a consequence the atom is ionised. The vacancy left

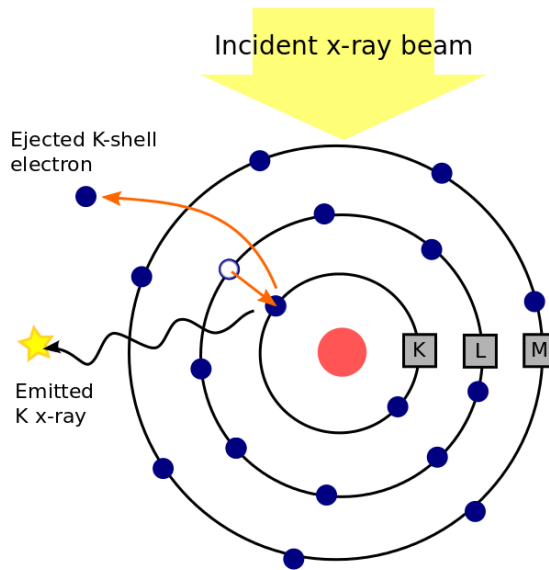


**Figure 2.3:** The process of X-ray fluorescence in atomic structure. The ejected photoelectron leaves a vacancy within the atomic shell which is filled by a higher energy electron accompanied by an energy loss, which is released via a secondary (or fluorescence) photon.

by the photoelectron is filled by an electron of a higher energy level, which releases the difference in energy by ejecting a so-called secondary X-ray photon. This photon is also referred to as *characteristic X-ray photon*, since its energy is unique to the specific material. The whole process is called *X-ray fluorescence* (XRF). The ejected fluorescence photons are emitted isotropically and are classified depending on the electron shell, where the vacancy is present and on the origin of the filling electron. Table 2.1 summarises the nomenclature used in this thesis.

electron shell transition	L → K	M → K	N → K	M → L	N → L
secondary photon label	$K_{\alpha}$	$K_{\beta}$	$K_{\gamma}$	$L_{\alpha}$	$L_{\beta}$

**Table 2.1:** Secondary photon labels for the electron transitions between atomic shells.

A competing process besides the ejection of photoelectrons, is the dissipation of excess energy in so-called *Auger electrons* [48, 49]: Instead of releasing the energy in form of a secondary or fluorescence photon, the released energy can be transferred to a further shell-electron, which again induces the process of electron ejection. This electron, however, is called an Auger electron instead of photoelectron, since it follows an interaction with a secondary photon. Nevertheless, the interaction also initiates a rearrangement of electrons triggering an emission of further secondary photons.

The probability of the Photoelectric effect is given by the cross section

$$\sigma_P \propto \frac{Z^n}{E_{\gamma}^{3.5}}, \quad (2.13)$$

where the factor  $n$  varies between 4 and 5 for the energy range of interest. For materials with large atomic numbers the interaction probability is increased due to the higher



electron binding energy. In particular, for K-shell electrons of very dense absorbers and high  $Z$  this probability is increased.

For increasing photon energies the probability of photoabsorption decreases, until the photon energy equals the binding energy  $E_L$  of the L-shell of the target material. At this point the probability for photoelectric interaction is at a maximum (cp. figure 2.4 with an example of iodine). In the energy range between the binding energy of the L-shell and the adjacent K-shell the photoabsorption probability again decreases, until it reaches another maximum at the position of the binding energy of the K-shell ( $E_K$ ). These *jumps* within the energy spectrum are referred to as *absorption edge* or K-edge, L-edge etc., with respect to the corresponding electron shell.

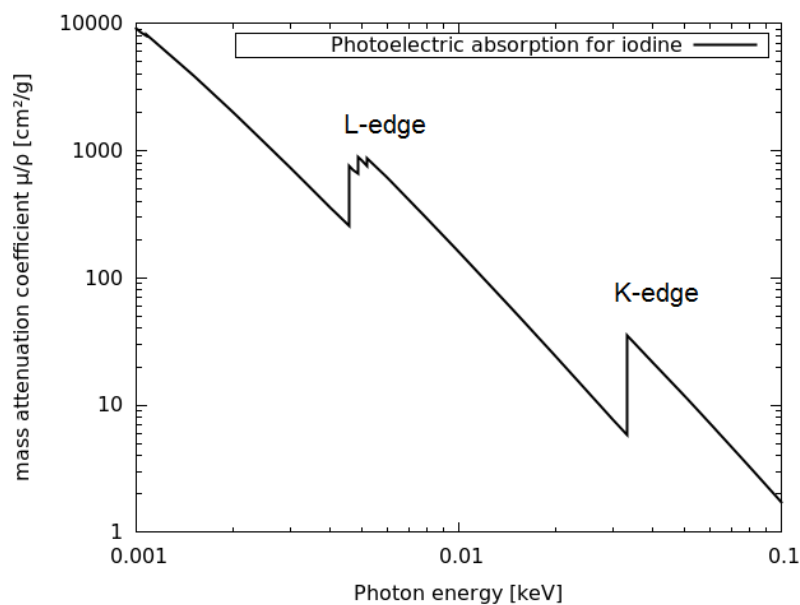


**Figure 2.4:** Energy dependence of the mass attenuation coefficient  $\mu/\rho$  for iodine. The probability for the Photoelectric effect decreases with increasing photon energies. Photon energies with presumably instantaneous increases of  $\mu/\rho$  characterise the absorption edges related to the binding energies of the corresponding atomic shells. The data is taken from the NIST webpage [www.nist.gov](http://www.nist.gov).

## 3. Detection of X-rays and detector characteristics

X-ray detectors convert the energy transported by the radiation into forms that can be recognised either visually or electronically. Common X-ray detectors used so far in medical imaging are for instance photographic films, imaging plates and flat panel detectors. In terms of X-ray detection they are *analog* and provide no information about the individual photon energy in that they convert X-ray photons, for instance, into blackened grains (films) or metastable states (image plate). This chapter focuses on digital energy resolved X-ray detectors preferably used for the detection of XRF photons and presents their general features.

### 3.1 Basic properties of X-ray detectors for XRF imaging

Digital X-ray detectors convert the energy of X-ray photons deposited on the detector material into an electric signal. This signal is processed and generates a readout, which, depending on the detector, provides information about measures such as photon energy and arrival time of the event. Depending on the detector type, the incident photon energy is processed either by direct or indirect measurement. Semiconductor or gas-filled detectors directly translate the energy into a certain amount of charge, which is then collected at an output electrode (anode). In contrast, scintillation detectors first convert the radiation energy into optical photons, which are then translated into electrons by means of a photodetector and multiplied by a *photomultiplier* tube or *photodiode*.

For common digital X-ray detectors the charge  $Q$  collected at the anode is the basis for further signal processing:

$$Q = \frac{E_\gamma}{\epsilon_c}, \quad (3.1)$$

where  $E_\gamma$  is the energy of the photon hitting the detector sensitive area, and  $\epsilon_c$  is an electronic charge conversion factor. This factor is the average energy necessary to produce an electron–ion pair in the detector material. It differs considerably with the detector type due to the different underlying physical processes during the conversion mechanism from photon energy to charge production. There exists no detector, which is perfectly suited for all possible detection applications. For choosing the appropriate detector type it is necessary to understand several characteristics specifying the

attributes of a detector. This section is dedicated to the various characteristics of detection systems predominantly used in X-ray applications.

### 3.1.1 Detector sensitivity and detector response function

An important aspect to consider when choosing a suitable detection device is whether the detector is sensitive to the type of radiation and energy range studied. The detector's sensitivity is a measure of how efficiently radiation is converted into a useable signal, i.e. counts. It describes the change of the detector's response due to a change of X-ray intensity. Sensitivity depends on several factors, such as the interaction cross section with the detector material, detector mass, detector noise and the shielding material in which the detector is embedded. For an energy resolved detector the pulse height distribution that describes the efficiency of charge-conversion, depending on the incident photon energy, is called *response function*.

### 3.1.2 Detection efficiency

Detector efficiency relates to the probability of the conversion of the incident photon energy into a useable signal and indicates the number of photons that are required to produce a signal (or *response*). The total detection efficiency  $\eta_{tot}(E)$  is defined as the fraction of photons that deposit their full energy in the detector material  $N_{deposit}(E)$  with respect to the total amount of photons emitted by the X-ray source  $N_{emit}(E)$ :

$$\eta_{tot}(E) = \frac{N_{deposit}(E)}{N_{emit}(E)}. \quad (3.2)$$

This dimension is constrained by various properties of the detection scheme, namely geometrical efficiency  $\eta_g$ , intrinsic efficiency  $\eta_i(E)$  and photopeak efficiency  $\eta_p(E)$ . If the mean free path for an interaction with the detector material is significantly smaller than the detector length, then the total detection efficiency can be written as the product

$$\eta_{tot}(E) = \eta_g \times \eta_i(E) \times \eta_p(E). \quad (3.3)$$

#### Geometrical efficiency $\eta_g$

Conventional X-ray sources are often approximated as point sources, emitting X-rays isotropically such that only a limited fraction of X-rays can be detected. Even an extensive detector array forming a spherical shape around the source would leave voids in the detector's solid angle coverage, thus yielding a difference between the number of photons that have left the X-ray source and the number of photons that have actually reached the detector's sensitive area. This discrepancy is expressed in the geometrical efficiency  $\eta_g$ . For a point source this factor relates to the solid angle  $\Omega$  as follows:

$$\eta_g = \frac{\Omega}{4\pi}, \quad (3.4)$$

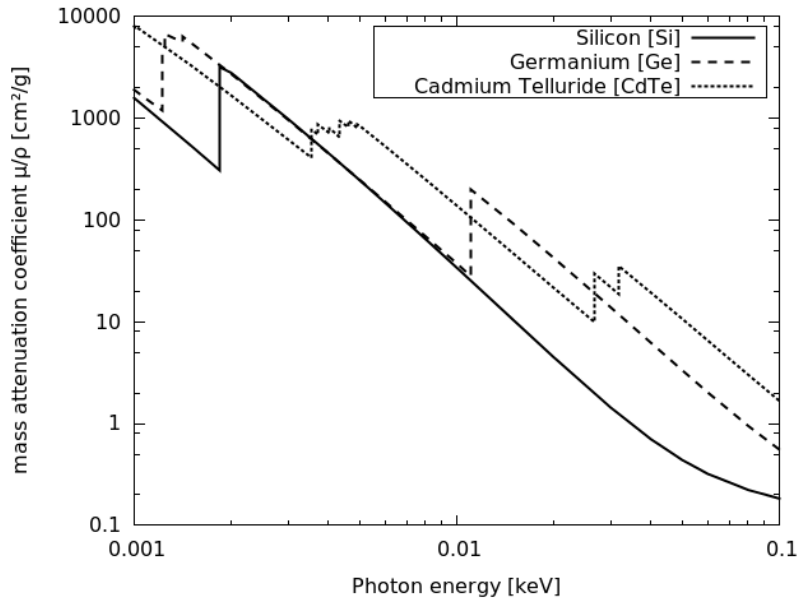


**Figure 3.1:** Mass attenuation coefficient  $\mu/\rho$  for the typical semiconductor detector materials Si, Ge and CdTe. The data is taken from the NIST webpage [www.nist.gov](http://www.nist.gov).

with  $\Omega = \frac{A}{r^2}$ , where  $A$  depicts the detector area and  $r$  is the distance between the X-ray source and the detector.

### Intrinsic efficiency $\eta_i(E)$

The fraction of the number of photons entering the detector that actually interact with the detector material is expressed by the intrinsic efficiency  $\eta_i(E)$ . It depends on the absorption properties of the detector material and on the detector thickness, and can be derived from the Beer-Lambert law (equation 2.6, chapter 2). The intrinsic efficiency denotes the interaction probability of the material and is calculated according to

$$\eta_i(E) = 1 - e^{(-x\rho \frac{\mu}{\rho})}, \quad (3.5)$$

where  $\mu/\rho$  is the mass attenuation coefficient at a given photon energy (cp. equation 2.7, chapter 2),  $x$  the thickness of the detector material and  $\rho$  its density. Figure 3.1 shows the mass attenuation coefficient for the materials Silicon (Si), Germanium (Ge) and Cadmium Telluride (CdTe) within an energy range between 1 and 100 keV. Materials with higher atomic numbers (Ge, CdTe) have higher absorption capabilities compared to lower  $Z$  materials such as Si. Also the detector thickness influences the intrinsic efficiency in that for thin detectors the amount of transmitting photons is increased.

### Photopeak efficiency $\eta_p(E)$

The photopeak efficiency  $\eta_p(E)$  defines the fraction of photons that deposit their full energy in the detector material. This quantity is limited by Compton interaction and

escape peaks. For incident photons with an energy of up to 100 keV the probability of Compton absorption is rather low and re-absorption of Compton scattered photons is rather high. This is visible in the recorded spectrum as a so-called *Compton continuum* within an energy range between 0 keV and  $\frac{2E_\gamma^2 m_0 c^2}{1+2E_\gamma m_0 c^2}$  keV, where the latter expression denotes the maximum energy released to the scattered electron.  $E_\gamma$  is the primary photon energy and  $m_0 c^2$  defines the rest-mass energy of the electron. Another limiting factor of the photopeak efficiency arises from escape events: An incident photon interacting according to the Photoelectric effect generates a secondary (fluorescence) photon as a consequence of a rearrangement of electrons within the atomic shell. This secondary photon has a high probability of being re-absorbed within the detector material. However, if the primary photon interacts close to the detector surface, as is the case for low energy photons, there is a non-negligible probability that the produced secondary photon escapes the detector volume instead of being re-absorbed. As a result, the energy spectrum displays escape peaks with energy  $E_{peak}$ , which is the difference between the primary photon energy  $E_\gamma$  and the escaped fluorescence photon  $E_{efp}$ :

$$E_{peak} = E_\gamma - E_{efp}. \quad (3.6)$$

In the low energy range approximately between 0.1 and 1 keV, the detection efficiency is limited by absorption in the dead layer of the detector material itself or by absorption in the window material of the detector.

### 3.1.3 Energy resolution

The energy resolution  $\Delta E$  describes the ability to distinguish between incoming photons that are closely separated in energy. Each photon hitting the detector surface deposits an energy  $E_\gamma$  that is translated into an electric signal with a certain pulse height distribution according to an ideal Dirac  $\delta$ -function. The broadening is a result of various statistical fluctuations during the measurement. Energy resolution is typically expressed in terms of the FWHM of the recorded photopeak,  $\Delta E_{FWHM}$ . The larger the FWHM the worse the energy resolution. Sometimes the energy resolution is the ratio (expressed as a percentage) between FWHM and centroid value of the distribution, i.e. the expected photon energy  $E_\gamma$ :

$$\text{Energy Resolution [\%]} = \frac{\Delta E_{FWHM}}{E_\gamma} \cdot 100. \quad (3.7)$$

Very often, the energy resolution is approximated by a Gaussian distribution:

$$G(E_\gamma | \bar{E}, \sigma) = \frac{N_0}{\sigma \sqrt{2\pi}} \cdot \exp\left\{ -\frac{(E_\gamma - \bar{E})^2}{2\sigma^2} \right\}, \quad (3.8)$$

where  $N_0$  is the peak area,  $\bar{E}$  is the mean value around the photopeak  $E_\gamma$ , and  $\sigma$  is the standard deviation, which for Gaussian distributions always relates to the FWHM of the recorded photopeak as  $\Delta E_{FWHM} = 2\sqrt{2\ln(2)}\sigma \approx 2.35\sigma$ . The operating mode

of the used detector type introduces various sources of statistical fluctuations that influence the total energy resolution:

$$\Delta E^2 = \Delta E_{stat}^2 + \Delta E_{noise}^2 + \Delta E_{multi}^2 + \Delta E_{trapping}^2. \quad (3.9)$$

These factors will be explained in greater detail in the following sections, since energy resolution has a crucial effect on the results obtained in this work.

### Statistical fluctuation $\Delta E_{stat}^2$

The first term in equation 3.9 introduces broadening due to statistical fluctuations that arise from the conversion of photon energy into charge carriers. Since this is an intrinsic feature of the operation of the detector, this contribution cannot be ameliorated via refinement of the detection system. The variance  $\sigma_n^2$  is proportional to the average number of charge carriers  $n$  generated during the detection process approximately following Poisson statistics:

$$\sigma_n = \sqrt{n}. \quad (3.10)$$

This number is very large for scintillation detectors so that Poisson statistics applies very well. The average amount of generated carriers is proportional to the primary photon energy  $E_\gamma$  and related to that number via the charge conversion factor  $\epsilon_c$ , yielding:

$$\sigma_n = \sqrt{\frac{E_\gamma}{\epsilon_c}}. \quad (3.11)$$

Consequently, the contribution to the energy resolution due to statistical fluctuations approximately amounts to

$$\Delta E_{stat} = 2.35 \sigma = 2.35 \epsilon_c \sigma_n = 2.35 \sqrt{(E_\gamma \epsilon_c)}. \quad (3.12)$$

In semiconductor detectors and gas proportional counters the correlation in the processes that generate individual charge carriers leads to a smaller variance of generated charge than predicted by Poisson statistics. This deviation is taken into account by an additional quantity, the Fano factor  $F$  [50], which is defined as the ratio of the variance to the mean of a random process. As a result, for Poisson statistics this factor equals one, whereas for dispersions of a probability distribution with decreased variance, the Fano factor lies below one ( $F < 1$ ). Taking into account the deviation from Poisson statistics with  $\sigma_n = \sqrt{Fn}$  yields:

$$\Delta E_{stat} = 2.35 \sqrt{(FE_\gamma \epsilon_c)}. \quad (3.13)$$

A smaller variance implies less noise and consequently leads to a smaller contribution of  $\Delta E_{stat}$ , thus improving the energy resolution.

**Electronic noise  $\Delta E_{noise}^2$** 

The second term contributing to the energy resolution in equation 3.9 is characterised by electronic noise that stems from the detector-amplifier system and is in most of the cases described by the equivalent noise charge (ENC). The ENC is the amount of charge delivered by the detector that produces a pulse signal for which the ratio between pulse amplitude and background noise equals one. If the ENC is known, the broadening in energy resolution conveyed by electronic noise is

$$\Delta E_{noise} = 2.35 \epsilon_c \frac{\text{ENC}}{e}. \quad (3.14)$$

For detectors that operate on the basis of photomultipliers, where the number of charge carriers (electrons) is amplified via a multiplication factor  $M$ , the influence of electronic noise is reduced by that factor, since the fraction of primary carriers generated in the detector (before multiplication) is the same:

$$\Delta E_{noise} = 2.35 \epsilon_c \frac{\text{ENC}}{e M}. \quad (3.15)$$

**Multiplication  $\Delta E_{multi}^2$** 

Even though detectors with internal multiplication gain  $M$  exhibit smaller broadening due to electronic noise, this multiplication factor introduces an additional broadening term  $\Delta E_{multi}$ . This term results from the statistics of the multiplication process involved.

**Charge trapping  $\Delta E_{trapping}^2$** 

The fourth factor of equation 3.9 is related to the charge collection efficiency, relevant for semiconductor detectors. These detectors have a high amount of defects in the crystal lattice, leading to an increased number of trapping sites resulting in charge trapping [54] and inferior charge carrier transport. In spectroscopy this effect is also called *hole tailing*, since the high amount of trapping sites leads to a small lifetime of holes. This is relevant when the attenuation length is long with respect to the detector thickness. If an interaction occurs near the cathode, the signal arises mainly from the electron current with almost no charge loss. If an interaction occurs close to the anode, the holes must travel the whole detector thickness. With a short lifetime this leads to a significant charge loss, qualitatively visible in the energy spectrum as a *tail* on the lower energy side of a photopeak.

**3.1.4 Dead time**

A detector requires a finite processing time for energy deposition and the readout of information. During this processing time, the detector along with its electronics are not able to respond to subsequent signals. If the detector is insensitive to further signals during this readout time, the information of subsequent events is lost. For that

reason, the processing time is referred to as *dead time* [51]. Modern detectors usually operate with an intrinsic *real time*  $T_R$  and *life time*  $T_L$  clock, which are related via

$$T_L = T_R - T_D, \quad (3.16)$$

where  $T_D$  is the dead time. The real time is the natural proceeding time and the life time is the time in which the detector is able to respond to incoming events. Dead time is usually reported as a percentage in order to provide a relative measure of dead time losses  $DT$ :

$$DT [\%] = \frac{T_D}{T_R} \times 100 [\%] = \left(1 - \frac{T_L}{T_R}\right) \times 100 [\%]. \quad (3.17)$$

Most manufacturers assure reliable dead time correction feasibilities to the measured spectrum if the dead time does not exceed approximately 60 %. Nevertheless, it is recommended to keep the dead time at a minimum level since especially for measurements using non-linear radiating X-ray sources, dead time corrections become increasingly difficult.

It should be noted that detection devices can be characterised by a paralyzable or a non-paralyzable behaviour [52]. In a paralyzable detector, a detection event which occurs during the dead time will be lost and restart the dead time, so that with increasing event rates the detector will not be able to process any further signals at all. In a non-paralyzable detector an event happening during the dead time will be lost, but not restart the dead time: With an increasing event rate the non-paralyzable detector will reach a saturation rate which equals the inverse of the dead time.

## 3.2 Common X-ray detectors

### 3.2.1 Gas detectors

Gas detectors or *Gas proportional counters* are characterised through a moderate energy resolution and a large sensitive area compared to other detectors. With relatively high counting rate capabilities dead time problems are considerably reduced. They are typically composed of a cylindrical gas-filled container with an electric field applied across it (figure 3.2). The outer surface functions as a cathode, whereas the anode is a wire across the cylinder axis. X-ray photons hitting the detector sensitive area mainly interact via the Photoelectric effect and produce electrons that are accelerated towards the anode due to a suitable voltage difference applied between the electrodes. Subsequent collisions between these electrons and the gas atoms lead to an ionisation of the gas. The number of electrons generated by means of ionisation together with a multiplication factor  $M$  for these electrons produce a signal with an amplitude that is proportional to the energy of the primary photons and the voltage difference. The most commonly used gases are argon (Ar), xenon (Xe), neon (Ne) and krypton (Kr). The charge conversion factor  $\epsilon_c$  typically ranges from 25 to 35 eV/ion pair and the multiplication factor  $M$  lies approximately between 10 and  $10^4$ , leading to an intermediate



energy resolution compared to other typical X-ray detector types. As a consequence of the low gas density and the limited thickness, gas proportional counters suffer from a reduced detection efficiency compared to other detectors.

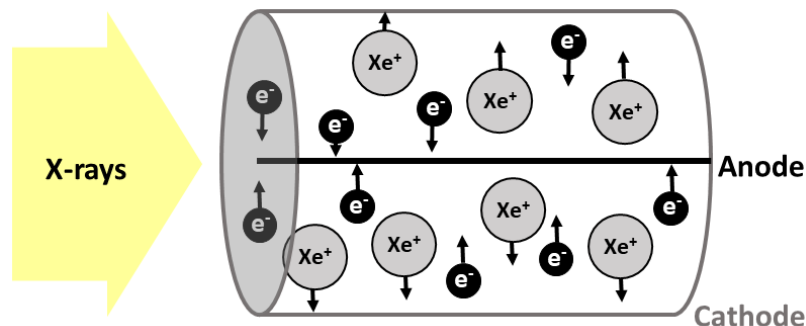


**Figure 3.2:** Basic functionality of a gas detector: X-rays hitting the surface produce electrons that are accelerated towards the anode within an electric field. Gas atoms (here xenon) move towards the cathode and collide with the electrons, producing further electrons that all together sum up to a signal that is proportional to the incident primary photon energy.

### 3.2.2 Scintillation detectors

Scintillation detectors basically consist of a scintillation crystal, e.g. NaI(Tl) or CsI(Tl), a photodetector (*photocathode*), and a photomultiplier tube (figure 3.3). The crystal translates the deposited energy of the incident X-ray photons into optical photons. Via the photoelectric effect these optical photons interact with the photodetector, which results in the ejection of electrons. These electrons are transferred to a photomultiplier tube, which multiplies the electrons by further electrodes (so-called *dynodes*). The collection of all electrons produces a transient current to the electronics and a suitable detection device relates the signal to the incident primary photo energy. As opposed to gas proportional counters, their higher atomic number and usually extensive thickness enables the detection of X-rays in a broader energy range. Moreover, scintillation crystals can be fabricated in large volumes so that X-rays are transported over large distances, yielding the best sensitivity among X-ray detectors. However, due to the nonlinearity of the scintillator's response and the fact that only a few primary photons are detected, their energy resolution is the poorest of all X-ray detectors, notably in the low energy range. Using a photomultiplier tube as a photodetector ensures a high photon count performance, but degrades the detection sensitivity. Photodiodes are a suitable alternative, but are prone to an increased electronic noise, which further degrades the energy resolution.

### 3.2.3 Semiconductor detectors

Semiconductor detectors measure the amount of charge carriers, or *electron-hole pairs*, produced as a result of the interaction of ionising radiation with the detector material. Deeper understanding is provided by basic solid-state physics: Atomic electron energy

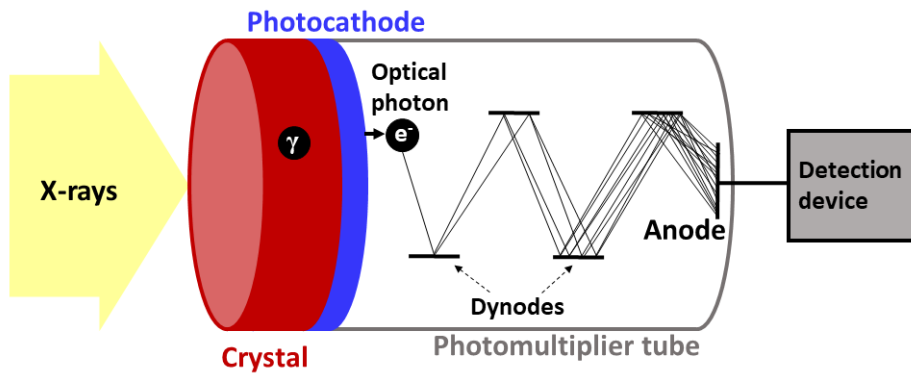


**Figure 3.3:** Basic functionality of a scintillation detector: The crystal translates the incident X-ray energy into optical photons, which provoke the ejection of electrons by interacting with the photodetector (or photocathode). The electrons are then multiplied by a photomultiplier tube. The sum of all electrons produces a transient current to the electronics.

states of single crystal semiconductor material are organised in *bands* of energy states. While most outer electrons lie in the so-called *valence band*, the next higher states are in the *conduction band*. These bands are energetically separated by an energy gap called the *bandgap*. If the semiconductor material does not inhibit impurities (as is the case for *dopants*), this gap contains forbidden states. An electron can advance from the valence to the conduction band if it receives an energy at least equal to the bandgap. Under the influence of an externally applied electric field, the promoted electron can move and be collected at the electrode (anode). In the same way, the vacancy or *hole* in the valence band left by the advanced electron, can move towards the opposite electrode (cathode) if an electric field is applied (figure 3.4). Electrons move faster than holes within the same crystal material. Incident X-ray photons interacting with the semiconductor material produce primary electrons as a consequence of the ionisation process. These primary electrons in turn excite bound electrons to the conduction band. The promoted electrons again can generate even further electrons in a cascading process, such that in the end a large number of electron-hole pairs is produced and collected at the electrodes of the detection device. If dopants are added to the semiconductor material, as is the case for semiconductors containing impurities, the conduction properties can be altered. Dopants introducing additional free electrons are called *donors* and dopants increasing the amount of holes are referred to as *acceptors*. Semiconductors doped with the former are so-called n-type materials, whereas the latter are classified as p-type material. Both increase the conductivity of the detector.

For each material, the amount of energy required to create an electron-hole pair is known. The number of electron-hole pairs is proportional to the intensity of the incident X-radiation. For semiconductor detectors the energy conversion coefficient  $\epsilon_c$ , i.e. the required average energy for the production of a charge-carrier pair, is only a few electronvolts compared to gas proportional or scintillation detectors, resulting in an increased transconductance. This notably reduces the electronic noise which is the reason why semiconductor detectors exhibit smaller statistical broadening (high energy resolution) and a high detection efficiency. The low energy conversion coefficient,

and hence increased stopping power towards incoming photons, is a consequence of the comparably high- $Z$  material of semiconductor detectors. Expanding the material dimensions raises the amount of spectral distortions due to hole tailing caused by an increase of density defects in the crystal lattice. As a result, semiconductors are significantly limited in size and therefore are sensitive to detecting incoming radiation through a relatively small solid angle. Nevertheless, semiconductor detectors are the preferred choice in terms of detection efficiency and energy resolution in X-ray spectroscopy. In particular compound semiconductors such as CdTe, CZT or HgI<sub>2</sub> (among others), exhibit even higher attenuation coefficients and wider bandgaps, which leads to a high energy resolution: A large band gap reduces the amount of electrons crossing the band gap and reach the conduction band, where they would respond to the electric field and produce electronic noise.

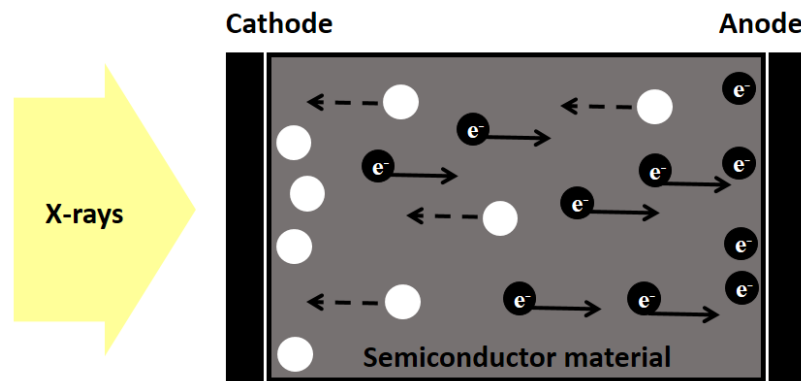


**Figure 3.4:** *Basic functionality of a semiconductor detector: Under the influence of an applied voltage, incident electrons are accelerated towards the anode, whereas the remaining holes move towards the cathode. Due to cascading processes triggered by the accelerated electrons, further electron-hole pairs are produced and collected at the electrodes of the detector.*

## 4. X-ray diffraction optics and mosaic crystals

In XRF spectrometry monochromators can be used to monochromatise either the primary X-ray beam generated by the source, or the secondary beam originating from the object of interest (cp. figure 4.1). In the former case, the optic device suppresses the spectral parts of the continuous background and bremsstrahlung contributions from the X-ray source and thus forms a primary beam with spectral properties that are optimal for the task. In the latter case the monochromator functions as an energy-selective analyser that exposes the fluorescence signal and eliminates the multiple scattered (Compton-)background nearly completely.

The feasibility of X-ray spectroscopic techniques is generally limited by the energy resolution and the collection efficiency of the X-ray optics. Other experiments are limited by the X-ray flux, either by an isotropically radiating X-ray source, or by an isotropically radiated signal emitted by the object of interest itself. In the case of XRF experiments with polychromatic X-ray sources, the X-ray flux is reduced due to both reasons. Therefore, the solid angle of the optics collecting X-rays needs to be as large as possible. Commonly used single crystals exhibit only a small integrated reflectivity, which is due to a small angle of acceptance. The collection angle can be increased by bending or by implementing a large area crystal. Large single crystals, however, are in general not available and bending is (normally) impractical. A solution for increasing the collection angle is the use of a multiple analyser crystal detection system as in [35].

An alternative approach is the implementation of mosaic crystals, which exhibit a large solid angle coverage due to their composition of small crystallites randomly oriented over a small angular range parallel to the surface plane. The FWHM of the angular

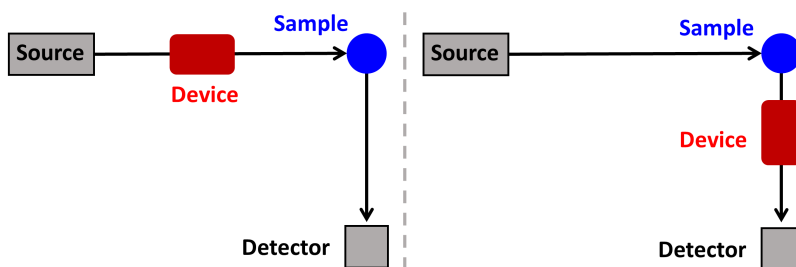


**Figure 4.1:** Monochromatising optic devices can be used as monochromators for primary X-ray beams (left), or as energy-selective analysers (right), that suppress spurious multiple scattered background photons and accentuate the fluorescence signal.

distribution of these crystallites is referred to as *mosaic spread* or *mosaicity*. For single crystals the term *rocking curve width*, is more prominent and one of the major quantities to investigate imperfections of crystal planes. The integrated reflectivity of mosaic crystals can be many orders of magnitude larger than that of single crystals, since the mosaic spread of the former is much larger than the rocking curve width of the latter [55, 56]. If the intrinsic reflection broadening of the individual crystallites (*Darwin width* [37] in the case of single crystals) is small, high energy resolutions can be realised [56, 57]. Mosaic crystals can easily be bent to any shape since its crystallite structure releases stress on the material, as opposed to ideal crystals. Highly oriented pyrolytic graphite (HOPG) is a synthetically produced and well studied mosaic crystal [36, 55, 58]. Further development lead to the production of HOPG with low intrinsic reflection broadening enabling a high spectral resolution. In some literature this type of thin pyrolytic graphite is called HAPG, for *highly annealed pyrolytic graphite* [56, 57, 59].

This chapter will summarise the underlying process of Bragg diffraction and provides an introduction to the properties of HOPG/HAPG crystals.

## 4.1 Bragg diffraction of mosaic crystals

The theory of the so-called *Bragg condition* was developed by William Lawrence Bragg and his father William Henry Bragg in order to describe constructive and deconstructive interference of waves on three-dimensional crystals [60]. With this formalism it was possible for the first time to analyse the structure of matter on the atomic level. The Bragg condition formulated for the reciprocal lattice is expressed via the famous Laue equations [61], which describe the process of diffraction of incoming waves on crystal lattices.

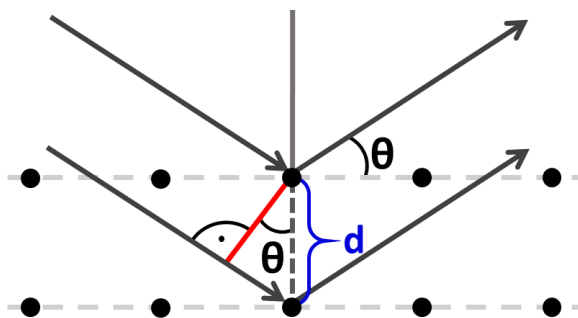


**Figure 4.2:** Process of the Bragg diffraction: A set of parallel lattice planes is separated by a characteristic distance  $d$ . If X-ray photons are incident under a certain angle  $\Theta$  (Bragg angle) their reflections on the atomic lattice add up leading to constructive interference.

Most X-rays incident on a crystal are transmitted without interacting with the crystal material. A small part, however, interacts via X-ray diffraction which is a consequence of X-ray photons scattering on the atomic lattice of the crystal. This can also be defined as weak reflection of X-rays on the lattice planes, albeit the radiation is only reflected in directions where the individual reflections are constructively superimposed. This condition is specified in the Bragg equation:

$$n\lambda = 2d \sin(\Theta), \quad (4.1)$$

where  $d$  is the distance between two parallel lattice planes,  $\lambda$  the wave length of the incident radiation,  $\Theta$  the so-called *Bragg-angle* which is the angle between the X-ray beam and the lattice plane, and  $n$  a natural number depicting the order of diffraction. Figure 4.2 delineates the process of Bragg diffraction on atomic level. Each set of parallel lattice planes is separated by a characteristic distance  $d$ , thus exhibiting a characteristic Bragg angle. The lattice planes are usually defined via the *Laue indices*  $hkl$ , such that for cubic crystal systems the distance  $d$  between lattice planes yields:

$$d_{hkl} = \frac{a}{h^2 + k^2 + l^2}, \quad (4.2)$$

where  $a$  is a constant. Inserting this relation into the Bragg equation 4.1 leads to the Bragg condition for cubic crystal systems:

$$\sin(\Theta)^2 = \frac{\lambda^2}{4a^2}(h^2 + k^2 + l^2). \quad (4.3)$$

## 4.2 Physical and geometrical properties of HOPG/HAPG

The mosaic spread determines the integrated reflectivity (energetic bandwidth that can be reflected) and the peak reflectivity depending on the crystal thickness. The random orientation of crystallites assures that every photon of the incident photon distribution hits the crystallite plane at the right Bragg angle (cp. figure 4.3). In a symmetric geometry, i.e. in the case that the distances source-to-crystal and crystal-to-detector are equal, the mosaic crystal focuses monochromatic light in the diffraction plane and thus augments the intensity in the detection plane and the spectral resolution. This effect is called *parafocusing effect* [62]. For each crystal plane an upper limit for the energy resolution (bandwidth of the reflection curve) is determined by the intrinsic width of Bragg reflection (or Darwin width) of the individual crystallites. It is a result of the contributions of various factors such as particle size, strain broadening, crystal thickness and mosaicity [63]. The following dispersion relation defines the upper limit of energy resolution [56]:

$$\frac{E}{\Delta E} = \frac{\tan(\Theta)}{\Delta\Theta}. \quad (4.4)$$

Here  $\Delta E$  is the energy resolution and  $\Delta\Theta$  the intrinsic width of Bragg reflection. This resolution, however, can hardly be achieved in practice due to further focusing errors caused by the source size and aberrations of the detection geometry. The crystal thickness also influences the energy resolution, which can be estimated via

$$\Delta s = 2D\cos(\Theta), \quad (4.5)$$

where  $\Delta s$  is the spatial smearing in the detector plane and  $D$  is the crystal thickness (cp. figure 4.3). The broadening of the integrated reflectivity by the crystallites participating in the reflection event originate from the following extinction processes: The incident beam can be attenuated by diffraction inside each individual crystallite (primary extinction) or by screening of the lower lying crystallites by crystallites lying near the crystal surface (secondary extinction). A larger mosaic spread reduces the effect of screening and thus enables a larger penetration depth. However, reflections from deeper lying crystal planes give rise to an asymmetric reflection profile. Implementing crystals that are thinner than the penetration depth, or crystals with a small mosaic spread (such as HAPG) therefore improve the energy resolution, although with the cost of reduced reflected beam intensity.

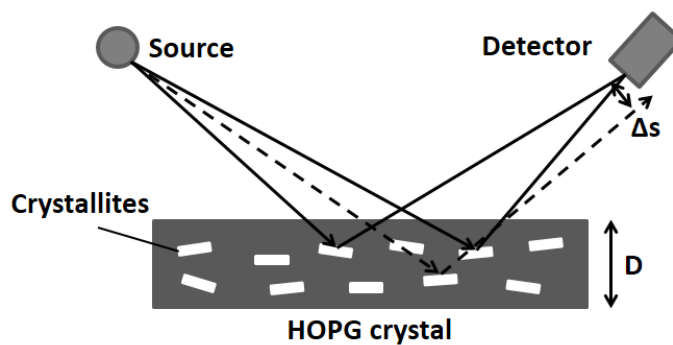


**Figure 4.3:** *Mosaic focusing: An incident beam can be reflected even if the angle deviates from the angle determined by the Bragg condition. Due to the mosaicity the beam penetrates the crystal and encounters a crystallite with the necessary orientation in order to be Bragg reflected.*

## 5. Data processing and analysis

The X-ray spectra obtained by measurement or simulation, consist of XRF and background counts, meaning that the net XRF signal is the difference between the total amount of counts  $N_{tot}$  and the background counts  $N_{bg}$ . One of the challenges of separating the XRF signal from the scatter background is introduced by the binning of the detector, which is a clustering of counts of various energies in defined energy intervals (*bin sizes*). Small bin sizes are associated with a high energy resolution, but lead to an increased amount of noise if the source flux is too low in order to compensate for this deficiency.

This chapter provides a brief overview of the methods for data analysis used in this study. Procedures on how to obtain these spectra via experimental detection or simulation will be explained in the respective parts within this thesis.

### 5.1 Fitting of XRF signal and background

In order to evaluate the XRF signal for every individual XRF spectrum, the XRF signal is fitted with a simple Gaussian distribution:

$$G(x|E_{K_\alpha}, \sigma) = A_{\text{XRF}} \cdot \exp\left\{-\frac{(x - E_{K_\alpha})^2}{2\sigma^2}\right\}, \quad (5.1)$$

where  $A_{\text{XRF}}$  is the amplitude of the fitted XRF signal,  $E_{K_\alpha}$  is the centre of the peak at the energy of the iodine  $K_\alpha$  fluorescence, and  $\sigma$  is the standard deviation defining the width of the Gaussian fit. A fit for the background around the signal is generated by similar Gaussian functions. Before the background is fitted, the counts within the bins of the signal region have to be removed from the spectrum. In this thesis the signal region is defined as

$$\text{XRF signal region} = E_{K_\alpha} \pm 3 \sigma_{\text{det}}, \quad (5.2)$$

where  $\sigma_{\text{det}}$  is the standard deviation of the detector resolution. The fit of the XRF signal and the background of the spectrum is illustrated in figure 5.1.



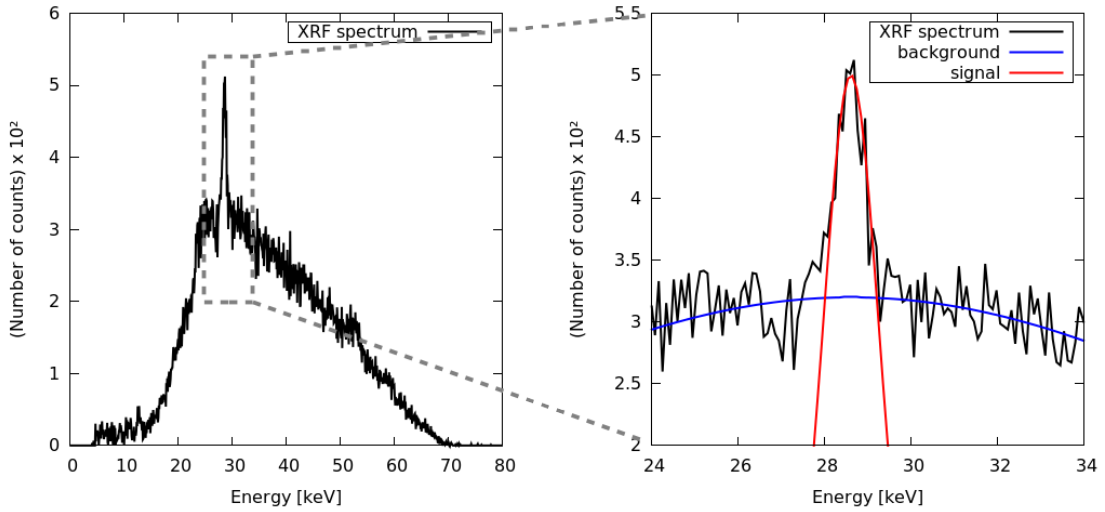


**Figure 5.1:** Example XRF spectra with fitting functions visualising the removal of the background and the isolation of the XRF signal.

## 5.2 Signal-to-noise ratio (SNR)

In this thesis the signal-to-noise ratio (SNR) is used as measure of the sensitivity of the used imaging system. It is defined as the ratio of the amplitude  $A_{\text{XRF}}$  of the fitted XRF signal to the standard deviation of the background  $\sigma_{bg}$ :

$$\text{SNR} = \frac{A_{\text{XRF}}}{\sigma_{bg}}. \quad (5.3)$$

This standard deviation of the background is defined as

$$\sigma_{bg} = \sqrt{\frac{\sum_{i=1}^{\mathcal{N}} (\mathcal{X}_i - \bar{\mathcal{X}})^2}{\mathcal{N} - 1}}, \quad (5.4)$$

where  $\mathcal{X}_i$  is the value of the  $i$ -th bin (e.g. the amount of counts within this bin),  $\bar{\mathcal{X}}$  is the mean value of energy bins, and  $\mathcal{N}$  is the number of energy bins used for the calculation.  $\sigma_{bg}$  is calculated outside of the signal region as defined in relation 5.2, using the *local* background, which comprises parts of the spectrum up to an arbitrarily chosen range of  $E_{K\alpha} \pm 9 \sigma_{\text{det}}$ . Before  $\sigma_{bg}$  is calculated, the background fitting function is subtracted from the spectrum.

It should be noted that this method of calculating the SNR is used for all experimentally derived results and simulated spectra reproducing the experimental results in this work (cp. chapter 10). Chapter 11 deals with larger energy bins, which is why a more simplified method is applied: All simulations are conducted with and without iodine. From the simulation with iodine, the value of the energy bin containing the XRF signal is used as signal amplitude  $A_{\text{XRF}}$ . From the simulation without iodine, the value of the same energy bin is used to calculate  $\sigma_{bg}$  by simply taking the square root of the value.

As a measure of whether an SNR is considered to be *acceptable*, serves the *Rose criterion* [64]. It states that an SNR of at least 5 is necessary in order to distinguish the signal from the background.

## Part II

# Experimental investigation



Part II is dedicated to the experimental realisation of the XRF imaging setup proposed in this work. All measurements were performed at Helmholtz Zentrum München (HMGU)<sup>1</sup>, Germany. Chapter 6 gives a detailed introduction to the radiation facility and materials provided by HMGU, which were used to generate all XRF spectra and X-ray dose values for this thesis. It also presents a detailed description of the powerful stripping algorithm developed for this work, which is indispensable for cleansing the recorded raw data. The results of the XRF measurements are discussed in chapter 7, including experiments with various phantom sizes, iodine concentrations and relative angular detector positions. This chapter concludes with measurements of the X-ray dose (air kerma) at the position of the object of investigation (phantom), performed with two ionisation chambers.

---

<sup>1</sup>Helmholtz Zentrum München GmbH, German Research Center for Environmental Health (HMGU)



## 6. Materials and methods

### 6.1 Experimental setup

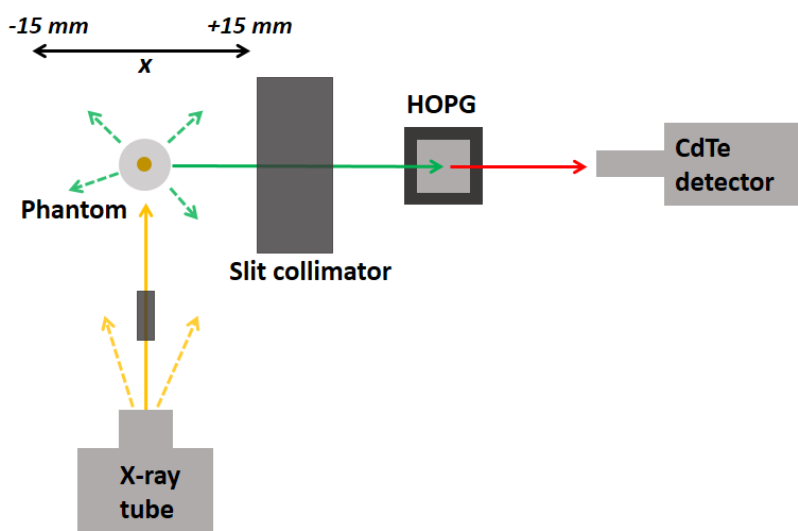


**Figure 6.1:** Top view scheme of a basic imaging setup for measuring the iodine X-ray fluorescence with and without an energy-selecting HOPG crystal. The X-rays (yellow) generated by an industrial X-ray tube are collimated by a hole collimator and directed towards a phantom where X-ray fluorescence is induced (green). Situated at a  $90^\circ$  angle relative to the beam hitting the phantom, a slit collimator cuts out non-radially directed spurious background radiation before the incident radiation hits the HOPG crystal. The crystal filters the radiation in terms of energy, suppressing the background radiation and emphasising the fluorescence signal (red) before it hits the sensitive area of the detector.

All experiments in this work have been conducted with an imaging setup which, due to simple modifications, facilitates viable comparisons between measurements including and excluding the HOPG crystal. The imaging system, as seen in figure 6.1, was built on a  $50 \times 50\text{ cm}^2$  Aluminium plate and the isocentre was positioned at a distance of 52 cm from the X-ray tube. At 33 cm between X-ray source and centre, a cylindrical hole collimator (diameter: 15 mm; length: 20 mm) consisting of lead was implemented in order to form a pencil beam with a diameter of 1 mm at the position of the phantom (isocentre). The used CdTe detector was placed at a  $90^\circ$  angle compared to the incident beam at a 21.5 cm distance from the phantom position. For the test series including the HOPG crystal, a goniometer (Owis, Staufen, Germany) with an

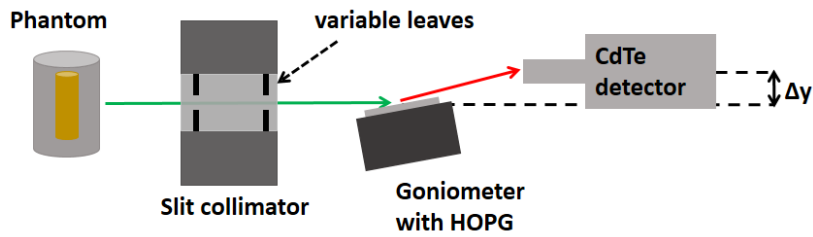


**Figure 6.2:** Side view schematic of the imaging setup: Fluorescence and multiple scattered photons (green) originating from the phantom, traverse the slit collimator before hitting the HOPG crystal at an angle of  $3.7^\circ$ . Bragg reflected photons are reemitted at a  $3.7^\circ$  angle before reaching the detector sensitive area. Therefore the detector has to be vertically shifted relative to the phantom. For measurements not including the HOPG crystal, the detector and phantom are positioned at the same vertical height.

angular adjustment accuracy of  $145 \mu\text{rad}$  ( $\approx 8.3 \cdot 10^{-3}^\circ$ ) according to the manufacturer was inserted at a distance of 3 cm from the detector. Attaching the HOPG to the goniometer surface enables precise angular alignment of the crystal relative to the phantom and the detector. Right next to the phantom a slit collimator consisting of aluminium and molybdenum was inserted in order to minimise the amount of photons hitting the detector area. This is advantageous for preventing count rate and hence dead time problems of the detector. The aluminium frame with dimensions  $10 \text{ cm} \times 10 \text{ cm} \times 5.5 \text{ cm}$  contains a total of four molybdenum plates, which form two pairs of variable leaves positioned on opposite sides, such that two adjoined slit-shaped gaps of alterable size and height can be adjusted to the demands of the experimental setup. This is a crucial feature since the two experimental setups, with and the one without the HOPG crystal, differ in their relative vertical phantom-detector position  $\Delta y$  (cp. figure 6.2). Moreover, in the case of the setup where the crystal is used, the upper collimator ensures that the scattered photon beam has to pass the crystal surface before hitting the detector sensitive area.

### 6.1.1 X-ray source and spectrum

All polychromatic X-ray spectra used in the experiments were generated by an industrial X-ray tube (MG160) by YXLON<sup>1</sup>, Hamburg, which is embedded in a setup installed by the Physikalisch-Technische Werkstätten<sup>2</sup> (PTW) in Freiburg, Germany. The whole system comprises a tabletop unit which can move relative to the X-ray tube, a filter wheel for various degrees of beam hardening and a collocation of laser pointers, enabling precise positioning of the probes to be irradiated relative to the isocentre. Focal apertures of various sizes can be installed at a distance of 30 cm to the anode focal point for collimating the primary X-ray beam. A monitor chamber at the same location provides a first estimate of the dose rate emitted by the X-ray tube.

<sup>1</sup>[www.yxlon.de](http://www.yxlon.de) (retrieved 1 May 2019)

<sup>2</sup>[www.ptw.de](http://www.ptw.de) (retrieved 1 May 2019)



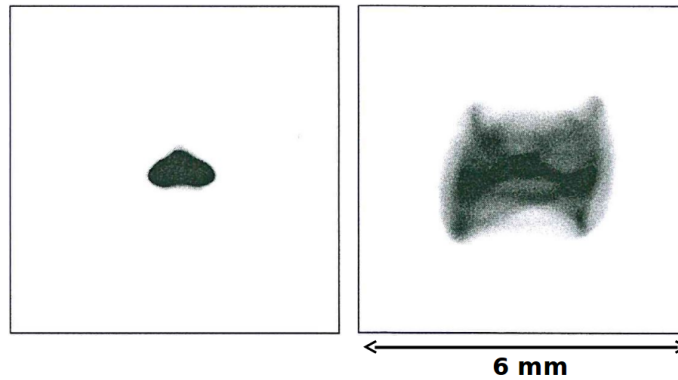


**Figure 6.3:** Anode focal spot sizes of the industrial X-ray tube MG 160 (Yxlon). Left: small focal spot with dimensions  $1.3 \text{ mm} \times 0.8 \text{ mm}$ . Right: large focal spot with dimensions  $2.9 \text{ mm} \times 2.4 \text{ mm}$ . Both spots have been measured on 28.09.2012. The edge length of each image equals 6 mm. Regions of high photon flux rates (dark) are clearly discriminable from regions of low flux rates (light).

The X-ray tube itself operates with a maximum peak kilo voltage of  $U_A = 160 \text{ kV}$  and a maximum electric current of  $I = 45 \text{ mA}$  (for 60 kV). The emitted X-radiation is pre-filtered by a beryllium window of 0.8 mm thickness. The mode of operation is based on a liquid-cooled tungsten anode with an angle of  $20^\circ$ . It offers two sizes of focal spots (FOC<sub>1.0</sub> and FOC<sub>5.5</sub>) displayed in figure 6.3 (left and right respectively). For the small focal spot FOC<sub>1.0</sub> the maximum electric current must be lower than for the large focal spot FOC<sub>5.5</sub> since the anode is heated above a critical temperature when the photon count rate exceeds a certain value. The larger spot consists of a larger area and consequently has the capacity to emit larger amounts of photons per second, while staying below the critical value for anode heating. Besides the intrinsic pre-filtering by the beryllium window, additional beam hardening is provided by a regularly gauged tunable filter wheel which generates a variety of beam qualities. Table 6.1 summarises all possible filter settings for the industrial X-ray tube used in this work and figure 6.4 shows example spectra generated with different filters: Filters influence the primary spectra by shifting the centroid and altering the FWHM of the polychromatic X-ray beam. However, the downside is that strong filters significantly reduce the photon flux.

In X-ray fluorescence it is preferable to utilise the highest possible electrical current in order to achieve satisfactory photon count statistics. However, due to the limit of the power output of the generator, the maximal applicable current decreases with increasing *peak kilo voltage* (kVp), which is the maximum applicable kilo voltage. Moreover, the minimum photon energy needed to induce X-ray fluorescence strongly depends on the element used as a contrast agent. For generating fluorescence photons in iodine the minimum photon energy has to be larger than the K-edge of iodine at about 33.168 keV. Consequently the peak kilo voltage of the X-ray tube has to be set such that the centroid of the polychromatic X-ray spectrum is clearly above the K-edge of iodine. Increasing the applied kVp, however, augments the probability of annihilation and obscuring of the XRF signal due to Compton photons. Similarly, broad polychromatic spectra decrease the XRF signal yield due to a large amount of

Filter	Material thickness [mm]
1	0.1 Al
2	0.5 Al
3	1.0 Al
4	2.0 Al
5	4.0 Al
6	4.0 Al + 0.2 Cu
7	4.0 Al + 0.6 Cu
8	4.0 Al + 2.0 Cu
9	4.0 Al + 5.0 Cu
10	4.0 Al + 5.0 Cu + 1.0 Sn
11	4.0 Al + 2.5 Sn

**Table 6.1:** All possible filter settings for the industrial X-ray tube MG 160 for generating spectra with various beam qualities.

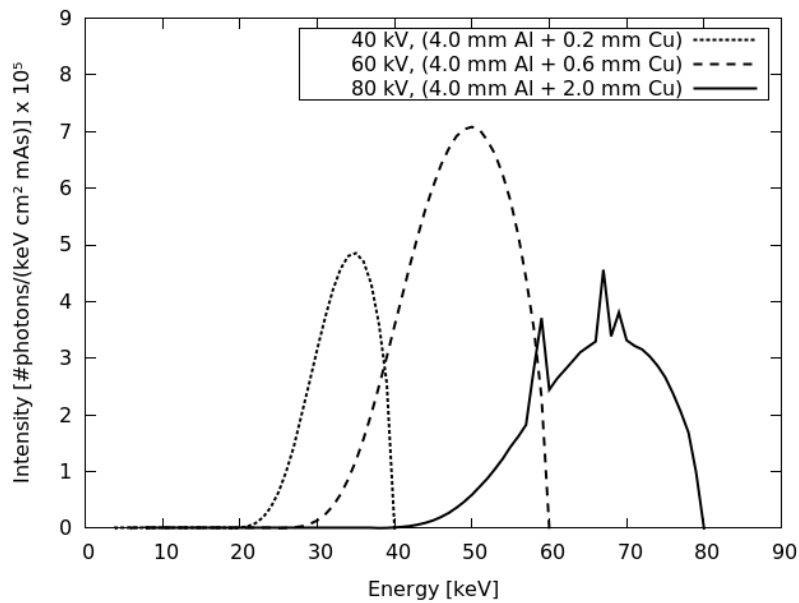


**Figure 6.4:** Example spectra generated with different high voltages and filters: The choice of applied voltage ( $U_A$ ) and filter, influences the shape, bandwidth (FWHM) and position of the centroid. For the 80 kV/(4.0 Al + 2.0 Cu) spectrum even the  $K_\alpha$  and  $K_\beta$  lines of the tungsten anode of the X-ray tube are clearly visible and potentially impair the measurements.

background photons. Hence the experiment with iodine demands a carefully chosen combination of peak kilo voltage and filtering in order to provide a narrow primary photon spectrum with the centroid energy a few electronvolts above the K-edge of iodine and sufficiently large photon count rate.

### 6.1.2 Phantoms

In order to produce iodine solutions of various degrees of concentration, pure iodine was diluted with PBS solution (phosphate-buffered saline), a buffer solution commonly used in biological research due to its neutral pH and iso-osmoticity and isotonicity with the human body. Thus, solutions with iodine concentrations ranging from 0.1  $\mu\text{g}/\text{ml}$  to 5.0  $\text{mg}/\text{ml}$  were generated.

#### Phantom 1 and Phantom 2

For the XRF measurements two different kinds of phantom were used, a very basic test tube, and a slightly more elaborate PMMA cylinder. The former is a cylindrical Eppendorf<sup>3</sup> test tube, made of synthetic plastic (polypropylene) and has a volume of 0.2 ml (cp. figure 6.5, left). The second XRF phantom is a cylinder composed of PMMA (polymethyl methacrylate) with a length of 60 mm and a diameter of 30 mm, thus comprising a volume of roughly 42.4  $\text{cm}^3$  (cp. figure 6.5, middle). The dimensions were chosen such that the phantom approximately resembled the size of a mouse. Its interior comprises an empty volume of approximately 0.2 ml in order to be able to insert the above mentioned Eppendorf test tubes.

#### Phantom 3

For a more detailed investigation of the angular dependency of the Compton background (cp. section 7.1.3), an additional larger phantom was deployed (figure 6.5, right). Its dimensions are 55 mm in height and 100 mm in diameter and the material is PMMA like the XRF phantom described above. Comparing the Compton background of phantom 2 to that of phantom 3, enables conclusions about the influence on the object sizes.

### 6.1.3 HOPG crystal

For the measurements including an energy-selective HOPG crystal, a crystal with dimensions of  $50 \times 50 \times 2 \text{ mm}^3$  was used. Its individual graphite crystallites are aligned to each other, such that the width of their angular distribution, or *mosaic spread*, is roughly  $0.4^\circ$ , giving the HOPG crystal an integrated reflectivity of up to 50 % in the energy range between 20 and 30 keV. The basis for studying the diffraction on crystal lattices is the Bragg condition as explained in 4.1. For HOPG crystals with a mosaicity of  $0.4^\circ$  the lattice spacing  $d$  is known to be 3.354 Å.  $K_\alpha$  fluorescence of iodine

<sup>3</sup>[www.eppendorf.com](http://www.eppendorf.com) (retrieved 1 May 2019)

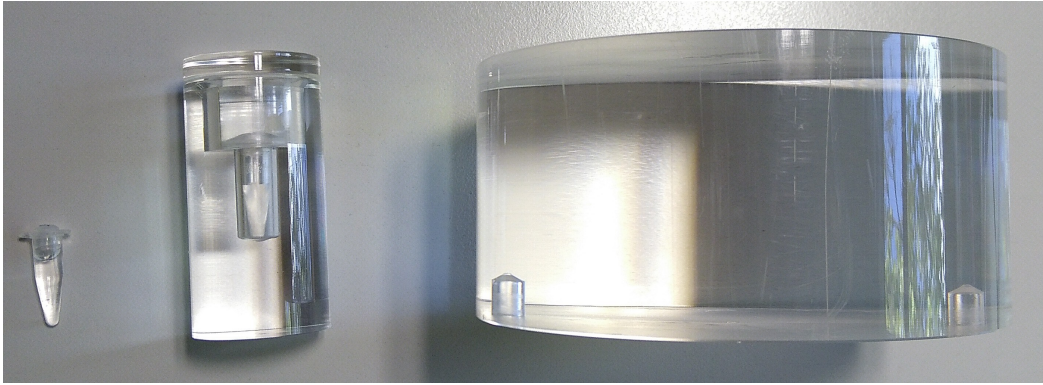


**Figure 6.5:** From left to right: Eppendorf test tube with a volume of 1.5 ml, filled with an iodine solution (phantom 1); more complex cylindrical PMMA/mouse Phantom (length: 60 mm, diameter: 30 mm) with an opening in order to insert Eppendorf test tubes with various iodine solutions (phantom 2); large PMMA Phantom (length: 55 mm, diameter: 100 mm) for studies on the background distribution (phantom 3).

is emitted at an energy of  $E = 28.6$  keV. For the first reflection order ( $n = 1$ ) of the lattice plane with the highest reflected intensity (002-plane), these values yield a Bragg angle of approximately  $3.7^\circ$  [65]. As a consequence, photons with energies around  $E = 28.6$  keV hitting the HOPG-002-crystal at an angle of  $3.7^\circ$ , are likely to be reflected by the crystal plane, whereas other angles of incidence and other photon energies are predominantly absorbed or transmitted. The reflection properties of the crystal plane with the second highest reflectivity (5 - 10%), the 004-plane, are calculated using the second order ( $n = 2$ ) Bragg condition. It turns out that this plane mainly reflects photons with an energy of about  $E = 57.2$  keV, if they hit the crystal at a Bragg angle of  $3.7^\circ$ . For each crystal plane an upper limit for the width of the reflection curve, or *energy resolution* (FWHM)  $\Delta E$  is determined by the relation 4.4 in section 4.2. With a reported value of 26 arcs ( $1 \text{ arcs} = (1/3600)^\circ$ ) for the HOPG 002-plane [63]  $\Delta E$  calculates to about 3.2 keV for the first reflection order of the HOPG crystal. The reflection curve for the 004-plane, i.e. the second reflection order, calculates to a maximum width of  $\Delta E = 6.4$  keV. However, due to the mentioned non-negligible focusing errors leading to further broadening, in practise the reflection curve exhibits a bandwidth of approximately 5 keV in the 002-plane and roughly 10 keV in the 004-plane.

#### 6.1.4 CdTe semiconductor detection system

The detection system used for this work comprises a XR-100CdTe X-ray detector (cp. figure 6.6) together with a preamplifier by Amptek<sup>4</sup> (Bedford, MA, USA). The  $3 \times 3 \times 1 \text{ mm}^3$  detector diode is placed behind a  $100 \mu\text{m}$  beryllium (Be) window and consists of cadmium telluride (CdTe), a compound semiconductor material with a wide bandgap (4.4 eV), high density ( $6.2 \text{ g/cm}^3$ ) and high atomic number  $Z$  (48.52). As a consequence, the stopping power of incoming radiation and charge transport is very high compared to many other semiconductor detectors.

<sup>4</sup>[www.amptek.com](http://www.amptek.com) (retrieved 1 May 2019)



**Figure 6.6:** Photo of the used semiconductor XR-100CdTe X-ray detector. On the upper right is a 1 cent Euro coin in order to give an impression of the detector size.

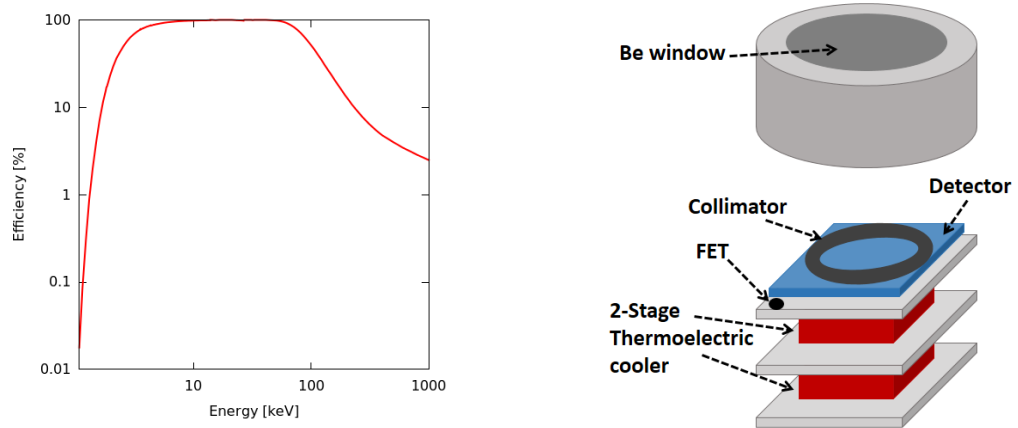


**Figure 6.7:** Left: Efficiency of the CdTe detector in logarithmic scale. The data is taken from the website of the manufacturer [www.amptek.com](http://www.amptek.com) (retrieved 1 May 2019). Right: Detailed structure of the CdTe detector.

The high efficiency between 10 and 50 keV as displayed in figure 6.7 (left), however, is a result of an applied voltage of +500 V supporting the charge collection. This in turn induces an increased temperature producing leakage currents and eventually leading to break down. Therefore the whole detection system is mounted on a two-stage thermoelectric (Peltier) cooler, which has been reported to significantly improve the charge transport [66] (cp. figure 6.7, right). This cooling system is also beneficial for the input field-effect transistor (FET) to the charge sensitive amplifier in that it further reduces leakage currents and increases the transconductance. As a result, electronic noise is minimised. A part of the current feedback network to the preamplifier and the feedback capacitor are also placed on the cooled substrate, which additionally suppresses parasitic capacitance at the input. Another large benefit of this CdTe detector model is that it has Schottky contacts of platinum (Pt, 200 nm, cathode) and indium (In, 100 nm, anode). Besides additionally reducing the leakage current [67], it has been reported that with thin (0.5 mm) CdTe detectors equipped with Schottky diodes, no hole tailing was observed at energies of more than 100 keV [68, 69]. The manufacturer specifies an energy resolution of less than 1.5 keV (FWHM) at about 122 keV and a dark count rate of less than  $5 \cdot 10^{-3}$  cps (*counts per second*) within an energy range between 10 keV and 1 MeV. Power to the whole detection system is provided by Amptek's PX5, a DC powered variable digital pulse amplifier with 0.2  $\mu$ s to 100  $\mu$ s peaking time. The PX5 functions as an interface between the detector

and the user's computer, processing the data from the digitisation of the preamplifier output to the generation of an energy spectrum. For more details on specification and mechanics the interested reader is referred to the Amptek webpage and to the various application notes dealing with specific detector effects such as charge transport [54], escape events [70], and efficiency [71].

## 6.2 X-ray dose measurement and estimation

For thoroughly scrutinising the proposed X-ray fluorescence imaging system it is essential to derive information about the radiation dose applied to the phantom. The integrated monitor chamber provides a rough estimate of the dose rate in terms of electric charge per second [C/s] at a distance of about 30 cm to the anode. However, this value severely deviates from the value to be expected at the phantom position since the monitor chamber is not calibrated to the used spectrum. Moreover, the phantom position is situated further away from the X-ray tube than the monitor chamber. The  $1/r^2$  relation defining the attenuation of radiation is only valid for finite point sources, which is not the case for X-ray tubes. Therefore, a value for the dose at the position of the phantom cannot be derived from the value measured by the monitor chamber. Moreover, the size of the X-ray beam in the XRF setup is reduced to a pencil beam of 1 mm in diameter by a hole collimator which is positioned behind the monitor chamber. Therefore only an indeterminable fraction of photons that have been recorded in the chamber will reach the phantom position. Another uncertainty to the dose introduces the anode spot, independently of which focal spot size is used. It does not emit photons isotropically and can change its emission properties with time due to abrasion. The image of both spots taken in 2012 (figure 6.3) shows areas of increased photon emission (dark) and those of reduced photon emission (light). Therefore, due to the lack of information about how many photons per second leave the X-ray tube at each pixel of the anode spot, it is impossible to predict the amount of photons per second that pass through the hole collimator. Nevertheless, it is possible to at least derive an approximation of the order of magnitude of the applied dose by measurements and calculation. Both estimation schemes used in this work will be explained in the following sections.

### 6.2.1 Dose measurement with ionisation chamber

This work makes use of two different ionisation chambers of volume  $0.6 \text{ cm}^3$  (Q 16) and  $30 \text{ cm}^3$  (Q 30), together with a PTW Unidos webline electrometer (Physikalisch-Technische Werkstätten Freiburg<sup>5</sup>), in order to determine the dose in terms of air kerma [Gy] at the position of the phantom. Ionisation chambers are based on the principle of gas detectors (cp. section 3.2.1) and count the amount of charge  $Q$  [C] in the radiation field of the X-ray tube by means of ionisation of a gas. From the total measured charge the air kerma can be calculated using various calibration factors that are different for each ionisation chamber, since they compensate for the volume and

<sup>5</sup>[www.ptw.de](http://www.ptw.de) (retrieved 1 May 2019)

material of the used ionisation chamber. Consequently, the resulting air kerma is expected to be equal for each ionisation chamber. Also the size of the X-ray beam has no influence on the value for the air kerma at the position of the phantom. However, for a reliable measurement it is important to cover the whole ionisation chamber with the X-ray beam during the entire measurement. Therefore, the hole collimator forming the narrow pencil beam used for the XRF experiments was demounted.

For each ionisation chamber the charge is collected in the following way: The chamber is mounted at a distance of about 52 cm from the X-ray tube, which is the exact position of the phantom in the XRF measurements. In order to determine a reliable value of the amount of collected charge, the average value is derived from a series of at least ten separate charge measurements. Each single measurement records the charge for a time of 60 seconds. Before and after the whole test series the environmental temperature  $T$  [°C] and air pressure  $p$  [hPa] are logged in order to calculate the air density correction factor  $K_\rho$ . Moreover, a null measurement of 60 seconds, collecting the charge without running the X-ray source, needs to be performed before and after the entire test series. The average of both null measurements  $Q_a$  is subtracted from each charge measurement  $Q_i$ . For each charge measurement the corresponding value for the air kerma  $K_i$  is calculated via

$$K_i = (Q_i - Q_a) \times N_k \times K_Q \times K_\rho \times K_E. \quad (6.1)$$

The individual factors of this equation are partly taken from the calibration certificates [72, 73] and are described as follows:

- $Q_a$  is the average value of the null measurements recorded before and after the measurements series.
- $N_k$  is the calibration factor for the air density specific to the individual ionisation chamber.
- $K_Q$  is an ionisation chamber specific factor of order unity and can be taken from the calibration document provided by the manufacturer.
- $K_\rho$  depicts the air density correction factor and is calculated using the average values of temperature  $T$  and pressure  $p$  recorded before and after the measurement series:  $K_\rho = (273.15 + T)/293.15 + 1013.25/p$
- $K_E$  is a factor specific to the used electrometer which is equal to one for the PTW unidos weblin dosemeter used in this work.

The results from dose measurements are used to calibrate X-ray spectra analysis programmes, such as SpekCalc which will be introduced in the next section. Consequently, the programme can calculate dose rates of other beam qualities obtainable with the industrial X-ray tube used in this work. Moreover, SpekCalc enables the generation of suitable spectra that can be used in theoretical investigations with Monte-Carlo simulations, which will be the topic of part III: *Monte Carlo Simulation GEANT4*.

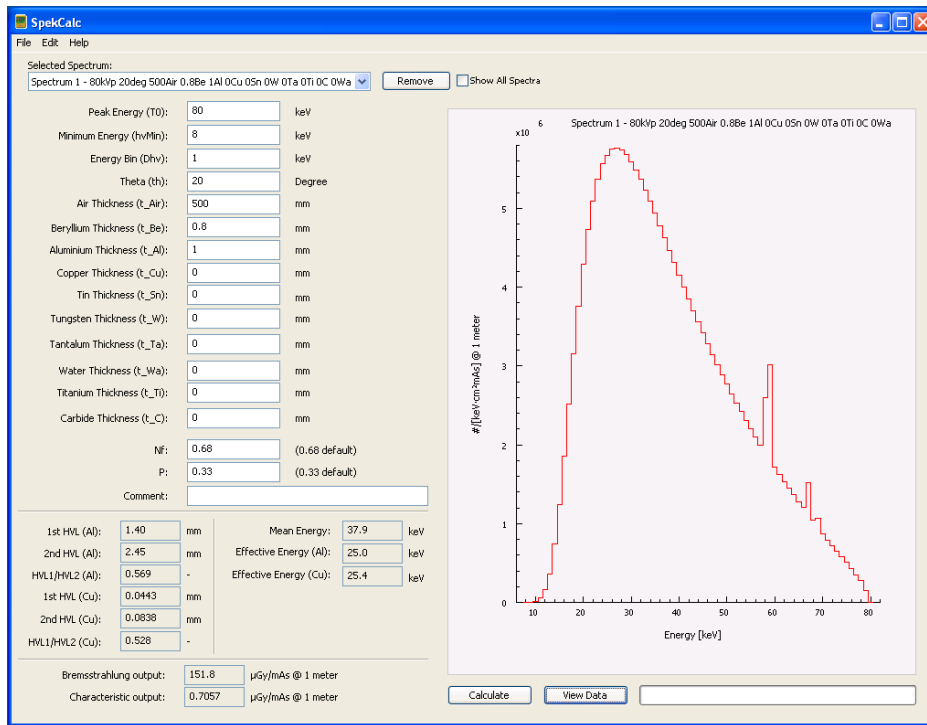


**Figure 6.8:** *SpekCalc* graphical user interface for generating a spectrum with various settings, such as voltage, energy bin, anode angle and filtration. A spectrum with the properties  $U_A = 80$  kV and a 1.0 mm Al filtration has been generated with the default settings for the ratio between characteristic X-rays and bremsstrahlung  $P$ , and the fluence rate changing factor  $N_f$ .

### 6.2.2 Dose estimation via calculation with SpekCalc

For the calculation of additional beam qualities apart from that experimentally measured with the ionisation chambers, this work made use of the open source programme SpekCalc<sup>6</sup> [74]. The programme computes X-ray spectra from tungsten anode X-ray tubes, based on semi-empirical models [75] and Monte Carlo calculations [76, 77]. It produces reliable results for tube potentials of 40 - 300 kVp and anode angles of 6 - 30° and offers pre-filtering for the following materials: air, water, beryllium, aluminium, copper, tin, tungsten, tantalum, titanium and carbide. Apart from the high voltage  $U_A$ , energy bin size, anode angle and filtration, the user can adjust the two additional factors  $N_f$  and  $P$  according to the demands of the task.  $N_f$  normalises the fluence and is useful for modifying the dose rate.  $P$  is the ratio of intensity of characteristic X-rays to bremsstrahlung. Figure 6.8 displays the graphical user interface of the programme including the input and output parameters, where the input factors correspond to a spectrum with  $U_A = 80$  kVp,  $I = 37.5$  mA and a 1.0 mm Al filtration. In order to gauge SpekCalc according to the used X-ray tube, the factor  $N_f$  has to be determined such that the calculated air kerma equals the measured air kerma. The former is calculated from SpekCalc using the sum of the bremsstrahlung and characteristic output together with information about radiation time and electric current.

<sup>6</sup><http://spekcalc.weebly.com/> (retrieved 1 May 2019)



It has to be noted that the results provided by SpekCalc are still an approximation for the air kerma given by the industrial X-ray tube used in this work. Factors such as the bremsstrahlung to characteristic radiation ratio, the optical spot and the distance to the source impair optimal dose estimations.

## 6.3 Spectrum correction methods

The various detector effects described in chapter 3 can have a strong influence on the shape of the recorded spectrum. However, these effects do not necessarily constitute a serious problem for every kind of experiment. Factors such as detector and radiation type or energy range dictate the spectrum distorting effects that have to be considered when analysing measured spectra. For XRF measurements, for example, the distortion due to dead time effects does not constitute a serious problem, since detector count rate limitations are hardly exceeded. Nevertheless, for all experimentally obtained spectra the number of counts  $N_{ex}$  has to be corrected accounting for dead time and detector efficiency, according to

$$N_{int} = N_{ex} \cdot \frac{100\%}{100\% - DT[\%]} \cdot \eta_{tot}(E). \quad (6.2)$$

The second term corrects for dead time effects  $DT$  and  $\eta_{tot}(E)$  is the efficiency function, which in many cases is published by the manufacturer. As for the CdTe detector the efficiency is very high for energies between 10 and 50 keV (figure 6.7, left). However,  $\eta_{tot}(E)$  as given by the manufacturer does not account for escape events, which for semiconductor detectors constitute the dominant effect of spectral distortion in the energy range of interest. Therefore the number of *corrected* counts in equation 6.2 is denoted with  $N_{int}$ , standing for an *intermediate* result.

### 6.3.1 The stripping algorithm

For the semiconductor detectors and radiation energies used in this work the predominant cause for distortions are escape events. Escape events occur when a photon with a certain energy interacts with the detector material such that only a part of the incident energy is deposited and processed and the remaining part escapes as a scattered photon and can be reabsorbed by the detector material. As a consequence, the original photon energy will not be represented in the recorded energy spectrum. Instead there will be two measurements at lower energies. This effect leads to a plateau of photon counts at lower energies. In order to cleanse the spectrum from spurious escape signals a suitable algorithm known as a *stripping method* [78] needs to be applied and will be explained as follows.

The first step for building a suitable stripping algorithm for a specific detector is to calculate the detector *response function*, since it is necessary to identify distortions due to escape events, transmission of primary X-rays and carrier trapping, also known as *hole tailing*. However, hole tailing does not constitute a serious problem in this work,

	K-edge	$K_{\alpha_1}$ [keV]	$K_{\alpha_2}$ [keV]	$K_{\beta_1}$ [keV]	$K_{\beta_2}$ [keV]
Cd	26.7	23.0	23.2	26.1	26.6
Te	31.8	27.2	27.5	31.0	31.7

**Table 6.2:** The constituents of CdTe, Cadmium and Telluride, with the energies of the K-edges and the characteristic X-ray  $K_{\alpha}$  and  $K_{\beta}$  energies.

since it has been shown that the effect for a semiconductor CdTe detector is negligible for energies below 50 keV [79] and non-existent for energies below 40 keV [80].

For building the stripping algorithm, this work makes use of the results of Tomal et al. [80–82], which were obtained as follows: In the first step a Monte Carlo code is used in order to determine the response function of the CdTe detector accounting for intrinsic and photopeak efficiency, i.e. transmission and escape events respectively. For this, monoenergetic simulations are carried out for energies between 5 to 120 keV in intervals of 0.5 keV. For each simulation  $10^6$  photons are emitted in a narrow collimated beam (pencil beam) and directed towards the CdTe detector which is implemented within the code according to the specifications given by the manufacturer (cp. subsection 6.1.4). Every incident photon and all secondary photons are tracked and for each interaction of the particles inside the detector material the deposited energy is recorded. The result allows for calculating the full-energy absorption efficiency, i.e. the ratio of counts in each escape peak to the photopeak as a function of the incident energy. The CdTe detector generates four escape peaks originating from the  $K_{\alpha}$  and  $K_{\beta}$  fluorescence lines of Cadmium (Cd) and Telluride (Te), which are summarised in table 6.2. The calculated ratios for each escape peak are fitted by a polynomial and are displayed in figure 6.9. Since the X-ray emission probability of  $K_{\alpha}$  photons is larger than that for  $K_{\beta}$  photons, the escape fraction for the former is higher. Also with increasing incident photon energy the necessary escape event correction decreases which can be explained with the decreasing interaction probability via the Photoelectric effect.

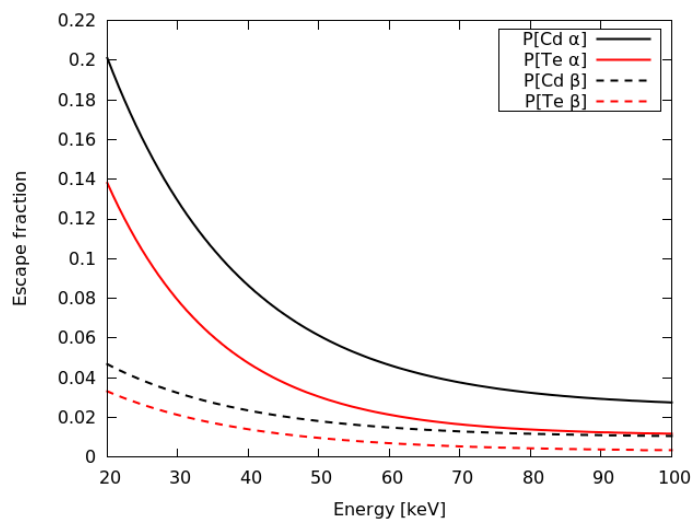


**Figure 6.9:** Polynomials derived from the ratios between escape peak to photopeak for each escape peak of K-shell electrons of Cadmium and Telluride,  $Cd_{\alpha}$ ,  $Cd_{\beta}$ ,  $Te_{\alpha}$  and  $Te_{\beta}$ . The data is taken from Tomal et al. [80–82].

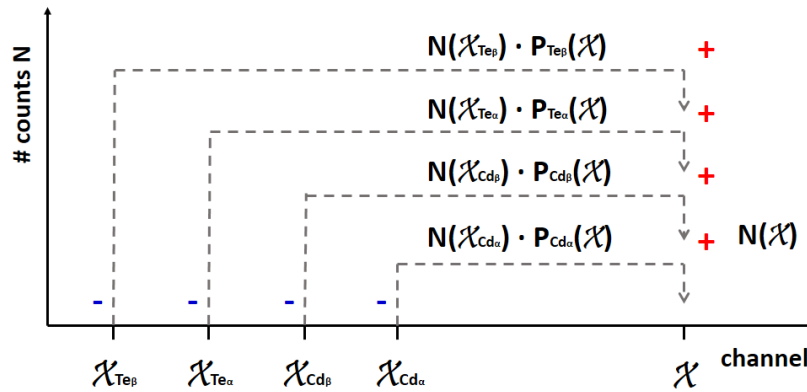


**Figure 6.10:** Illustration of the procedure of the stripping algorithm for an CdTe detector.

The correction algorithm assumes the spectrum is recorded with a perfect detector regarding energy resolution, meaning that it neglects Gaussian broadening. It begins with the highest energy channel and treats it as a one channel photopeak. For this channel the four escape peaks are determined and the ratio of escape to photopeak counts are computed using the four polynomials displayed in figure 6.9. These counts are subtracted from the escape channels and added to the photopeak channel. The processed spectrum is now the basis for repeating this procedure for the next lower energy channel. This method is applied channel by channel proceeding down to the Cd escape edge. Figure 6.10 illustrates the procedure starting with the highest photopeak channel  $\mathcal{X}$ . The corresponding escape channel for the Te  $K_\beta$  fluorescence is at the position  $\mathcal{X}_{Te_\beta} = \mathcal{X} - 31.0$  keV. The number of counts in this channel  $N(\mathcal{X} - 31.0$  keV) is multiplied with the polynomial  $P_{Te_\beta}(\mathcal{X})$  for the Te  $K_\beta$  escape fraction at the position  $\mathcal{X}$  and then added to the number of counts  $N(\mathcal{X})$  at position  $\mathcal{X}$ . The same applies for the other escape channels. Figure 6.11 shows the effect of the stripping algorithm for an experimentally recorded spectrum (grey coloured line) from a 80 kVp tungsten anode and filtering with 1 mm Al. A plateau of low energy counts below 20 keV is clearly visible, which originates from multiple Compton scattered photons and escape events within the detector material. The blue line shows the counts of escape events being subtracted by the stripping algorithm from the spectrum, whereas the red line displays the counts that have been added to their appropriate energy channels. The final corrected spectrum (black) still exhibits counts below approximately 20 keV, which partly arise from multiple scattered Compton events. However, a certain fraction of these counts may stem from the simplifying assumption that have been made to the algorithm: The escape events have distinct energies and are hence a line process. Also the correction algorithm assumes a line process. However, the peaks in the recorded spectrum are subject to Gaussian broadening. An excerpt of the stripping algorithm developed in the framework of this thesis is displayed in Appendix V.A.

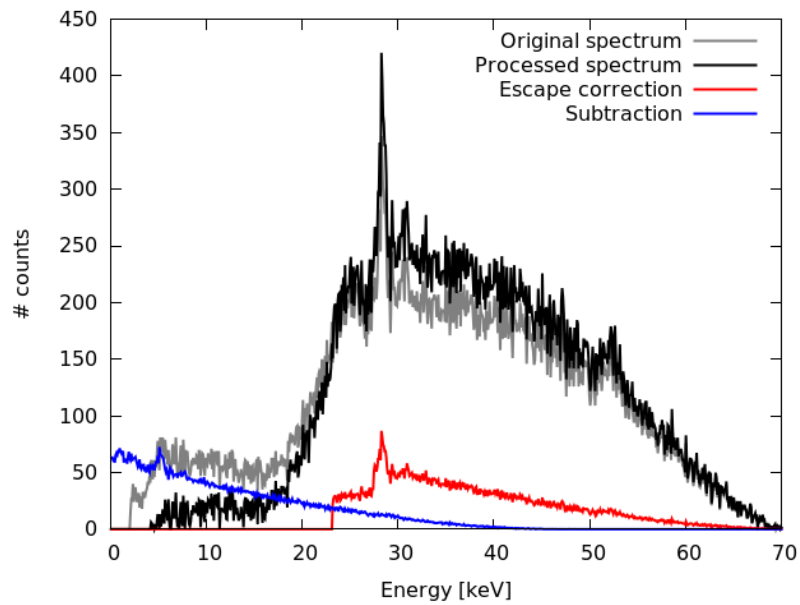


**Figure 6.11:** Example of an escape corrected X-ray spectrum: Shown in grey is the original spectrum. Escape events have been subtracted (blue) and added as escape correction (red). The final spectrum is shown in black.

## 7. Results: measurements of X-ray spectra

This chapter presents the results of the experimental implementation of the XRF imaging setup proposed in this work. All XRF experiments have been performed with and without incorporating the HOPG crystal in order to test its feasibility and to have a substantial database for the GEANT4 simulations which will be introduced in the third part of this work. Prior to detailed analyses, all recorded spectra have been processed according to the methods described in section 6.3. Section 7.1 deals with *preliminary* measurements, investigating suitable beam qualities for XRF measurements, and deriving the optimal initial X-ray spectrum for this work. Moreover, measurements with various angular detector positions relative to the X-ray source are studied for the most prominent initial beam quality. In section 7.2 XRF signals are recorded for various iodine concentrations for both the simplified Eppendorf phantom (phantom 1) and the slightly larger PMMA/mouse phantom (phantom 2). Finally this chapter concludes with air kerma measurements of the derived initial source spectrum used for all subsequent XRF measurements (section 7.3).

### 7.1 Preliminary measurements with various beam qualities

As described before, conventional X-ray tubes generate broad polychromatic energy spectra. An adequate combination of high voltage  $U_A$  and pre-filtering can optimise the XRF signal yield. As follows, various beam qualities are investigated in order to derive the most suitable initial spectrum for subsequent XRF measurements in terms of SNR and applied X-ray dose.

#### 7.1.1 Influence of applied high voltage $U_A$

The applied high voltage  $U_A$  defines the energy threshold of the upper end of the energy spectrum. Using iodine as a contrast agent in XRF measurements requires an initial spectrum where the majority of photons has an energy clearly above the K-edge of iodine ( $E_{K\text{-edge}} \approx 33.2$  keV), such that X-ray fluorescence can be generated. Therefore, the high voltage should be chosen such that the centroid of the spectrum is situated around the K-edge. However, the caveat of working with polychromatic spectra is the non-negligible amount of photons within the energy range between centroid and maximum photon energy, which significantly impairs the resulting spectra by enhanc-

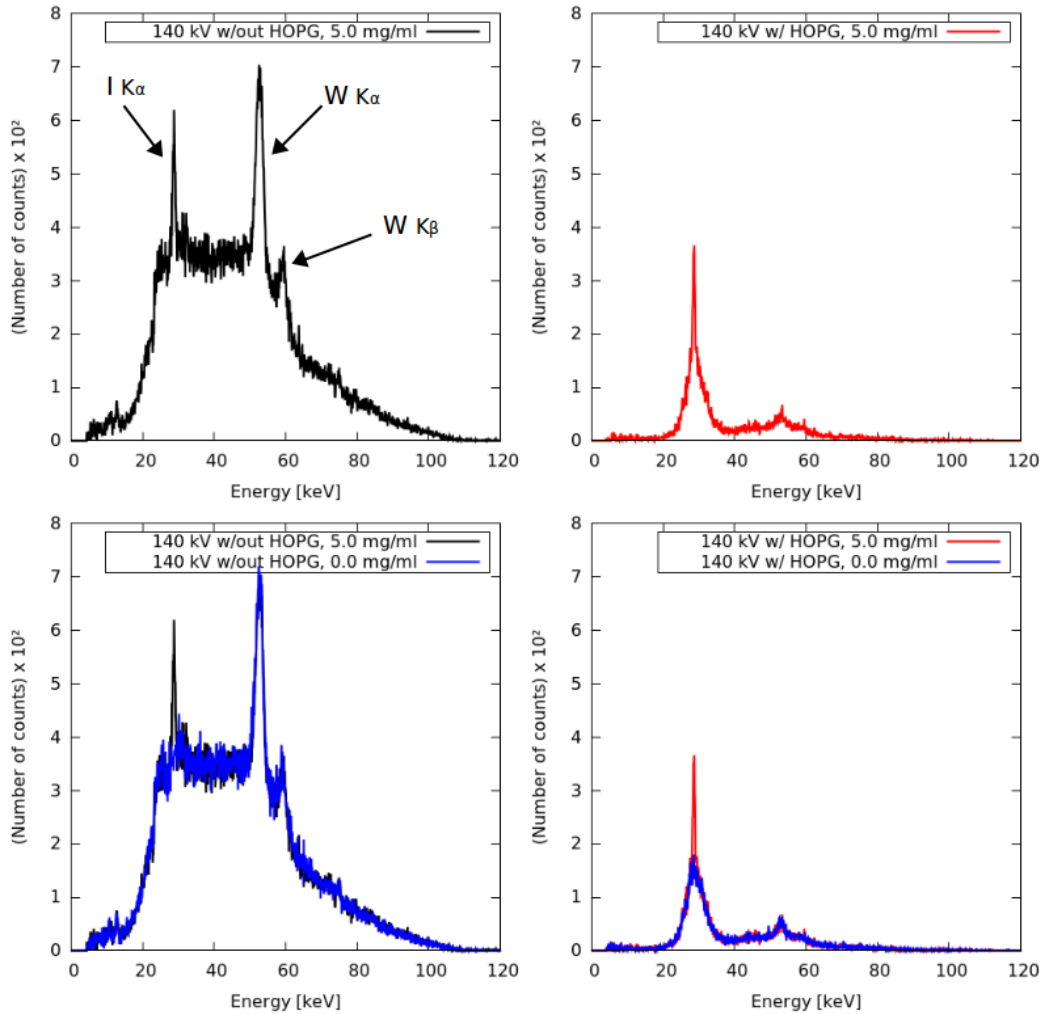


**Figure 7.1:** XRF spectra without (left) and with (right) HOPG generated with an initial spectrum of 140 keV/(1.0 Al) and a contrast agent concentration of 5.0 mg/ml (top). For comparison the spectra at the bottom additionally include measurements without contrast agent.

ing the amount of spurious background signals. Moreover, implementing the HOPG crystal at an angle of  $3.7^\circ$  in order to emphasise the iodine XRF signal, introduces second order reflections in the energy range around 57.2 keV. Consequently the upper energy limit defined by the high voltage should be chosen such that the photon flux around 33.2 keV is sufficiently large, while the photon flux at about 57.2 keV is kept rather low.

In order to decide on a suitable high voltage  $U_A$  various XRF measurements have been performed and compared to each other with regard to X-ray dose at the isocentre and SNR. The large anode spot was employed since it locally produces a larger photon flux compared to the small anode spot and hence yields improved counting statistics. In order to further improve the mentioned counting statistics, the recording time was set to 120 seconds. For all recordings a  $90^\circ$  detector configuration was implemented and the PMMA/mouse phantom (phantom 2) was used with an iodine concentration of 5.0 mg/ml. For the purpose of comparison and isolating the net XRF signal, additional

		<i>w/o HOPG</i>		<i>w/ HOPG</i>	
$U_A$ [kV]	dose [Gy]	SNR		SNR	
<b>40</b>	0.96	$1.98 \pm 0.70$	( $\pm 35.4\%$ )	$1.67 \pm 0.88$	( $\pm 52.7\%$ )
<b>60</b>	1.79	$5.76 \pm 1.41$	( $\pm 24.5\%$ )	$4.57 \pm 1.63$	( $\pm 35.7\%$ )
<b>80</b>	2.12	$9.81 \pm 2.11$	( $\pm 21.5\%$ )	$8.28 \pm 2.12$	( $\pm 25.6\%$ )
<b>100</b>	2.18	$8.63 \pm 1.12$	( $\pm 13.0\%$ )	$8.10 \pm 2.49$	( $\pm 30.7\%$ )
<b>120</b>	2.22	$9.53 \pm 2.06$	( $\pm 21.6\%$ )	$7.92 \pm 2.45$	( $\pm 30.9\%$ )
<b>140</b>	2.24	$9.36 \pm 2.20$	( $\pm 23.5\%$ )	$8.27 \pm 2.54$	( $\pm 30.7\%$ )
<b>160</b>	2.25	$9.99 \pm 2.14$	( $\pm 21.4\%$ )	$8.23 \pm 2.52$	( $\pm 30.6\%$ )

**Table 7.1:** Results of XRF measurements without and with HOPG produced with various beam qualities with high voltages from 40 to 160 kV in steps of 20 kV. The 1.0 mm Al filter was used for all spectra. The initial X-ray dose remains the same for measurements without and with implementing the HOPG. The SNR is provided with its absolute error and the percentage in parentheses represents its relative error.

measurements without iodine were included. A filter of 1.0 mm Al was chosen for suppressing initial low-energy photons significantly below the K-edge of iodine. All experiments were performed with and without including the HOPG crystal. The chosen filter was kept fixed, while the high voltage was modified with each measurement in steps of 20 kV from 40 to 160 kV.

The top row of figure 7.1 displays XRF spectra without and with the HOPG (left and right respectively) each generated with an initial spectrum including the above specifications and an applied high voltage of  $U_A = 140$  kV. The bottom row additionally includes spectra recorded with the same settings but using a contrast agent concentration of 0.0 mg/ml (i.e. no iodine). The resulting spectra exhibit a clear XRF signal around 28.6 keV and two signals from the  $K_\alpha$  and  $K_\beta$  emission lines of the tungsten anode. These spectra demonstrate the effect of the HOPG crystal: In an energy range around the  $K_\alpha$  fluorescence line of iodine, the 002-plane of the crystal reflects nearly 50% of the resulting background photons of the XRF spectrum. Likewise the 004-plane of the HOPG crystal reflects about 5 - 10% of the photons in the region around 57.2 keV. All other energies are considerably suppressed. However, the iodine XRF signal height in the resulting spectrum including the HOPG, is reduced not only by 50% compared to the spectrum without HOPG, but is notably larger than predicted. However, the relative statistical error of 30.7% for the spectrum including the HOPG is larger than the error for the spectrum without the crystal (23.5%). This is a consequence of a tremendously reduced photon flux due to the experimental setup, which includes a hole collimator, a slit collimator, an quasi-monochromatising device (for the case including the HOPG crystal) and a detector with a minimum angle coverage of only  $9 \cdot 10^{-4}$  rad ( $\cong 7.2 \cdot 10^{-3}\%$  of the full solid angle  $\Omega$ ).

Table 7.1 summarises the results for each high voltage  $U_A$ , displaying the applied X-ray dose and SNR for both experimental setups without and with the implementation of the HOPG crystal. The dose was measured and calculated following the scheme as explained in sections 6.2.1 and 6.2.2. The maximum applicable electric current  $I$  decreases for increasing high voltages  $U_A$ . This is reflected in the X-ray dose, which

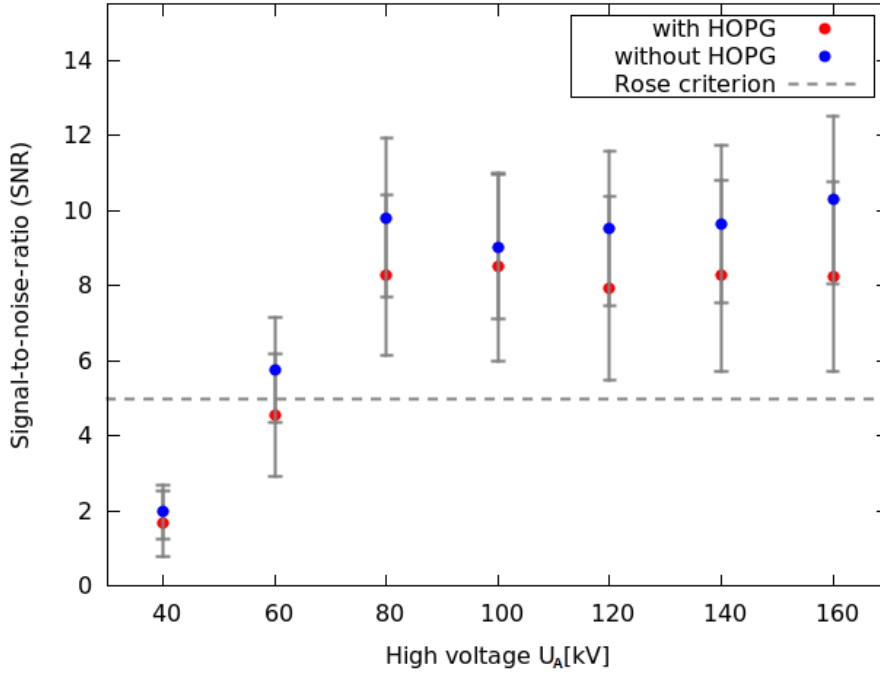


**Figure 7.2:** SNR of recorded XRF spectra produced with various high voltage configurations. All initial spectra were filtered with 1.0 mm Al. The measurements were performed with the PMMA/mouse phantom including an iodine concentration of 5.0 mg/ml.

increases with  $U_A$ , but stagnates at very high values for the high voltage. Figure 7.2 displays the SNRs for measurements with and without HOPG crystals, including a grey dashed line for the *Rose criterion* (cp. section 5.2). The SNRs for the experimental setup including the HOPG crystal are generally smaller than those for the setup without HOPG, albeit the relative ratios between signal height and background height show no difference for both setups. This is due to the way of calculating the SNR which considers the increasing statistical error for decreasing amounts of counts in the energy spectrum. Since the HOPG reduces the amount of counts by roughly 50% in the energy region of interest (EROI), this effect is particularly apparent. For both setups, an initial high voltage of  $U_A = 40$  kV leads to XRF results with an SNR below the Rose criterion, thus being discarded as candidate for subsequent XRF measurements. Also, an initial spectrum with  $U_A = 60$  keV yields SNRs not clearly satisfying the Rose criterion. Other values for  $U_A$  lead to SNRs significantly above the Rose criterion with no significant trend for increasing high voltages. This result correlates with the applied X-ray dose which increases rapidly for very low values of  $U_A$  but stagnates at values larger than  $U_A = 80$  kV. Besides the applied X-ray dose the shape of the initial spectrum decisively influences the recorded results: The centroid of the 40 kV spectrum is significantly below the energy of the iodine K-edge. Consequently, most photons of the initial spectrum have energies below the excitation energy for generating X-ray fluorescence of iodine. This leads to a decreased relative ratio between background and XRF signal photons, and consequently a low SNR.

This effect is demonstrated in figure 7.3, where the initial spectra with voltage/filter settings of 40 kV/(1.0 mm Al) and 100 kV/(1.0 mm Al) are displayed on the left side



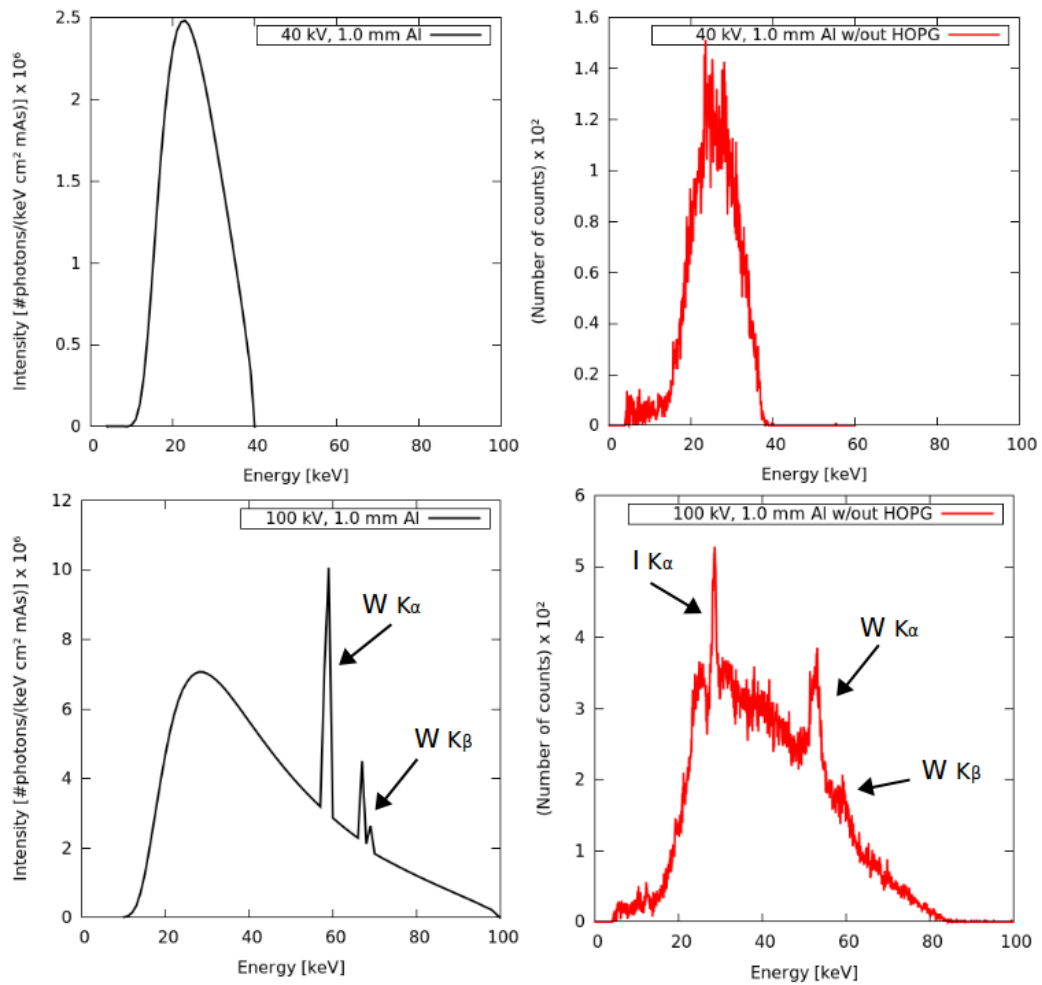


**Figure 7.3:** Left: Initial beam qualities with 40 kV/(1.0 mm Al) (top) and 100 kV/(1.0 mm Al) (bottom). Right: Respective XRF measurements. Note that the scale of the graphs of the initial beam intensity (left) and the graphs of the respective number of counts for the resulting XRF spectrum (right) differ by a factor of approximately 2.

and on the right side the respective XRF results without HOPG crystals. The resulting XRF signal for the 40 kV spectrum is not distinguishable from the continuously distributed background, whereas for the 100 kV spectrum the resulting XRF signal is clearly discriminable. Besides a decreased SNR the 40 kV spectrum is subject to stronger filtering by the 1.0 mm Al filter which leads to a decreased photon flux and therefore worse statistics in the resulting XRF spectrum.

		<i>w/o HOPG</i>	<i>w/ HOPG</i>
<i>Filter</i> [mm]	dose [Gy]	SNR	SNR
0.1 Al	8.12	$7.50 \pm 2.36$ ( $\pm 31.5\%$ )	$7.24 \pm 2.36$ ( $\pm 32.6\%$ )
0.5 Al	3.36	$7.87 \pm 2.53$ ( $\pm 32.1\%$ )	$7.45 \pm 2.67$ ( $\pm 35.8\%$ )
1.0 Al	2.12	$9.81 \pm 2.11$ ( $\pm 21.5\%$ )	$8.28 \pm 2.12$ ( $\pm 25.6\%$ )
2.0 Al	1.24	$8.73 \pm 2.12$ ( $\pm 24.3\%$ )	$8.19 \pm 2.22$ ( $\pm 27.1\%$ )
4.0 Al	0.65	$6.68 \pm 1.72$ ( $\pm 25.7\%$ )	$6.22 \pm 1.69$ ( $\pm 27.2\%$ )
4.0 Al + 0.2 Cu	0.23	$5.78 \pm 1.39$ ( $\pm 24.0\%$ )	$5.34 \pm 1.42$ ( $\pm 26.6\%$ )

**Table 7.2:** Results of XRF measurements without and with HOPG produced with different filters. A high voltage of  $U_A = 80$  kV was used for all measurements. The initial X-ray dose remains the same for measurements without and with implementing the HOPG crystal. The values for the SNRs are given according to table 7.1.

## Preliminary Conclusion

For optimised XRF experiments with iodine as contrast agent, the applied high voltage should satisfy the trade-off between a sufficient photon flux from the initial spectrum and a minimised amount of resulting background photons. Spectra with high voltages between 80 kV and 120 kV fulfil these requirements, but for the subsequent test series aiming to find a suitable filtration for the initial X-ray spectrum, the high voltage was chosen to be  $U_A = 80$  kV. Due to second order reflections off the 004-crystal-plane, the amount of spurious background photons in energy bins around 57.2 keV increases with increasing high voltage. Therefore it is reasonable to reduce these contributions by choosing the lowest convenient high voltage. This is also advantageous when implementing detectors with larger sensitive area, since with large angular coverage the amount of spurious background contributions is increased.

### 7.1.2 Influence of X-ray tube filtering

As described in section 6.1.1 a filter wheel installed in front of the exit window of the X-ray tube enables the generation of spectra with various beam qualities. In order to decide on a suitable filter that matches the chosen high voltage of  $U_A = 80$  kV for generating an optimal initial spectrum, various measurements have been performed: Similar as in the previous subsection, all experiments were conducted using the large anode spot, a  $90^\circ$  detector configuration, and the PMMA/mouse phantom filled with an iodine concentration of 5.0 mg/ml and 0.0 mg/ml (i.e. no iodine). The high voltage was kept fixed while various filters between 0.1 mm Al and 4.0 mm Al + 0.2 mm Cu were investigated. The recording time again was set to 120 seconds. Table 7.2 summarises the results for the applied dose and the SNR for each implemented filter. As expected, a stronger filtering notably decreases the intensity of the initial spectrum and consequently reduces the X-ray dose applied to the phantom.

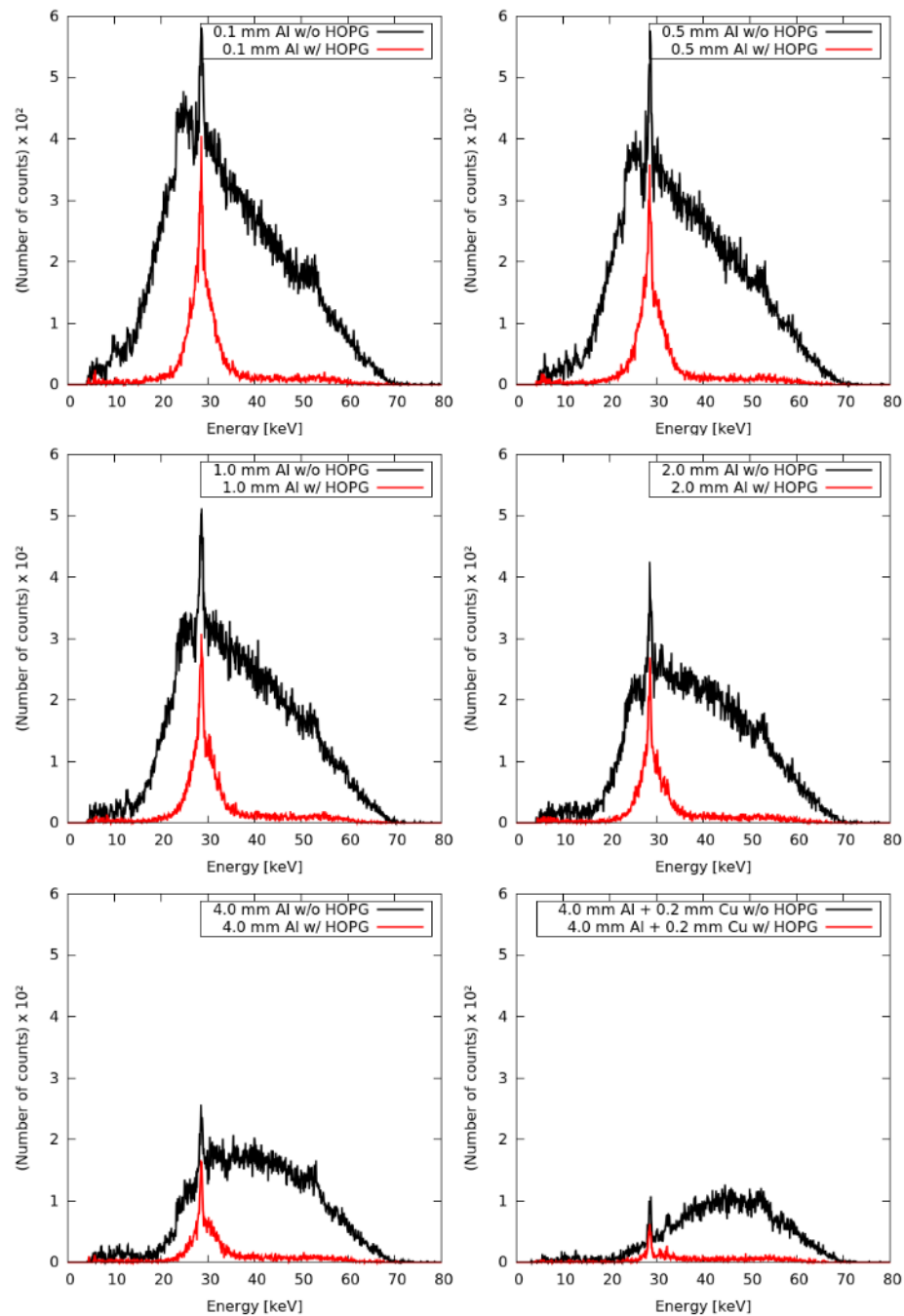


**Figure 7.4:** Collection of XRF spectra without/with HOPG recorded with different filter settings and a fixed high voltage of  $U_A = 80$  kV. Filters  $\geq 4.0$  mm Al significantly reduce the initial beam intensity resulting in XRF spectra with reduced counting statistics. Filters  $< 1.0$  mm Al yield XRF spectra with an increased amount of spurious counts below the EROI of 28.6 keV.

Figure 7.4 displays spectra recorded with filters from 0.1 mm Al up to 4.0 mm Al + 0.2 mm Cu. Each graph contains the measured spectra for experimental setups without and with HOPG crystals. All graphs nicely confirm the theoretical prediction, that the HOPG crystal reduces the intensity yield by approximately 50% in the EROI of 28.6 keV (and likewise by 5 - 10% in the region around 57.2 keV), and suppresses energy contributions from other energy bins. For filter configurations using less absorption capability than 4.0 mm Al, the measured spectra without HOPG exhibit non-negligible counts below the signal region, whereas filters equal or larger than 4.0 mm Al cut out these energy contributions. However, the latter filters significantly reduce the overall photon flux which is disadvantageous for the experimental setup which includes the HOPG crystal. In particular, the spectra recorded with the 4.0 mm Al + 0.2 mm Cu filter suffer from insufficient counting statistics, which can only be remedied by increasing the detection time. As a result, the 1.0 mm Al filter has been found to be the suitable candidate for the subsequent measurements, since it offers a reasonable trade-off between applied X-ray dose and counting statistic. It also achieves the largest SNR among all filter settings.

## Conclusion

As a result the initial spectrum displayed in figure 7.5 was chosen for all further XRF measurements. The results, however, will only be valid for this specific initial spectrum and the used industrial X-ray source.

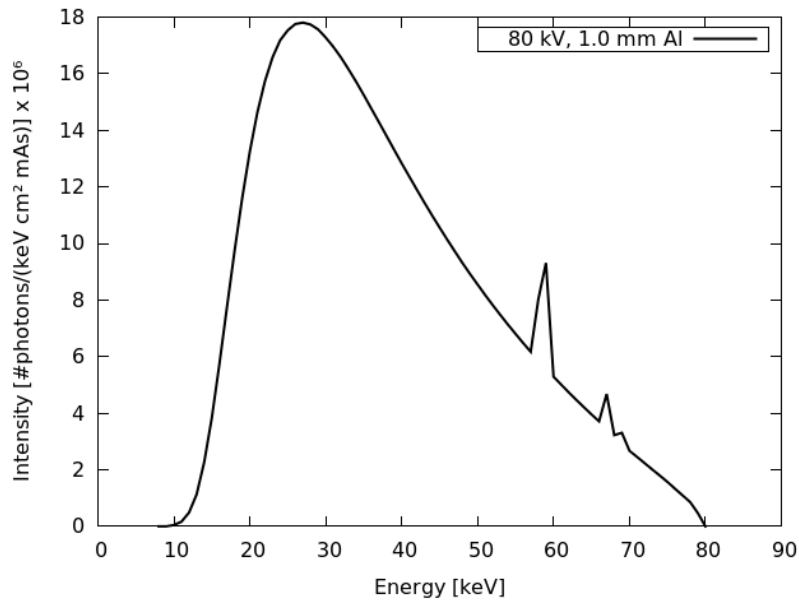


**Figure 7.5:** Final initial spectrum used for all subsequent XRF measurements of this work. Specifications:  $U_A$  80 kV,  $I = 37.5$  mA, 1 mm Al filter.

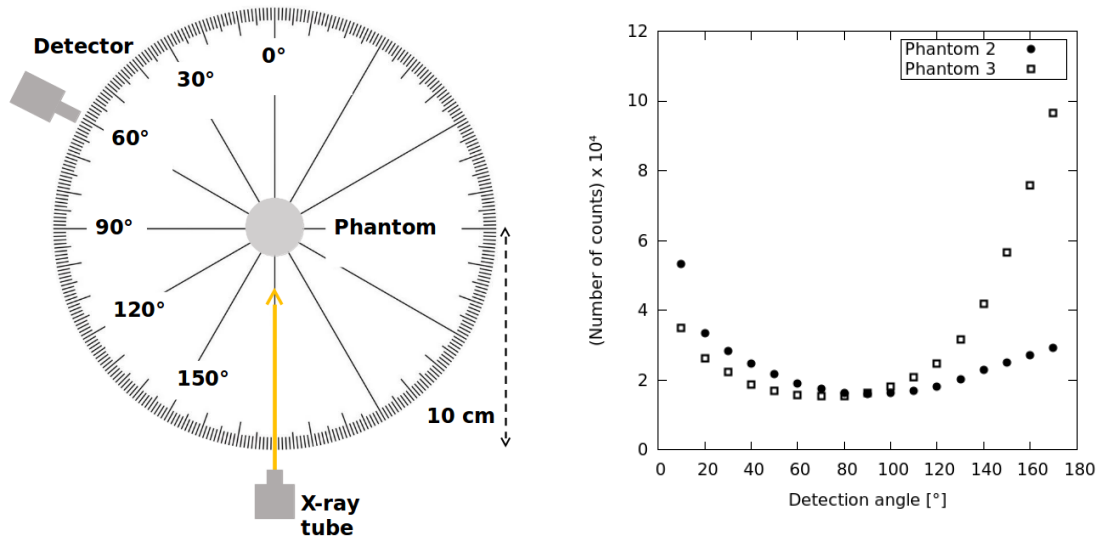


**Figure 7.6:** *Left: Detection scheme for investigating the anisotropic Compton background. Right: Number of counts per angular position of the detector relative to the X-ray source.*

### 7.1.3 Influence of angular detector configuration

XRF measurements with polychromatic X-ray sources are impaired by spurious background counts, which however can be reduced by a suitable angular detector configuration such as the relative angular position between the X-ray source and the detector as shown in figure 7.6 (left). Moreover, the total attenuation path, i.e. the phantom size, additionally alters the quality of the emitted XRF signal for each detection angle.

In [31] a simplified mathematical model was introduced which reflects the behaviour of the anisotropic background distribution. The underlying assumption was that a minimal difference between the mean photon energy of the initial spectrum and the K-edge of the contrast agent predominantly produces first order Compton photons. This thesis does not aim to validate this model and does not intensify the investigations related to the background distribution within XRF spectra. For the sake of optimised XRF measurements it is however necessary to find the optimal relative angular detector position for the initial spectrum found in sections 7.1.1 and 7.1.2 emitted from the PMMA/mouse phantom (phantom 2).

In order to study the dependency of phantom size and detection angle a test series was performed irradiating the PMMA/mouse phantom (phantom 2; 3 cm diameter) and phantom 3 (10 cm diameter) and recording the emitted background photons from angles between 10° and 170°. The small Eppendorf test tube (phantom 1) was not used for this study since it only comprises a small volume filled with the contrast agent. It lacks an absorbing layer which would show its influence on the background distribution. Phantom 2 was used without contrast agent. For all measurements the initial spectrum derived above ( $U_A = 80$  kV,  $I = 37.5$  mA, 1.0 mm Al filter) was used. The test series was conducted without implementing the HOPG crystal since its implementation in varying angular configurations is very challenging and consequently subject to systematic errors. As opposed to the measurements in the subsections above, the measurement time was set to 60 seconds. This is reasonable since in the setup

	<i>w/o HOPG</i>		<i>w/ HOPG</i>	
<b>I [mg/ml] [kV]</b>	<b>SNR</b>		<b>SNR</b>	
<b>0.6</b>	2.12 ± 0.75	(± 35.4 %)	2.01 ± 0.69	(± 34.3 %)
<b>1.2</b>	2.59 ± 0.76	(± 29.3 %)	2.28 ± 0.76	(± 33.3 %)
<b>2.3</b>	4.55 ± 1.16	(± 25.5 %)	4.41 ± 1.41	(± 32.0 %)
<b>5.0</b>	9.81 ± 2.11	(± 21.5 %)	8.28 ± 2.12	(± 25.6 %)

**Table 7.3:** Results of XRF measurements without and with HOPG produced with the PMMA/mouse phantom (phantom 2) filled with various iodine concentrations. The values for the SNRs are given according to table 7.1.

here, no additional collimators are used, which considerably filter the XRF spectrum. In contrast, the flux here is large enough so that counting statistics are not impaired. Figure 7.6 (right) shows the results for the measured photon flux emitted by the two phantoms depending on the detection angles. Error bars were not included, since the errors are situated within the symbols for the photon counts. For phantom 3, the number of background counts increases with increasing detection angle (backward scatter), which is in accordance with the findings of [31]. In contrast, the results for phantom 2 reveal that a broad range of angular detection configurations is suitable for an optimal XRF signal yield.

This result shows that a 90° angular detector configuration, as implemented in previous measurements, is suitable (lowest amount of Compton scatter) for all further investigations with the initial spectrum derived in the previous section. Moreover, the findings show that angular detector positions between 80° and 110° do not significantly increase the amount of scatter for phantom 2. This implies that detectors with larger sensitive areas could be implemented without deteriorating the quality of the results. In contrast, the XRF signal yield would be improved.

## 7.2 Measurements of various iodine concentrations

With the derived initial spectrum ( $U_A = 80$  kV,  $I = 37.5$  mA, 1.0 mm Al filter) various XRF measurement were performed using the PMMA/mouse phantom (phantom 2) and the simple Eppendorf test tube (phantom 1). Each phantom underwent a measurement sequence with an experimental setup omitting the HOPG crystal and a setup where the crystal was included. In total four measurement series were performed. The first subsection deals with the PMMA/mouse phantom (phantom 2) and the second subsection will summarise the results implementing the simple Eppendorf test tube (phantom 1). The resulting XRF spectra form the basis for the feasibility tests of the Monte Carlo code presented in part III, *Monte Carlo Simulation GEANT4*, of this work.

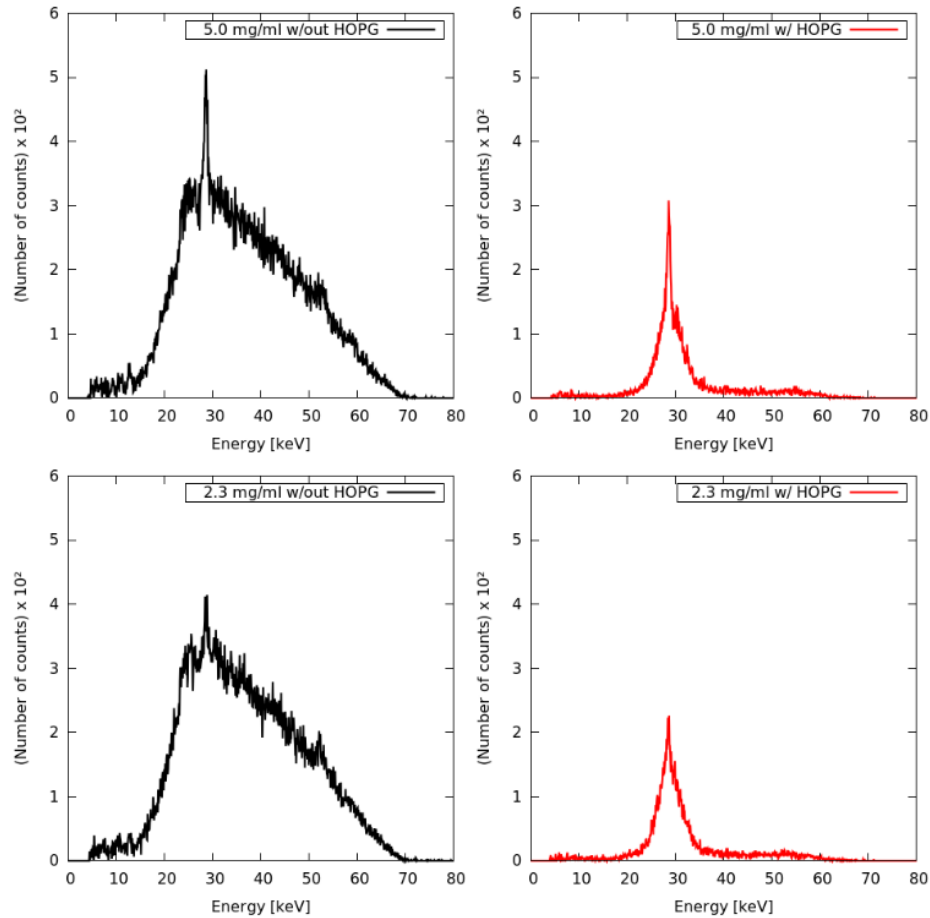


**Figure 7.7:** XRF spectra emitted by the PMMA/mouse phantom without (left) and with (right) HOPG crystal. The HOPG isolates the energy region around the  $K_{\alpha}$  signal of iodine and suppresses other energy regions.

### 7.2.1 PMMA/mouse phantom (phantom 2)

For the XRF measurements the PMMA/mouse phantom was filled with iodine concentrations of 0.6 mg/ml, 1.2 mg/ml, 2.3 mg/ml and 5.0 mg/ml and one measurement was performed without iodine. Figure 7.7 shows an XRF spectrum performed with phantom 2 using an iodine concentration of 5.0 mg/ml (top) and 2.3 mg/ml (bottom), left without the HOPG and right including the crystal. The results nicely confirm the 50% reduction of counts due to the HOPG crystal and the suppression of other energy bins. The energy range of the second order 004-plane reflection in the energy area around 57.2 keV shows a minimal increase of photon counts, but is nevertheless very well reduced.

Table 7.3 summarises the results of the XRF spectra for each iodine concentration, displaying the SNR for both experimental setups including and omitting the HOPG crystal. Figure 7.8 visualises these findings. As expected, the SNR shows a linear increase with the iodine concentration. A contrast agent concentration of 2.3 mg/ml or lower yields an SNR that does not fulfil the Rose criterion. Only the SNR derived with a 5.0 mg/ml iodine concentration lies clearly above this threshold. Recordings

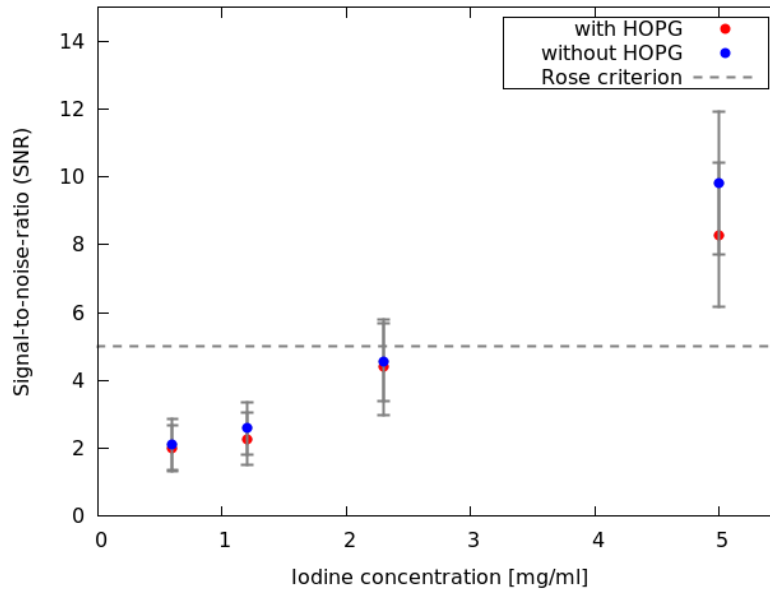


**Figure 7.8:** SNRs of recorded XRF spectra (with/without HOPG crystal) emitted from the PMMA/mouse phantom, applying various iodine concentrations between 0.6 mg/ml and 5.0 mg/ml.

with a considerably increased measuring time and dose would reduce the statistical fluctuations and improve the values for the SNRs.

### 7.2.2 Eppendorf phantom (phantom 1)

This subsection deals with XRF measurements recorded using the Eppendorf test tube phantom. Due to its lack of an absorbing PMMA layer, it is expected that even lower iodine concentrations than the ones used for phantom 2 will fulfil the Rose criterion. Measurements were performed without iodine and with contrast agent concentrations of 0.15 mg/ml, 0.3 mg/ml, 0.6 mg/ml, 1.2 mg/ml, 2.3 mg/ml and 5.0 mg/ml. Figure 7.9 shows the resulting XRF spectra recorded with iodine concentrations of 5.0 mg/ml (top) and 2.3 mg/ml (bottom), left without the HOPG and right including the crystal. The results clearly show the influence of phantom size: The absolute values of the XRF signals and resulting SNRs are notably larger than for the PMMA/mouse phantom. Also the number of background counts is considerably reduced compared to the spectra performed with the PMMA/mouse phantom (compare figure 7.7). Even the signal of the  $K_{\beta}$  emission line is discriminable for the spectra without HOPG implementation and the 5.0 mg/ml spectrum including the crystal.



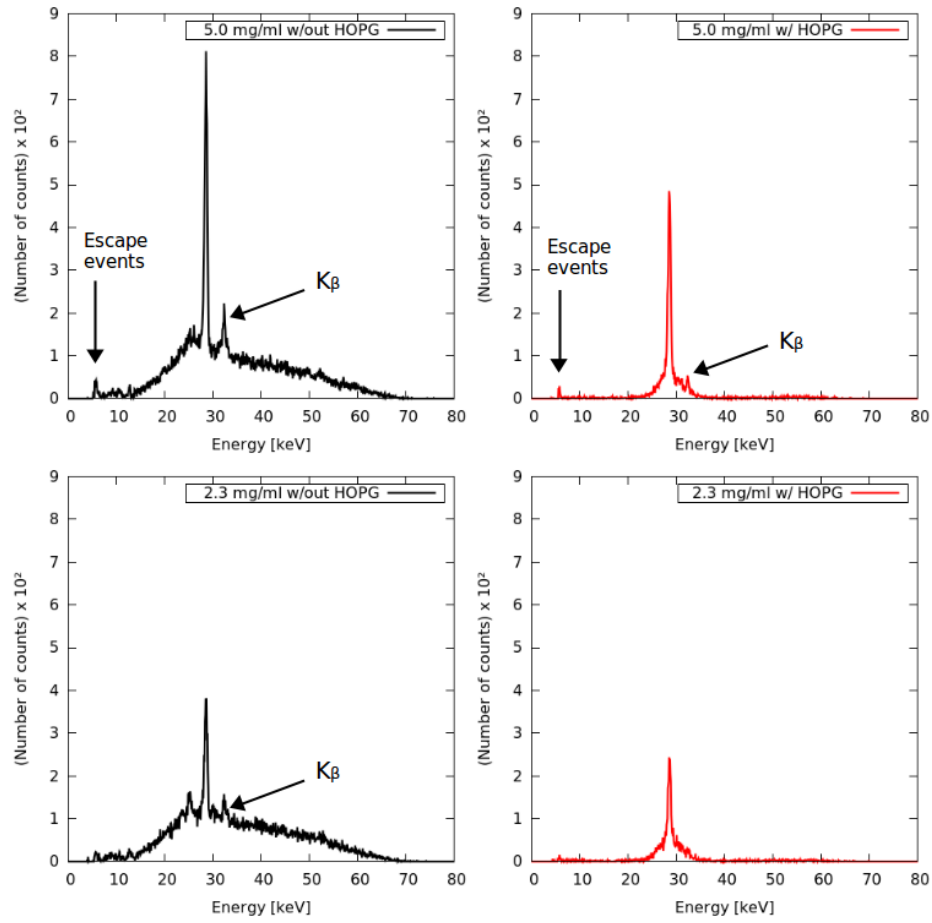


**Figure 7.9:** XRF spectra emitted by the Eppendorf test tube without (left) and with (right) the HOPG crystal. The amount of background photons is considerably reduced compared to the spectra emitted by the PMMA/mouse phantom. The  $K_{\beta}$  signature is clearly distinguishable from the background for an implementation without HOPG crystal, but is reduced in the HOPG results. In the results using an iodine concentration of 5.0 mg/ml there is an artefact due to escape events at  $\approx 5$  keV.

	<i>w/o HOPG</i>		<i>w/ HOPG</i>	
<b>I [mg/ml] [kV]</b>	<b>SNR</b>		<b>SNR</b>	
<b>0.15</b>	3.37 ± 1.03	(± 30.6 %)	1.55 ± 0.83	(± 53.5 %)
<b>0.3</b>	1.59 ± 0.61	(± 38.4 %)	2.67 ± 1.17	(± 43.8 %)
<b>0.6</b>	6.03 ± 1.56	(± 25.9 %)	5.26 ± 1.69	(± 32.1 %)
<b>1.2</b>	8.84 ± 2.07	(± 23.4 %)	8.21 ± 2.21	(± 26.9 %)
<b>2.3</b>	13.95 ± 2.94	(± 21.1 %)	12.13 ± 2.70	(± 22.3 %)
<b>5.0</b>	24.66 ± 4.63	(± 18.8 %)	19.56 ± 3.88	(± 19.8 %)

**Table 7.4:** Results of XRF measurements without and with HOPG produced with the Eppendorf test tube phantom filled with various iodine concentrations. The values for the SNRs are given according to table 7.1.

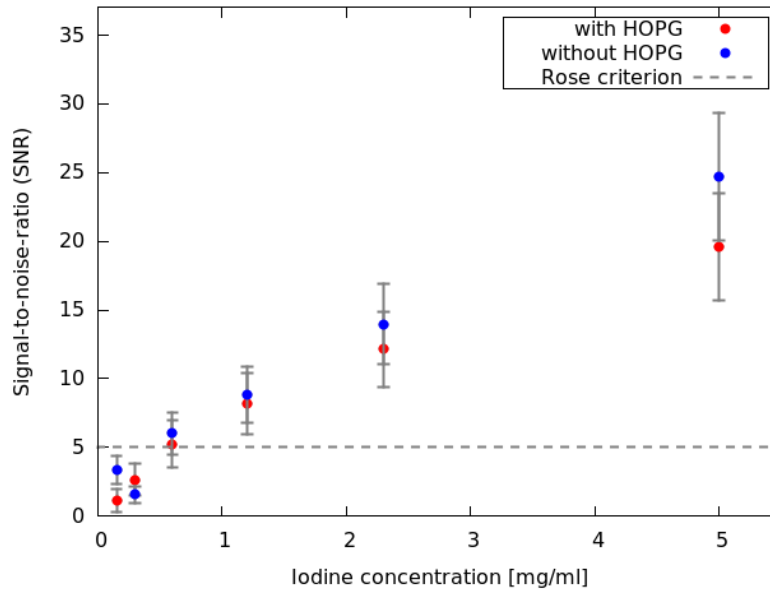


**Figure 7.10:** SNR of recorded spectra emitted from the Eppendorf test tube phantom, applying various iodine concentrations between 0.15 mg/ml and 5.0 mg/ml.

The signature at about 5 keV for the 5.0 mg/ml measurements is an artefact due to escape events which could not entirely be removed by the stripping algorithm. Figure 7.10 shows the linear increase with iodine concentration of the SNRs for both experimental setups (the values are summarised in table 7.4). Even an iodine concentration of 0.6 mg/ml leads to an SNR of  $6.03 \pm 1.56$  (without HOPG) and  $5.26 \pm 1.69$  (with HOPG), thus fulfilling the Rose criterion. The measurements with lower iodine concentrations, i.e. with 0.15 mg/ml and 0.3 mg/ml, do not show the linear increase when measured without HOPG. It is possible that the iodine concentration in this configuration is too low, in order to be discriminable from the scatter background.

## 7.3 Air kerma measurements with ionisation chambers

In order to obtain a value for the dose applied to the used phantom with the chosen spectrum ( $U_A = 80$  kV,  $I = 37.5$  mA, 1.0 mm Al filter), air kerma measurements were performed with two different ionisation chambers according to the measurement scheme described in subsection 6.2.1. The corresponding calibrating factors used for the chambers are summarised in table 7.5 and the values for each single charge measurement  $Q_i$  are listed in table 7.6. Also included are the corresponding values  $K_i$  for the measured air kerma, which are calculated according to the relation 6.1 explained in subsection 6.2.1:

$$K_i = (Q_i - Q_a) \times N_k \times K_Q \times K_\rho \times K_E. \quad (7.1)$$

The average absorbed dose measured for 60 seconds with the small ionisation chamber Q16, yields  $1.06 \pm 0.14$  Gy. For the larger ionisation chamber Q30 the absorbed dose calculates to  $1.03 \pm 0.14$  Gy. The uncertainty of  $\pm 0.14$  Gy derives from the error for  $K_Q$ ,  $T$  and  $p$ , and an overall uncertainty of 1 % in the final results as stated by the manufacturer. The differences in results using the different sizes of ionisation chamber are small considering the uncertainties. However, the differences potentially arise due to three different reasons: i) The calibration factors taken from the calibration document are determined for specific beam qualities, i.e. for combinations of source and filter, and peak kilo voltages not used in this work. Therefore, for this work, an approximate value of  $K_Q$  is used. ii) As explained in subsection 6.1.1, the large anode spot distributes the amount of emitted photons unevenly on its surface. Consequently, there is a probability that the small ionisation chamber was positioned such that it was primarily irradiated by a large photon flux rate, whereas the large chamber additionally comprised areas of reduced photon fluxes. iii) A third cause for the discrepancy in the results could arise due to the Heel effect, which is a variation of the emitted X-ray intensity depending on the direction of emission along the axis between the anode and cathode. The anode geometry influences the photon intensity such that photons emitted perpendicular to the anode-cathode axis are usually less intense than those directed towards the cathode. The reason for this effect is absorption of X-rays within the anode material before being emitted. As a consequence, the small ionisation chamber is likely to predominantly collect X-ray photons of higher intensity compared to the larger ionisation chamber, whereas the larger ionisation chamber also collects photons of larger divergence from the anode-cathode axis, which are known to be less intense. Therefore, the air kerma measured by the large ionisation chamber is smaller

	$N_k$ [ $\frac{\mu\text{Gy}}{\text{C}}$ ]	$K_Q$	$K_\rho$	$K_E$	$Q_a$ [nC]	$T$ [°C]	$p$ [hPa]
<b>Q 16</b>	27.52	$0.947 \pm 0.025$	1.054	1.0	0.0	$22.75 \pm 0.05$	$970.30 \pm 0.05$
<b>Q 30</b>	931.90	$0.979 \pm 0.025$	1.054	1.0	-0.15	$22.85 \pm 0.05$	$970.25 \pm 0.05$

**Table 7.5:** Calibration factors for both ionisation chambers used for calculating the air kerma [Gy].

# measurements	Q16: $Q_i$ [nC]	$K_i$ [Gy]	Q30: $Q_i$ [nC]	$K_i$ [Gy]
1	38.64	$1.06 \pm 0.14$	1075.0	$1.03 \pm 0.14$
2	38.64	$1.06 \pm 0.14$	1075.0	$1.03 \pm 0.14$
3	38.65	$1.06 \pm 0.14$	1075.0	$1.03 \pm 0.14$
4	38.66	$1.06 \pm 0.14$	1075.0	$1.03 \pm 0.14$
5	38.67	$1.06 \pm 0.14$	1076.0	$1.03 \pm 0.14$
6	38.67	$1.06 \pm 0.14$	1076.0	$1.03 \pm 0.14$
7	38.68	$1.06 \pm 0.14$	1076.0	$1.03 \pm 0.14$
8	38.69	$1.06 \pm 0.14$	1076.0	$1.03 \pm 0.14$
9	38.69	$1.06 \pm 0.14$	1076.0	$1.03 \pm 0.14$
10	38.70	$1.06 \pm 0.14$	1076.0	$1.03 \pm 0.14$
11	38.70	$1.06 \pm 0.14$	1077.0	$1.03 \pm 0.14$
<b>average</b>	<b>38.67</b>	<b><math>1.06 \pm 0.14</math></b>	<b>1075.73</b>	<b><math>1.03 \pm 0.14</math></b>

**Table 7.6:** Results of the dose measurements with the small (Q16,  $0.6 \text{ cm}^3$ ) and the large (Q30,  $30 \text{ cm}^3$ ) ionisation chamber.  $Q_i$  [nC] denominates the charge of each single charge measurement and  $K_i$  is the calculated air kerma [Gy] for each single measurement. The final row averages over the single measurements. The final result is  $1.06 \pm 0.14 \text{ Gy}$  for Q16 and  $1.03 \pm 0.14 \text{ Gy}$  for Q30.

than the dose measured by the small ionisation chamber. If the Heel effect is mainly responsible for the deviation of the measured dose, then the dose measured by the small ionisation chamber ( $1.06 \pm 0.14 \text{ Gy}$ ) should be chosen since it displays the dose applied to a small phantom more accurately. Another reason in favour of the value obtained with the small ionisation chamber is the irradiated solid angle, which for the XRF measurements is even smaller than that for the air kerma measurement with the small ionisation chamber. Also, in the context of radiation protection it is advisable to assume a more conservative value for the applied dose, i.e. a dose of  $1.06 \pm 0.14 \text{ Gy}$ . This yields an absorbed dose rate of roughly  $17.7 \pm 0.14 \text{ mGy/s}$ .

With this result, SpekCalc (cp. section 6.2.2) can be gauged such that it meets the characteristics of the used X-ray tube when calculating the air kerma. The dose rate modifying factor  $N_f$  thus derives to a value of 2.1.

## Part III

# Monte Carlo simulation GEANT4



In order to further investigate the potential of X-ray fluorescence together with an energy-selective HOPG crystal, part III makes use of the Monte Carlo code **GEANT4**. Chapter 8 provides a profound introduction to the functionality of the **GEANT4** toolkit and in chapter 9 the methods for simulating X-ray fluorescence and HOPG reflection will be explained. In order to assure the correct functionality of the code, chapter 10 deals with the exact computational reproduction of the experimental results generated in part II. This part concludes with a thorough investigation of the potential of large area detectors with increased intrinsic detector resolution and large bin sizes, together with various HOPG/HAPG crystal mosaicities (chapter 11).





## 8. Introduction to the GEANT4 toolkit

GEANT4<sup>1</sup> is a software toolkit based on Monte Carlo methods, which was developed to accurately simulate the passage of particles through matter [83–85]. It is the result of a worldwide collaboration initiated by CERN<sup>2</sup> comprising physicists and software engineers from various cooperating institutes, universities and high energy experiments. The software package is freely available and can be downloaded from the GEANT4 web-page<sup>3</sup>.

The project was initiated with the aim to incorporate advanced software-engineering techniques into the existing GEANT3 code [86], the predecessor written in Fortran95 [87]. Such as all other procedure-based Monte Carlo codes GEANT3 suffered from an unmanageable complexity and interdependency when being extended by new and alternative physics models. In order to resolve this difficulty and to maintain transparency and flexibility within a continuously growing large scale software project, GEANT4 is written in C++ [88]. It therefore exploits object-oriented design philosophy and follows an iterative-incremental software development process [89] that permits refinements and extensions to the toolkit while avoiding drastic modifications to the existing code. All simulations in this thesis were performed using GEANT4 version 10.00.

### 8.1 The Monte Carlo method in GEANT4

For very detailed simulation settings, tracking individual particles can significantly reduce the CPU time, since a particle in flight is subject to many competing processes. Moreover, the particle may proceed through various geometries of different materials, sizes and shapes before interacting or decaying. In GEANT4 a particle is moved forward in **steps** and it is crucial to find an efficient way of limiting the **step** size, in order to maintain a reasonable computing time. For that reason GEANT4 applies Monte Carlo methods at each **step** by randomly sampling interaction probability distributions given by cross sections from theoretical models or experimental data that are tabulated during initialisation [83, 90].

The interaction length or mean free path  $\xi$  of a particle is

---

<sup>1</sup>acronym for GEometry ANd Tracking

<sup>2</sup>*Conseil Européen pour la Recherche Nucléaire* [European Council for Nuclear Research]

<sup>3</sup><http://geant4.web.cern.ch/geant4/> (retrieved 1 May 2019)

$$\xi = \rho \left[ \sum_i \frac{x_i \sigma_i}{m_i} \right]^{-1}, \quad (8.1)$$

where  $\rho$  is the density of the current material,  $\sigma_i$  the cross-section of isotope  $i$ , mass  $m_i$  of the isotope and fraction by mass  $x_i$ . The total number of mean free paths  $n_\xi$  that the particle can traverse before the next interaction occurs is

$$n_\xi = \int_0^l \frac{dl}{\xi(l)}. \quad (8.2)$$

Since the probability distribution of  $n_\xi$  is a simple exponential and hence independent of material and energy, the particle in flight has a probability of surviving a distance  $l$  without interacting given by

$$P(l) = 1 - e^{-n_\xi}. \quad (8.3)$$

Consequently  $n_\xi$  can be randomly sampled at the beginning of the trajectory by setting

$$n_\xi = -\ln(\zeta), \quad (8.4)$$

where  $\zeta$  is a random number uniformly distributed in the range  $(0,1]$ . With this procedure the distance  $s(l) = n_\xi \cdot \xi(l)$  to the next point of interaction in the current material is determined.

All possible processes applicable to the particle at this current **step** propose a **step** length  $l$  according to the Monte Carlo technique given above, each process using a different random number  $\zeta$ . The process suggesting the shortest distance to the next point of interaction is chosen and determines the reaction acting on the particle at the current **step**. Interaction or decay processes annihilate the particle and create secondary particles, which are then tracked according to the same scheme.

An additional limit to the **step** length is imposed such that the **step** is confined to the current object in which the particle is moving, forcing the **step** to end at a geometrical border. Further information concerning the processing of particle transport can be found in the *GEANT4 Physics Reference Manual* [90].

## 8.2 Structure, design and architecture of GEANT4

GEANT4 was intended to satisfy the software needs of modern experiments which inspired its modular and flexible programme design. Its individual components can be utilised separately or in combination. The key elements of the tracking of particles in matter are described below.

### 8.2.1 Geometry and materials

With the toolkit it is possible to build an environment with an arbitrary number of components with various shapes and materials and the ability to integrate voxel models. Repetitive structures can be multiplied by parameterisation, thus saving CPU time. Moreover the tracking efficiency is increased since the geometrical setup follows a hierarchical principle comparable to that of a Russian doll (Matryoshka): The largest geometric domain, defined as the *mother volume*, contains smaller volumes which are again hosts for even smaller geometrical entities and so on.

The construction of materials in GEANT4 reflects the logical organisation in nature where materials are built from elements and elements are constructed from isotopes. Isotopes reflect the intrinsic properties of atoms such as atomic number, number of nucleons and mass per mole etc. From that, elements can be built which encompass the number of isotopes, effective atomic number, effective number of nucleons, effective mass per mole, shell energy, and other quantities such as the cross section per atom. The sum of different elements in individual materials reflect the macroscopic properties of matter like density, state, temperature, pressure, and dimensions such as radiation length and mean free path.

Alternatively materials can be built using the internal GEANT4 database which is based on the NIST<sup>4</sup> [92] database of isotope and element compounds.

### 8.2.2 Particles and their interaction with matter

As GEANT4 was originally designed for high energy physics a large amount of particle types are implemented that can be derived from internal or external sources. Various physical processes and models for photons, electrons, muons and hadrons can be defined. Practically all simulation applications use the GEANT4 electromagnetic physics models and processes described in [83, 93, 94]. However, the user needs to decide which physics model best suits the simulation task. Since this work deals with imaging using X-rays, the relevant physics processes are Rayleigh scattering, Compton scattering, and the Photoelectric effect (cp. chapter 2). Consequently the low energy **Livermore** model [95] was initialised, which employs a set of publicly distributed data libraries [96–98] in order to determine cross-sections and to sample final state characteristics. This data set is included in the **G4LEDATA** set in a reformatted form and can be downloaded from the CERN website<sup>5</sup> and compiled with GEANT4. The advantage over the implemented *standard* electromagnetic physics model [94] is that its validity of particle interactions extends to lower energy ranges. It also comprises an atomic de-excitation module including the emission of fluorescence and Auger electrons.

---

<sup>4</sup>National Institute of Standards and Technology, [www.nist.gov](http://www.nist.gov)

<sup>5</sup><http://geant4.web.cern.ch/geant4/> (retrieved 1 May 2019)

### 8.2.3 Tracking and event generation

Following particle tracks is a fundamental feature in GEANT4 and is carried out according to the Monte Carlo approach described in section 8.1. At the end of each **step** a particle can interact with its surroundings and the corresponding physical process is invoked. In the context of X-ray imaging these are primarily Rayleigh scattering, Compton scattering, and the Photoelectric effect. Each primary particle generated at initialisation is considered to be an **event**. At an interaction point this primary particle is discarded and secondary particles are created and hence new **events** are generated. For the generation of secondaries GEANT4 implements a *range cut off* instead of an *energy cut off*, as used in many other comparable codes. That means, that if the expected range of a secondary particle in the material is less than the cut value, no secondary particle will be produced.

### 8.2.4 Detector - hits and digits

In GEANT4 a detector is built according to the concepts of a *Physical Volume* and a *Logical Volume*. The former refers to the geometrical representation of the detector such as the spatial positioning of all detector components and their relation to each other, whereas the latter can be used to coordinate the information linked to the element properties like sensitivity, electronics and response. *Physical Volumes* are constructed in the same manner as all other geometries within the simulation setup as described earlier in subsection 8.2.1. The *Logical Volume* enriches this simple geometrical representation with user defined intrinsic parameters and manages the information related to visualisation characteristics and tracking properties.

When a particle track interacts with the sensitive area of a detector, all the information contained in a **step** is recorded in a **Hit**. This **Hit** stores the **step** information about position, time, momentum, energy, energy deposition and geometrical attributes. An accumulation of **Hits** is collected in a **HitsCollection** which is imparted to **Digi**, the digitisation class, which transfers all **Hit** information to a readout scheme and the graphical system for visualisation.

### 8.2.5 User interface and visualisation

The visualisation design of GEANT4 was built around a complex interface that supports various graphics systems with flexible handling of graphics libraries. This work makes use of OpenGL<sup>6</sup> [99] and Qt<sup>7</sup> [100], which both require additional libraries that are partly pre-installed on various Linux systems and are freely available on most operating systems. As shown in figure 8.1 (simplified Qt example representation of simulation setup) all parts of the simulation setup can be visualised, including geometries, particle trajectories, and particle **Hits** in the detector element. The advantage of using Qt is that it offers the possibility to create a movie, thus providing control of the complete simulation flow. OpenGL enables zoom, rotation and translation and each **run** can be

---

<sup>6</sup>[www.opengl.org](http://www.opengl.org) (retrieved 1 May 2019)

<sup>7</sup>[www.qt.io](http://www.qt.io) (retrieved 1 May 2019)

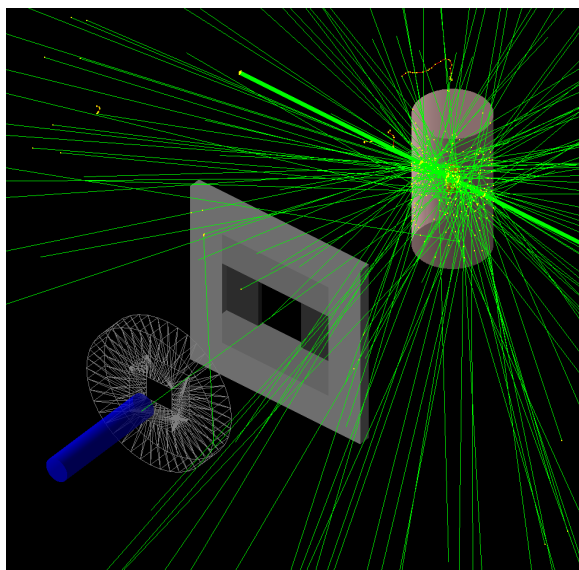


**Figure 8.1:** *Simplified scheme of the simulated XRF imaging setup visualised with Qt: The PMMA/mouse phantom (phantom 2) is irradiated by an X-ray beam (green) originating in the top part of this image. The grey square is the slit collimator and the blue cylinder represents the detector. The grey wired cylinder in front of the detector represents an additional lead collimator, shielding the detector from scatter. Every step is visualised as a yellow dot. Secondary X-rays isotropically emitted by the phantom are green.*

initiated and viewed from the user interface. This feature enables the verification of the correct implementation of all elements of the setup and subsequent elimination of errors such as geometrical overlaps and deviating particle trajectories.

### 8.2.6 Data analysis

GEANT4 provides a variety of storage and analysis systems for the production of histograms and statistical reports of the data provided by Digi. A full list of tools and output formats can be found in [91]. Data generated in this work was stored in ASCII format and further processed with own routines written in C++, which are discussed in more detail in section 9.3.

## 8.3 (Pseudo) random number generator (PRNG)

The performance of the Monte Carlo approach described in section 8.1 strongly depends on the quality of the random number sequences used to calculate the probability distribution functions. In practice, pseudo random number generators (PRNG)<sup>8</sup> [101] are sufficiently fast and deliver sufficient randomness for applications such as Monte Carlo simulations. The random number sequence generated by a PRNG is controlled by the so-called *seed*, which is a fixed starting value that initialises the number sequence. From the seed all pseudo random numbers are derived according to a deter-

<sup>8</sup>also known as deterministic random bit generator (DRBG)

ministic and iterative sequence, thus also allowing reproducibility by using the same initial seed again. Besides having good random properties a central requirement of an adequate PRNG algorithm is the possibility to manage several subsequences in order to allow for parallelisation on multiple processors. These features are included in the `HEPJamesRandom` algorithm [102] used in this work. The code is a component of the `HEPRandom` module which is incorporated in the `CLHEP`<sup>9</sup> library [103] included in `GEANT4` since version 9.5.

## 8.4 Parallelisation

Monte Carlo simulations with a large number of `events` can result in very large computing times. However, since the `events` are independent from each other, the computation time can be significantly reduced by distributing all primary `events` in parallel `runs` with different initial seeds. For this work, parallelisation was implemented using the Message Passing Interface (MPI) [104] with the `OpenMPI`<sup>10</sup> [105] library. Using the `GEANT4` MPI run manager the simulation was split up into several `runs` and allocated to several clusters.

---

<sup>9</sup><http://cern.ch/clhep> (retrieved 1 May 2019)

<sup>10</sup>[www.open-mpi.org](http://www.open-mpi.org) (retrieved 1 May 2019)

## 9. Methods for simulating X-ray fluorescence and HOPG reflection

### 9.1 Implementation of the X-ray source

Since the experimental investigation of this work was performed using an industrial X-ray source (YXLON MG160), it is necessary to supply the simulation code with realistic polychromatic X-ray spectra and an accurate beam geometry. All spectra were generated with SpekCalc [74] (cp. subsection 6.2.2) using the same parameters used in the experiments ( $U_A = 80$  kV,  $I = 37.5$  mA, 1.0 mm Al filter and an irradiation time of 120 seconds) and stored in ASCII format with an energy bin size of 1 keV. The spectrum files were read-in by the code and the rate of emission of photons in each energy bin was used to calculate a probability density function of photon energies. For the simulation the X-ray energies were randomly drawn from these probability density functions. According to the experimental setup (chapter 6) the diameter of the beam was set to 1 mm, but was adjustable to different sizes and shapes.

### 9.2 Implementation of the detector

For the simulation of XRF photons it is necessary to integrate routines for energy resolved detection schemes. All relevant geometrical attributes of the detector were built according to the specifications given by the manufacturer (cp. subsection 6.1.4): The detector sensitive CdTe area had dimensions of 3.4 mm in diameter and 1 mm in thickness. A beryllium window with a 4 mm diameter and 0.1 mm thickness was placed at a distance of 2 mm from the detector area. The energy bin was set to approximately 86 eV.

GEANT4 version 10.00 does not provide the possibility to simulate crystal materials with intrinsic mosaic structure and the (quasi-)monochromatising effect on radiation. Therefore the resulting data generated by the GEANT4 simulations had to be further processed in order to account for the energy-filtering properties of the HOPG. As a consequence, the detector simulated with the toolkit was assumed to be ideal concerning detection efficiency and energy deposition. All features offered by GEANT4 to construct a detector as realistic as possible, including escape events, hole tailing, charge trapping, electronic noise and Fano broadening, had to be neglected. All detector effects relevant for measurements within this energy range had to be simulated subsequently with separate routines and will be explained as follows.

## 9.3 Data processing and analysis

In order to scrutinise the effect of HOPG crystals on XRF imaging, it is necessary to compare the experimental results using the crystal with the results generated without crystal. Moreover, the findings of the experiment need to be comparable with the results obtained via the GEANT4 simulation. Two steps are necessary to meaningfully compare the results of the simulations to the results of the experimental investigations. First the effects of the energy-selective HOPG crystal have to be included in the simulation output. The second step is to account for the detector effects that lead to broadening of the fluorescence peaks (intrinsic energy resolution). In the simulations for the case not using a HOPG crystal, the first step can be neglected.

### 9.3.1 HOPG crystal reflection curve – XOP v2.4

Since the calculation of the reflection and transmission profile of HOPG crystals is very complex, this work makes use of the XOP<sup>1</sup> programme [106], which is an open source front-end interface of several codes used for the calculation of radiation characteristics of X-ray sources and their propagation through matter. The programme version used in this work (XOP v2.4) is based on IDL version 8.1 [107] and is hence available for all IDL-supported operating systems such as Windows, Unix, Linux and macOS. It is of great interest for the synchrotron radiation community due to its synergy of codes modelling various X-ray sources (synchrotron radiation such as undulators and wigglers, as well as common X-ray tubes) and codes computing the index of refraction and attenuation coefficients of optical elements (mirrors, filters, crystals, multilayers, etc.) using user-selectable databases.

For the calculation of the reflection and transmission profiles (reflection curves) of the HOPG 002 and 004 crystal planes, XOP provides the XCRYSTAL code. It is based on the theory of diffraction developed by Zachariasen [37] in order to calculate the diffraction profiles of perfect and mosaic crystals in Bragg and Laue geometries. It is possible to either compute angular scans based on a given photon energy, or energy scans based on a fixed incident beam angle. This work uses the latter option.

For determining the appropriate incident beam angle for the maximal reflection of the photons of the iodine  $K_{\alpha}$  fluorescence line, a complementary programme called X0h<sup>2</sup> [108, 109] is used. For a given energy it provides the Miller indices range, the Bragg angles range, the minimum intensity of Bragg reflection and the range of angles of the respective plane. The left side of figure 9.1 shows the search form of X0h and the right side displays the results for the iodine  $K_{\alpha_2}$  fluorescence line (28.6 keV). The result sheet provides the Bragg angles for every crystal plane for a photon energy of 28.6 keV, which can be implemented in XOP in order to calculate the crystal reflection curve.

---

<sup>1</sup>X-ray Oriented Programs

<sup>2</sup>X0h was built to calculate the crystal susceptibilities  $\chi_0$  and  $\chi_h$  for X-ray scattering and Bragg diffraction



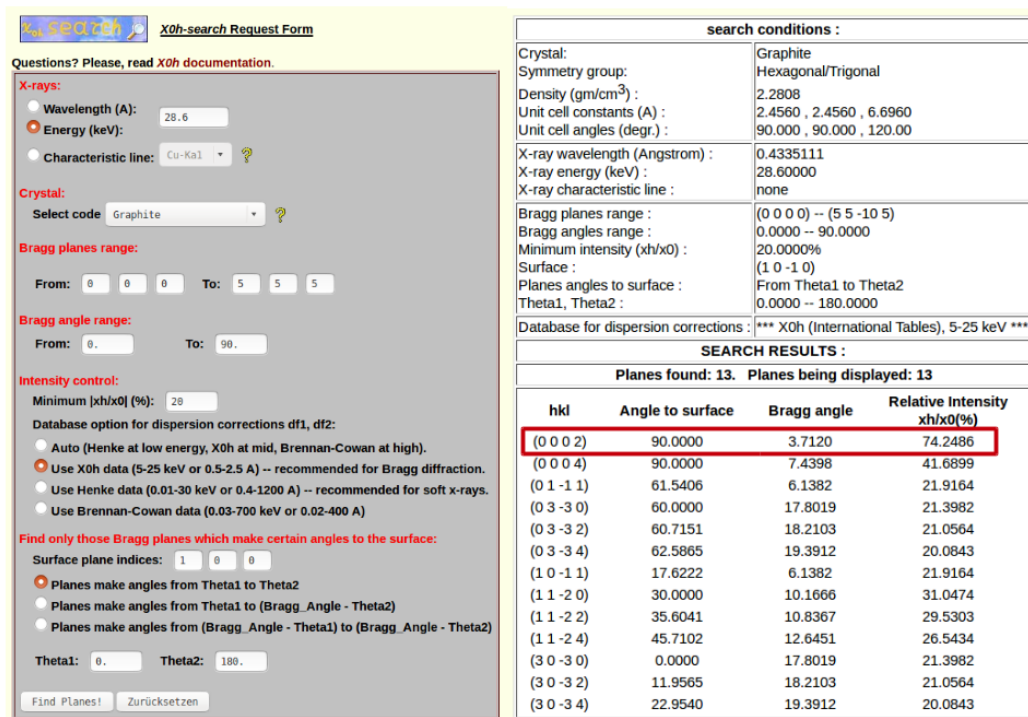


**Figure 9.1:** Graphical user interface of X0h with the search form for all crystal planes fulfilling the Bragg condition for an incident energy of  $E = 28.6$  keV (left) and the result form (right) showing that the 002 plane of HOPG meets the Bragg condition for a Bragg angle of about  $3.7^\circ$ .

Running the programme with these parameters yields a 2D and 3D representation of the reflection profile of the HOPG crystal. Figure 9.2 shows the HOPG reflection on the 002 and 004 plane for a Bragg angle of  $3.7^\circ$ . The data can be saved in ASCII format and used for calculating the effect of the energy selection throughout the crystal. For that purpose, the XOP data is approximated by a combination of Gauss curves and an additional linear function representing the electronic noise of the detector, and subsequently multiplied with the data obtained from the GEANT4 simulation. This yields an intermediate state of the results, considering the reflection pattern of the HOPG crystal, but neglecting all important detector effects besides electronic noise. Hence, the data is further processed in order to gain a realistic representation of the energy spectrum.

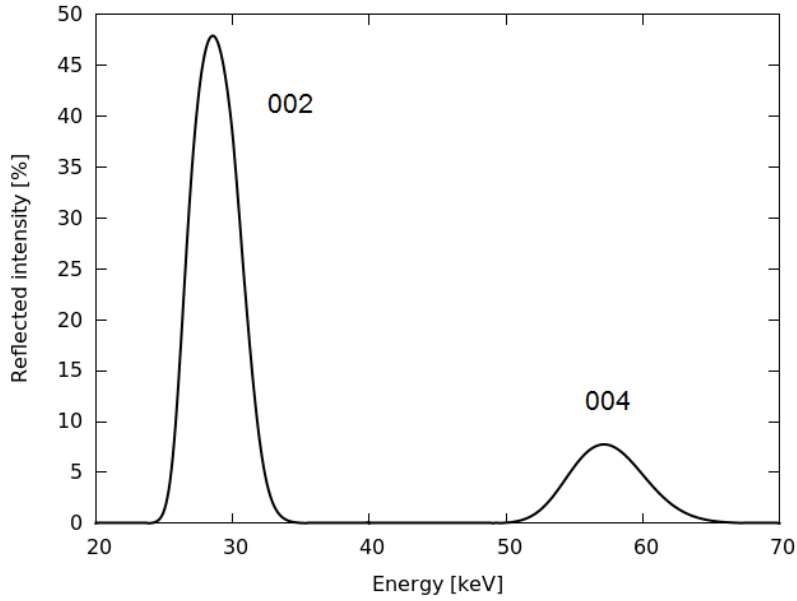


**Figure 9.2:** Reflection pattern of the 002 and 004 plane of the HOPG crystal. For a Bragg angle of incidence equal to  $\approx 3.7^\circ$ , the dominant reflections occur around an energy of about 28.6 keV with a FWHM  $\approx 3.2$  keV, and around an energy of about 56.2 keV with a FWHM  $\approx 6.4$  keV.

### 9.3.2 Detector resolution

In order to gain an energy spectrum with a realistic energy resolution as produced by the CdTe detector used in the experiments, it is necessary to apply a Gaussian filter. For that purpose a C++ code was written that produces random numbers around each distribution mean  $\mu$  with a distinct standard deviation  $\sigma$  for each energy bin, starting with the lowest energy channel  $\mathcal{X}_1$ . This uncertainty  $\sigma$  can be derived according to the relation of  $\sigma$  and the FWHM (cp. subsection 3.1.3) where for Gaussian functions

$$FWHM [eV] = 2\sqrt{2\ln(2)} \sigma \approx 2.35 \sigma. \quad (9.1)$$

Neither FWHM nor  $\sigma$  are constant since the energy resolution of the CdTe detector decreases with increasing energy. Therefore an empirically derived formula calculating  $\sigma$  for each energy channel was derived based on the specifications for various energies given by the manufacturer of the detector:

$$\sigma = (c + \mathcal{X}[keV]) / (2\sqrt{2\ln(2)}). \quad (9.2)$$

The constant  $c$  is an empirically derived factor. After applying the Gaussian filter, the energy bins with a size of 1 eV can be summed up to larger bin sizes depending on the detector type. For comparing the simulations to the experimental results obtained in part II, *Experimental investigation*, the simulated energy bins were grouped together into bins of 86 eV according to the approximate channel size of the CdTe detector used in this work.

## 10. Results: Comparison of simulated and experimental results

This chapter serves as the validation of the Monte Carlo XRF code by comparing the simulated results to the experimental results obtained in part II, *Experimental investigation*, of this work.

The number of initial photons used for the simulations was derived empirically because of uncertainties introduced by the following factors: The size and flux of the anode spot varies with time and hence introduces an uncertainty into the number of emitted photons. Also the initial beam is collimated by a hole collimator before interacting with the phantom. Additionally the photons emitted by the phantom are collimated by a slit collimator before hitting the detector sensitive area. In the case of the experimental setup including the HOPG crystal, a number of photons of roughly 50% in the region of 28.6 keV is discarded before interacting with the detector sensitive area. After estimating the amount of initial photons to  $10^8$  -  $10^{11}$  photons and performing various simulations, it has been empirically found that for the used spectrum ( $U_A = 80$  kV,  $I = 37.5$  mA and 1.0 mm Al filter) an amount of  $5 \cdot 10^9$  initial photons corresponds to an irradiation time of  $\approx 120$  seconds.

Section 10.1 presents and analyses the simulated results using the PMMA/mouse phantom (phantom 2) and the Eppendorf test tube phantom (phantom 1) filled with various iodine concentrations. A simulated analysis of the background scatter distribution is provided in section 10.2.

### 10.1 Simulations of various iodine concentrations

With the initial spectrum ( $U_A = 80$  kV,  $I = 37.5$  mA and 1.0 mm Al filter) and  $5 \cdot 10^9$  initial photons, various XRF simulations were performed using the PMMA/mouse phantom (phantom 2) and the simple Eppendorf test tube (phantom 1). As in the experiments (section 7.2) each phantom was used in a sequence with an imaging setup omitting and including the HOPG crystal. In total, four simulation series were performed and compared to the experimental results.

### 10.1.1 PMMA/mouse phantom (phantom 2)

For the XRF simulations the PMMA/mouse phantom was filled with the same iodine concentrations as for the experiments performed in chapter 7, namely 0.6 mg/ml, 1.2 mg/ml, 2.3 mg/ml and 5.0 mg/ml. Also, a simulation was performed without iodine. Figure 10.1 compares the simulated (left) and experimental (right) results performed with phantom 2 using an iodine concentration of 5.0 mg/ml, without (top) and with (bottom) the HOPG crystal. The overall shape of the simulated spectra agrees well with the experimentally derived results. However, there are two significant differences: i) The shape of the experimentally recorded XRF spectrum without HOPG is slightly distorted compared to the simulated spectrum. ii) Both experimentally derived spectra exhibit clearly visible contributions in energy regions below 15 keV. Both effects are caused by the detector characteristics, which can only be compensated by the simulation chain to a certain degree. The stripping algorithm applied to the raw data recorded with the CdTe detector significantly improves the XRF spectrum but is based on assumptions that introduce uncertainties.

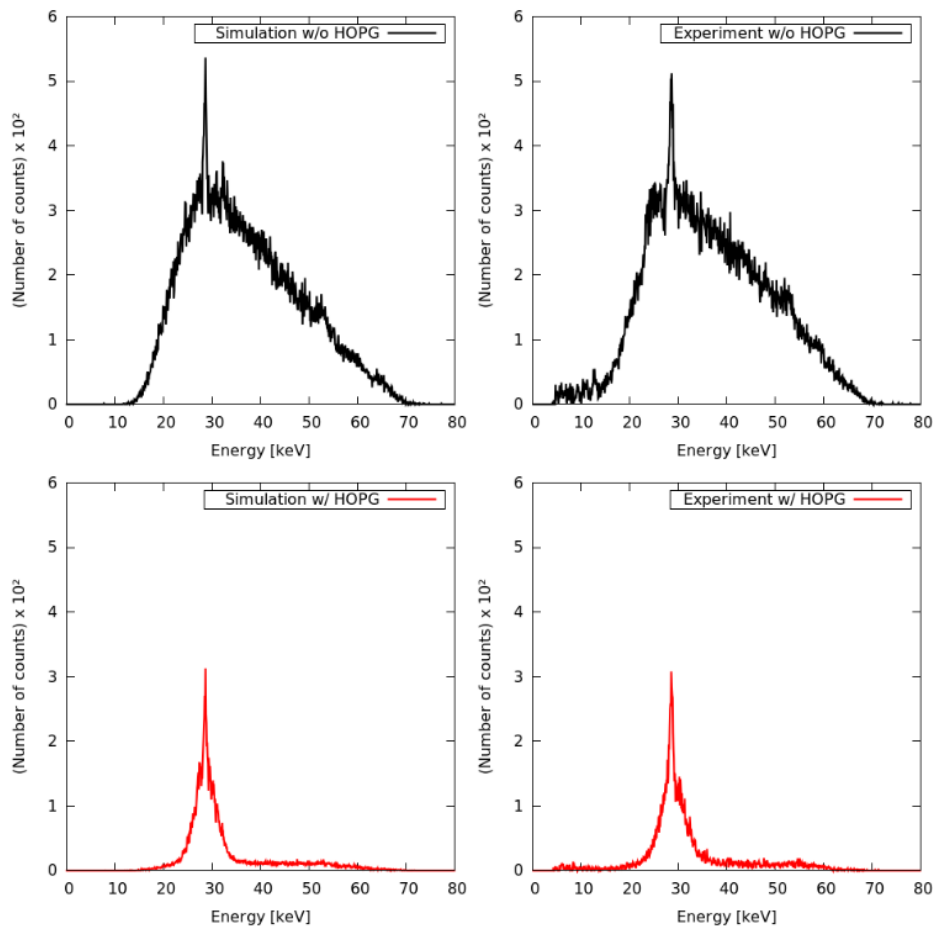


**Figure 10.1:** Comparison of the simulated (left) and experimentally recorded (right, cp. figure 7.7) spectra emitted by the PMMA/mouse phantom filled with an iodine concentration of 5.0 mg/ml. The top row displays the results generated without HOPG and the bottom row shows the results obtained including the HOPG crystal.

	<i>w/o HOPG</i>		<i>w/ HOPG</i>	
<b>I [mg/ml] [kV]</b>	<b>SNR</b>		<b>SNR</b>	
<b>SIMULATION</b>				
<b>0.6</b>	3.51 ± 0.43	(± 12.3 %)	2.48 ± 0.43	(± 17.3 %)
<b>1.2</b>	4.07 ± 0.49	(± 12.0 %)	3.07 ± 0.41	(± 13.4 %)
<b>2.3</b>	6.21 ± 0.53	(± 8.5 %)	5.04 ± 0.53	(± 10.5 %)
<b>5.0</b>	12.49 ± 0.94	(± 7.5 %)	9.49 ± 0.99	(± 10.4 %)
<b>EXPERIMENT</b>				
<b>0.6</b>	2.12 ± 0.75	(± 35.4 %)	2.01 ± 0.69	(± 34.3 %)
<b>1.2</b>	2.59 ± 0.76	(± 29.3 %)	2.28 ± 0.76	(± 33.3 %)
<b>2.3</b>	4.55 ± 1.16	(± 25.5 %)	4.41 ± 1.41	(± 32.0 %)
<b>5.0</b>	9.81 ± 2.11	(± 21.5 %)	8.28 ± 2.12	(± 25.6 %)

**Table 10.1:** SNRs of XRF simulations and measurements (cp. table 7.3) without and with HOPG produced with the PMMA/mouse phantom, filled with various iodine concentrations. The SNR is provided with its absolute error and the percentage in parentheses represents its relative error.

Moreover, the algorithm cleanses the spectrum from erroneous counts introduced by the interactions of X-ray photons and the detector material. Spurious counts caused by electronic noise cannot be removed by the stripping algorithm. As for the experimental results including the HOPG, the simulation shows the 50 % reduction of the energy region around the iodine  $K_\alpha$  fluorescence line and the suppression of other energy regions. Also, as for the experimental results, the area around the second order reflection of the 004-plane at about 57.2 keV is slightly increased in the simulated spectrum. The simulated spectrum including the HOPG crystal exhibits less fluctuations in counts between the energy bins than the corresponding experimental spectrum, which is a consequence of the method used to process the data (cp. section 9.3): Since **GEANT4** version 10.00 does not offer the possibility to account for mosaic crystal materials, the effect of the HOPG crystal has to be applied on the results of the **GEANT4** simulations, which exhibit a total number of counts comparable to that of a recorded or simulated spectrum without the HOPG crystal.

Table 10.1 summarises the results of the XRF spectra for each iodine concentration, displaying the SNR for both simulated setups including and omitting the implementation of the HOPG crystal. In addition the experimental results for the SNRs of table 7.3 are included for reasons of comparison. The values of the simulated and experimentally derived SNRs agree well considering the values for the uncertainties.

Figure 10.2 visualises the SNRs of the simulated/experimentally recorded spectra without (left) and with (right) HOPG crystal and demonstrates that both results are in agreement.

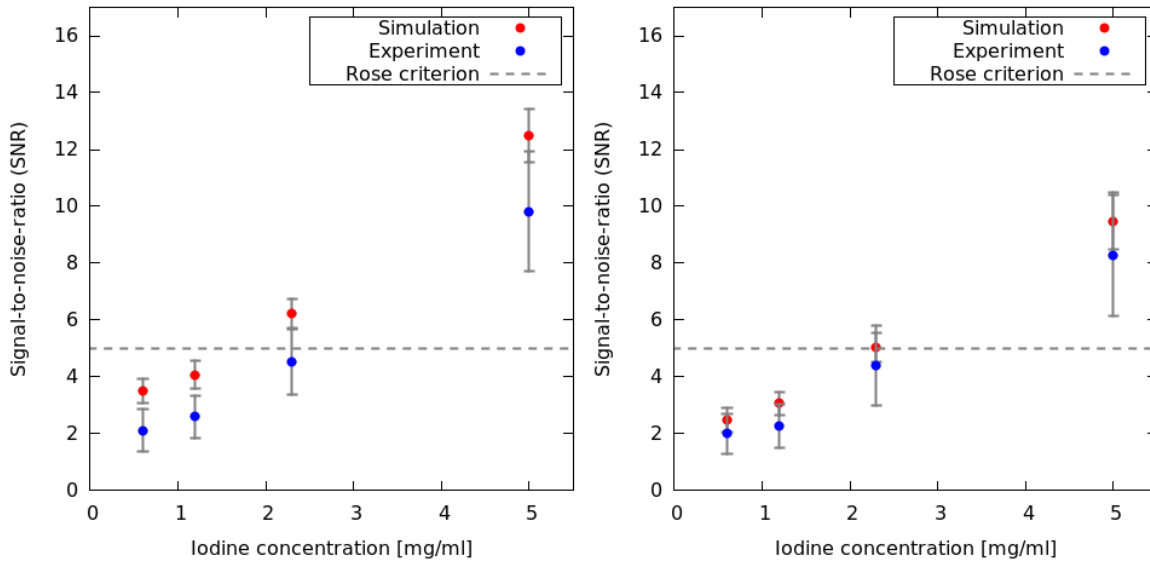


**Figure 10.2:** SNRs of simulated (red) and experimentally recorded (blue, cp. figure 7.8) XRF spectra without (left) and with (right) HOPG crystal emitted from the PMMA/mouse phantom, applying various iodine concentrations between 0.6 mg/ml and 5.0 mg/ml.

### 10.1.2 Eppendorf phantom (phantom 1)

This subsection compares the simulated results to the XRF measurements recorded using the Eppendorf test tube phantom. The simulations were performed using the same contrast agent concentrations as for the experiments: 0.15 mg/ml, 0.3 mg/ml, 0.6 mg/ml, 1.2 mg/ml, 2.3 mg/ml and 5.0 mg/ml. An additional simulation was performed without contrast agent. Along the lines of the previous subsection, figure 10.3 shows the simulated (left) and experimental (right) results performed with phantom 1 using an iodine concentration of 5.0 mg/ml, without (top) and with (bottom) the HOPG crystal. As for the experimental results the  $K_{\beta}$  emission line is clearly visible in the simulated spectrum. The artefact at roughly 5 keV due to escape events is not visible in the simulated XRF spectra. The experimentally recorded spectra show the same distortions compared to the simulated spectra as explained in the previous subsection. However, the additional contributions in energy regions below 15 keV are less pronounced than in the results for the PMMA/mouse phantom, which are therefore being assumed to be a consequence of the phantom size. In table 10.2 the SNRs of the XRF spectra for each iodine concentration in both simulated setups with and without the HOPG crystal are listed. For ease of comparison the experimental results of table 7.4 are also included. As in the previous section, the values of the simulated and experimentally derived SNRs agree well within the calculated uncertainties. Figure 10.4 visualises the values of table 10.2 displaying results without (left) and with (right) HOPG crystal.

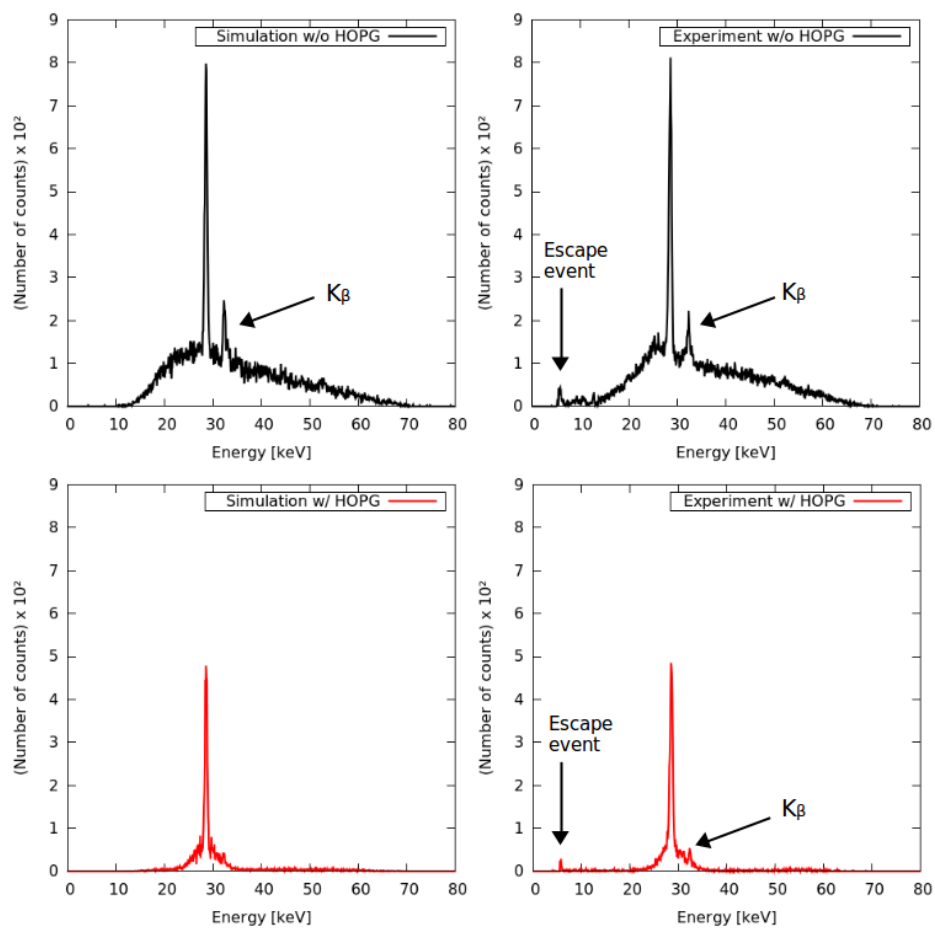


**Figure 10.3:** Comparison of the simulated (left) and experimentally recorded (right, cp. figure 7.9) spectra emitted by the Eppendorf test tube phantom filled with an iodine concentration of 5.0 mg/ml. The top row displays the results generated without HOPG and the bottom row shows the results obtained including the HOPG crystal.

	<i>w/o HOPG</i>		<i>w/ HOPG</i>	
I [mg/ml] [kV]	SNR		SNR	
<b>SIMULATION</b>				
0.15	$3.54 \pm 0.54$	( $\pm 15.7\%$ )	$2.50 \pm 0.55$	( $\pm 22.0\%$ )
0.3	$4.72 \pm 0.61$	( $\pm 12.9\%$ )	$3.34 \pm 0.63$	( $\pm 18.9\%$ )
0.6	$6.78 \pm 0.69$	( $\pm 10.2\%$ )	$4.80 \pm 0.70$	( $\pm 14.6\%$ )
1.2	$8.79 \pm 0.75$	( $\pm 8.5\%$ )	$6.22 \pm 0.76$	( $\pm 12.2\%$ )
2.3	$13.09 \pm 0.84$	( $\pm 6.4\%$ )	$9.26 \pm 0.86$	( $\pm 9.3\%$ )
5.0	$22.05 \pm 0.91$	( $\pm 4.1\%$ )	$16.17 \pm 0.93$	( $\pm 5.8\%$ )
<b>EXPERIMENT</b>				
0.15	$3.37 \pm 1.03$	( $\pm 30.6\%$ )	$1.55 \pm 0.83$	( $\pm 53.5\%$ )
0.3	$1.59 \pm 0.61$	( $\pm 38.4\%$ )	$2.67 \pm 1.17$	( $\pm 43.8\%$ )
0.6	$6.03 \pm 1.56$	( $\pm 25.9\%$ )	$5.26 \pm 1.69$	( $\pm 32.1\%$ )
1.2	$8.84 \pm 2.07$	( $\pm 23.4\%$ )	$8.21 \pm 2.21$	( $\pm 26.9\%$ )
2.3	$13.95 \pm 2.94$	( $\pm 21.1\%$ )	$12.13 \pm 2.70$	( $\pm 22.3\%$ )
5.0	$24.66 \pm 4.63$	( $\pm 18.8\%$ )	$19.56 \pm 3.88$	( $\pm 19.8\%$ )

**Table 10.2:** SNRs of XRF simulations and measurements (cp. table 7.4) without and with HOPG produced with the Eppendorf test tube phantom, filled with various iodine concentrations. The values for the SNRs are given according to table 10.1.

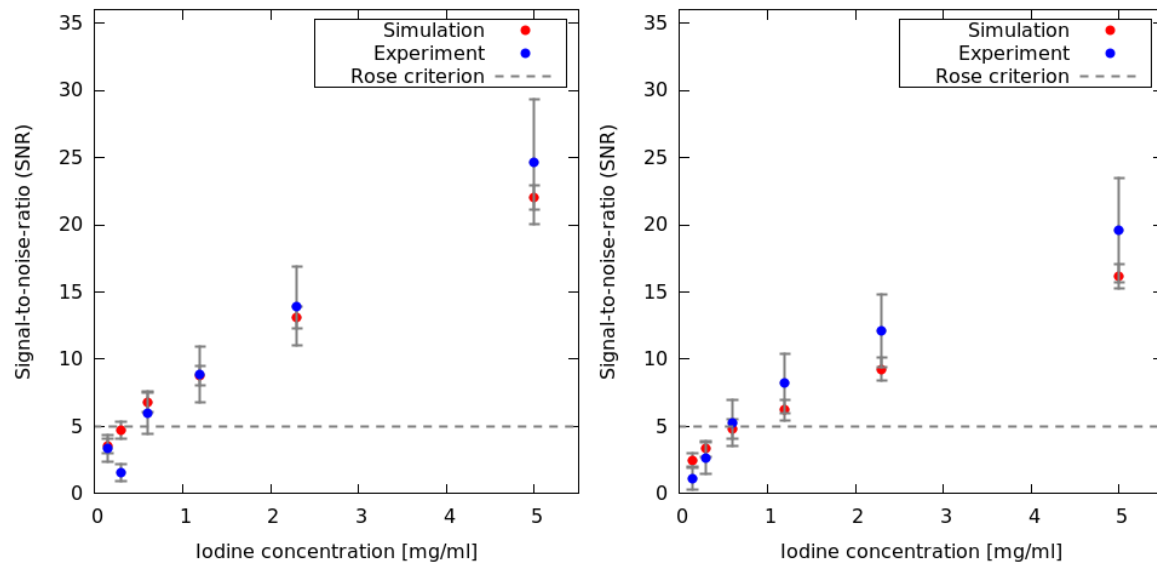


**Figure 10.4:** SNRs of simulated (red) and experimentally recorded (blue, cp. figure 7.10) XRF spectra without (left) and with (right) HOPG crystal emitted from the Eppendorf test tube phantom, applying various iodine concentrations between 0.15 mg/ml and 5.0 mg/ml.



### 10.1.3 Contributions of multiple scattered photons

Simulations of the experimental setup with `GEANT4` allow the contributions of multiple scattered photons to the final XRF spectrum to be displayed. The `steppingAction` module can be used to read out data about all photons after every `step` of the Monte Carlo code (cp. section 8.1). Figure 10.5 displays the results for the simulated XRF spectra for the PMMA/mouse phantom (left) and the Eppendorf test tube phantom (right) for a simulated iodine concentration of 5.0 mg/ml (top without, bottom with HOPG). The results clearly show the influence of the phantom size on the amount of interactions a photon undergoes before hitting the detector sensitive area. Whereas for the PMMA/mouse phantom the amount of background photons is approximately evenly composed of multiple scattered photons, the XRF signal emitted by the Eppendorf test tube phantom is predominantly contaminated by single scattered background photons. Although the imaging setup included a slit collimator in order to shield the detector from scatter, there is still a large amount of multiple scattered photons, as is particularly visible in the PMMA/mouse phantom spectrum.

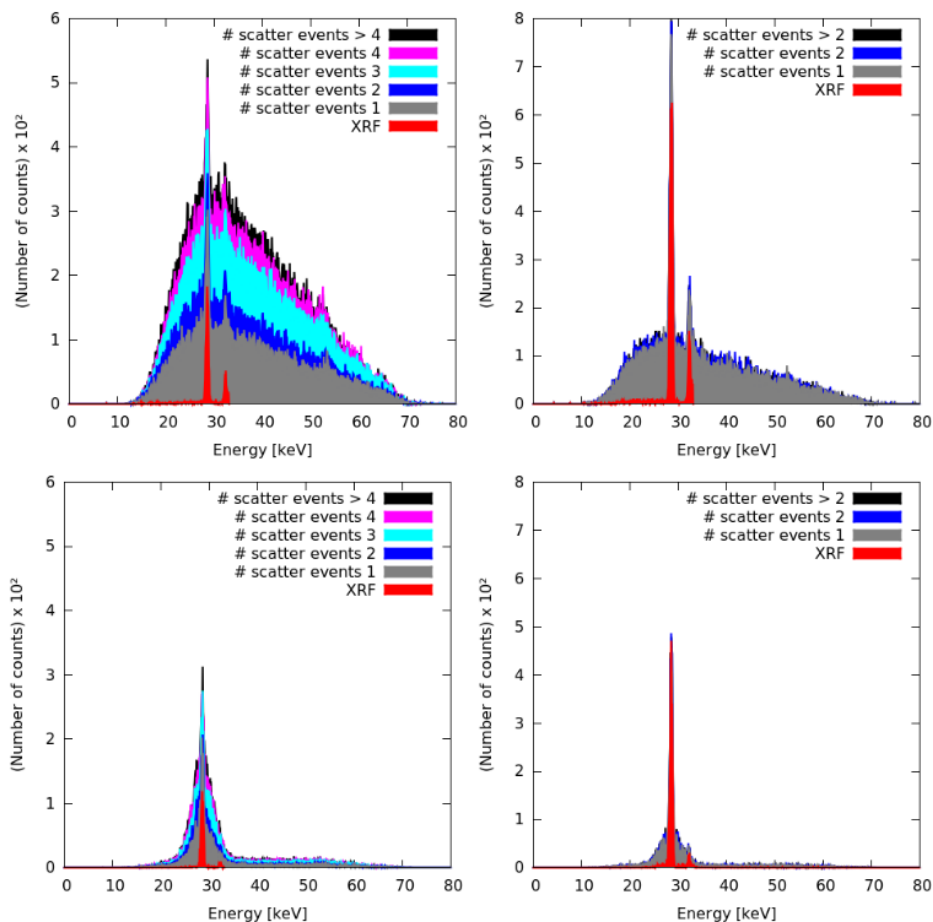


**Figure 10.5:** Simulated XRF spectra of the PMMA/mouse phantom (left) and the Eppendorf test tube phantom (right) filled with an iodine concentration of 5.0 mg/ml, divided in numbers of scattering events. Top: without HOPG; Bottom: with HOPG.

## 10.2 Simulation of the background distribution

In order to complete the validation of the Monte Carlo XRF code, the angular background distribution of photons emitted from two different phantoms was simulated and compared to the findings presented in section 7.1.3. A series of simulations was performed building an XRF imaging setup without HOPG and irradiating the PMMA/mouse phantom (phantom 2) and phantom 3 with the initial spectrum ( $U_A = 80$  kV,  $I = 37.5$  mA and 1.0 mm Al filter) from varying angles between  $10^\circ$  and  $170^\circ$ . Phantom 2 was simulated without iodine. As in the experimentally recorded measurements the measuring time was set to 60 seconds, which for the simulations is equivalent to about  $2.5 \cdot 10^9$  photons.

Figure 10.6 compares the results of the angular dependency for the measured (black dots) and simulated (red squares) photon flux emitted by phantom 2 (left) and phantom 3 (right). Statistical simulation errors concerning the number of counts have been neglected, since the error bars were situated within the points. The shape of the simulated angle-dependent function is in overall accordance with the angular course of the experimentally derived data. Some points, however, show a difference in the amount of photons, which could be a consequence of the unevenly distributed photon flux emitted by the anode spot and an effect of the stripping algorithm.

Nevertheless, the simulated results follow the same trend as the experimental results, and thus confirm the implications already derived from the experimentally derived photon numbers: The imaging setup is suitable for implementing a  $90^\circ$  angular detector configuration and for using a large area detector extending to adjacent angular positions.

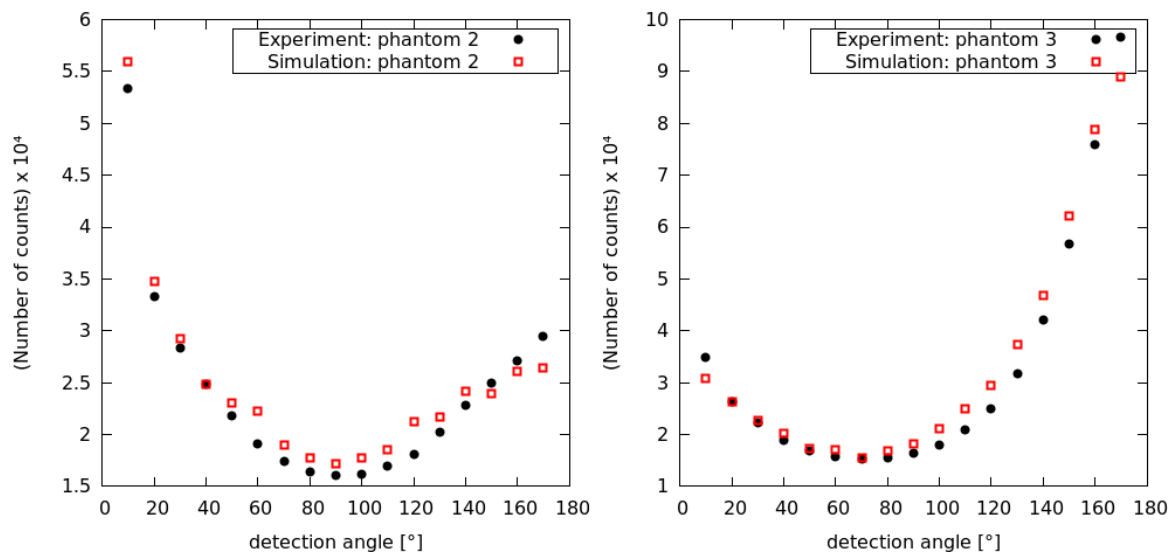


**Figure 10.6:** Comparison of the simulated background distribution with the measured background for the PMMA/mouse phantom (left) and phantom 3 (right).

## 11. Influence of detector characteristics and mosaicity

One of the major challenges of XRF imaging is the isotropic emission of fluorescence photons and the related loss of information, due to the small sensitive areas of conventional semiconductor XRF detectors. However, these detectors are particularly suitable for XRF imaging since they provide a high sensitivity, an energy resolution of less than 1 keV in the EROI (28.6 keV) and small bin sizes ( $< 100$  eV) which correlates with a high specificity. In contrast, large area detectors generally exhibit energy resolutions of several keV and large bin sizes (1 to several keV), thus significantly impairing the sensitivity. Implementing a large detection area leads to increased counting statistics and consequently allows for reduced exposure times and smaller concentrations of contrast agent. This larger detection area could be achieved by installing several semiconductor XRF detectors, which however would considerably raise the costs. Another approach, which is subject of this chapter, is the implementation of a large area detector with reduced energy resolution and large bin size, together with an energy-selective HOPG crystal. To a certain extent the crystal compensates for the limited energy resolution at large bin sizes and thus enables the use of large area detectors for XRF imaging.

This chapter makes use of the developed XRF Monte Carlo code, which has been verified in the previous chapter, in order to study the effects of the HOPG crystal on the XRF signal recorded with a large area detector with moderate energy resolution and increased bin size. All results in this section have been simulated with the

Detector Sizes [mm <sup>2</sup> ]		Bin sizes [keV]
27	3 × CdTe	5.0
90	10 × CdTe	7.5
270	30 × CdTe	10.0
900	100 × CdTe	12.5
2700	300 × CdTe	15.0
9000	1000 × CdTe	17.5
27000	3000 × CdTe	20.0
		30.0
		40.0
		50.0
		100.0

**Table 11.1:** *List of investigated sensitive detector areas and bin sizes.*

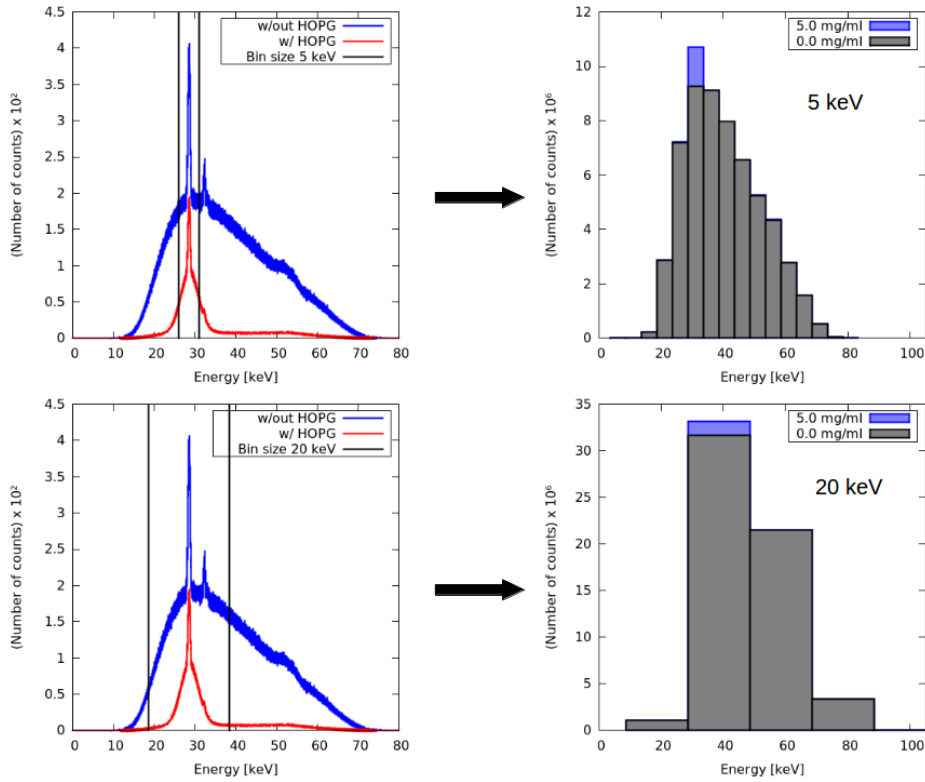


**Figure 11.1:** Example spectra and histograms with different bin sizes. Top row: Spectrum including a suggested binning of 5 keV (left), and the resulting histogram (right). Bottom row: Suggested binning of 20 keV (left) and the respective histogram (right).

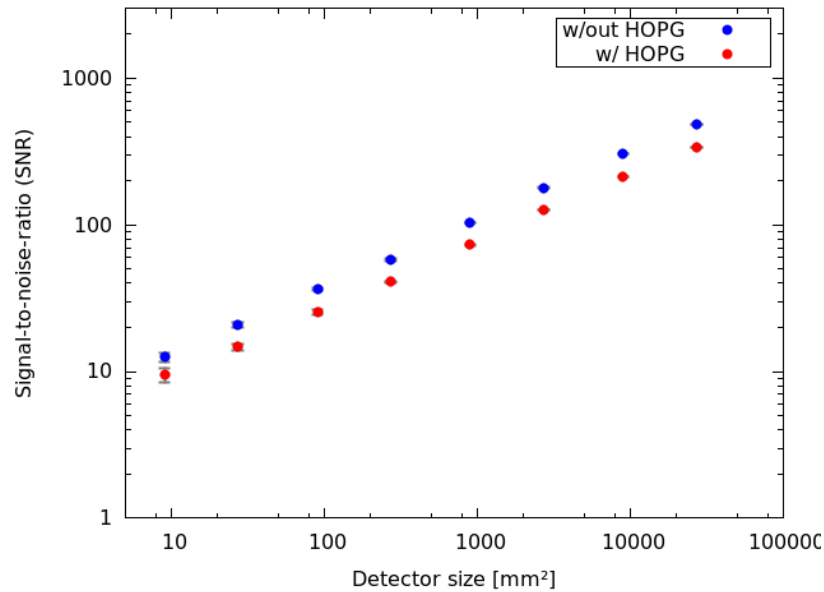
PMMA/mouse phantom and the initial spectrum used in the previous chapter with the specifications  $U_A = 80$  kV,  $I = 37.5$  mA and 1.0 mm Al filter. The amount of initial X-ray photons of  $5 \cdot 10^9$  corresponds to a recording time of about 2 minutes. Unless stated otherwise, a detector resolution of  $\approx 0.48$  keV in the EROI (28.6 keV) was used, corresponding to the CdTe detector used in the experiments as well as in chapter 10. All simulated detector sizes are multiples of the CdTe detector which has a sensitive area of  $9 \text{ mm}^2$ . Each detector is cylindrically shaped and positioned such that every detector part is situated at a distance of 10 cm from the centre of the phantom. Table 11.1 lists all detector sizes used in this study ranging up to  $27000 \text{ mm}^2$  which equals 3000 times the size of the CdTe detector. The table also summarises all bin sizes used in this investigation, ranging from 5 keV to 100 keV ( $\hat{=}$  no binning).

Figure 11.1 delineates the binning process: The initial XRF spectrum is a spectrum with a binning of 1 eV and an underlying intrinsic detector resolution of 0.48 keV in the EROI, corresponding to the CdTe detector used in the experimental part of this work. The target bin sizes were formed via summation of the 1 eV bins such that the EROI is situated in the centre of the resulting bin size. In this investigation the  $K_\beta$  line of iodine was discarded for the following reason: The HOPG crystal suppresses the energy region around the  $K_\beta$  line, such that the  $K_\beta$  signal is hardly apparent for the experimental setup including the HOPG crystal. In contrast, in the setup without the HOPG crystal,  $K_\beta$  can be discriminated if the iodine concentration is sufficiently high.  $K_\beta$  emission is significantly less probable than  $K_\alpha$  emission, and is

not discriminable from the background at iodine concentrations where  $K_\alpha$  emission is still prominent. This study aims for analysing the feasibility of the HOPG crystal with respect to the lowest necessary iodine concentration, where  $K_\beta$  would not be apparent. Therefore, in order to draw conclusions from results with sufficiently analysable iodine concentrations to the lowest possible iodine concentrations, the  $K_\beta$  was discarded. Also, the transition from SNR of the spectra with bin sizes not including the  $K_\beta$  line in the signal bin to those with bin sizes including it, would be characterised by a sudden increase of the SNR. Drawing conclusions to results with the lowest possible iodine concentration would be complicated and error-prone.

Section 11.1 investigates the influence of the detector size and the bin size on the SNR and the sensitivity and compares the results for XRF spectra recorded with and without the HOPG crystal. Section 11.2 deals with the influence of the intrinsic detector resolution on the SNR while section 11.3 scrutinises the effects of mosaicity on the results. The final section ?? combines the effects of intrinsic detector resolution and mosaicity on the XRF results.

## 11.1 Detector size and bin size



**Figure 11.2:** SNRs of XRF spectra with an iodine concentration of 5.0 mg/ml recorded with detector sizes between 9 mm<sup>2</sup> and 27000 mm<sup>2</sup> (logarithmic scale).

The influence of the chosen detector size on the resulting detection ability of a certain contrast agent concentration is shown in figure 11.2. The figure displays the SNRs of XRF spectra using the PMMA/mouse phantom with an iodine concentration of 5.0 mg/ml recorded with detector sizes between 9 mm<sup>2</sup> and 27000 mm<sup>2</sup>. As expected, the SNR scales with the square root of the detector size:

$$\text{SNR} \sim c \sqrt{\text{Detector size}}, \quad (11.1)$$

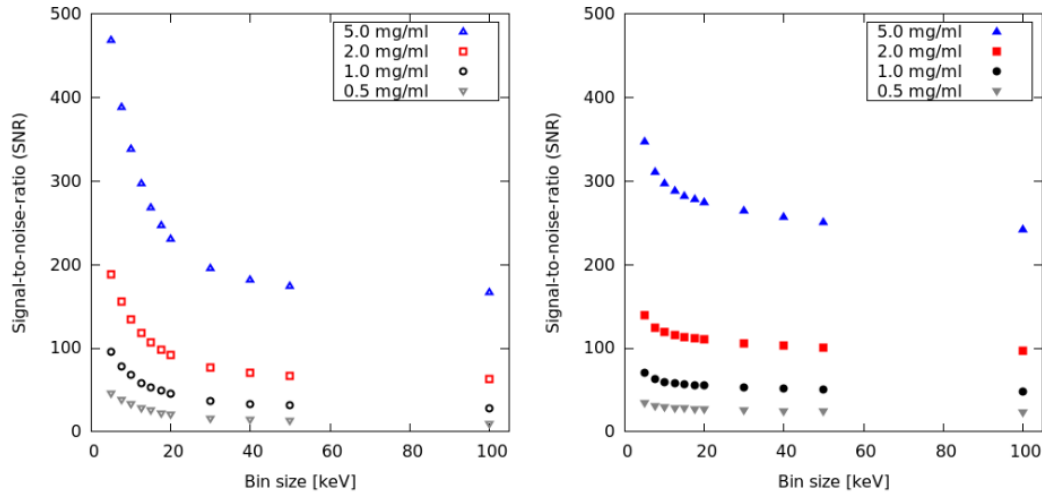


**Figure 11.3:** SNRs calculated for bin sizes between 5 and 100 keV recorded with a detector size of 9000 mm<sup>2</sup> and various iodine concentrations between 0.5 and 5.0 mg/ml for an experimental setup omitting (left) and including (right) the HOPG crystal.

where  $c$  is a constant that depends on the binning, angular detection configuration, and phantom characteristics. As in the results of the previous chapter, the SNR for the spectra recorded with HOPG crystals is consistently smaller than the SNR recorded without crystals. This is due to the method of calculating the SNR explained in section 5.2. As explained in section 7.1 for a bin size of 86 eV, the ratio of signal height to background height for the simulations with the crystal is at least equal to the corresponding ratios of the results without HOPG.

Figure 11.3 summarises the effect of the bin size on the resulting SNR: The SNRs of all bin sizes listed in table 11.1 are calculated for a detector size of 9000 mm<sup>2</sup> (1000 × CdTe) and iodine concentrations between 0.5 mg/ml and 5.0 mg/ml for an experimental setup without (left) and with (right) the HOPG crystal. Error bars were neglected since they are situated within the symbols. The SNRs of the setup omitting the HOPG drops at a faster rate than the SNRs of the setup including the crystal.

Figure 11.4 compares the decline for a setup with and without HOPG crystals for an iodine concentration of 1.0 mg/ml and a detector size of 9000 mm<sup>2</sup>. For a binning  $\geq 15$  keV the resulting SNR of the HOPG setup exceeds the SNR of the setup omitting the crystal, which highlights the effect of the HOPG crystal. For a binning of 15.0 keV the value for the SNR obtained with the setup including the HOPG exceeds the value obtained without crystal by 7.15%. For a detector with a bin size of 100 keV, the HOPG outperforms the non-HOPG setup by 71.34%. The SNR values for all binnings for a detector size of 9000 mm<sup>2</sup> and an iodine concentration of 1.0 mg/ml are listed in Appendix V.B table B.1.

The positive effect of the HOPG also holds for other initial spectra as well as the one used for all simulations in this chapter. Figure 11.5 compares the decline of the SNR with bin size for a setup with and without HOPG crystal for an initial spectrum using  $U_A = 160$  kV. As has already been explained in chapter 7 in the experimental part of this work, the amount of photons in higher energy regions considerably increases

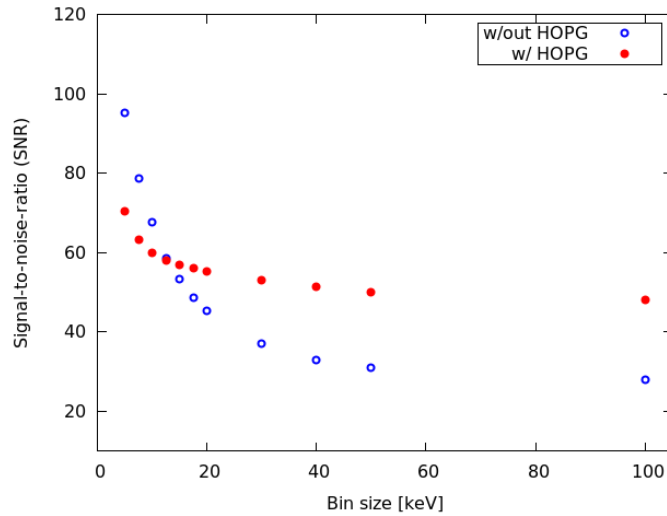


**Figure 11.4:** Comparison of the decline of the SNR with bin size for an experimental setup without (blue rings) and with (red circles) the HOPG crystal (initial spectrum:  $U_A = 80$  kV, iodine concentration: 1.0 mg/ml, detector size: of 9000 mm<sup>2</sup>). For bin sizes  $\geq 15$  keV the implementation of the HOPG yields a higher SNR.

with the applied high voltage  $U_A$ . Therefore, it seems to be advantageous to use initial spectra with a reduced number of counts in energy regions above the EROI. However, figure 11.5 clearly shows that the suppressing effect of the HOPG of energy parts outside the EROI is not affected by the amount of counts in energy parts above the EROI: Here, the resulting SNR of the HOPG setup exceeds the SNR of the setup without HOPG for a binning  $\geq 12.5$  keV.

Table 11.2 summarises the results of the simulations with/without HOPG performed with the PMMA/mouse phantom, the chosen initial spectrum ( $U_A = 80$  kV and 1.0 mm Al filter),  $5 \cdot 10^9$  initial X-ray photons ( $\approx$  recording time of about 2 minutes), and an intrinsic detector resolution of  $\approx 0.48$  keV in the EROI (28.6 keV). The table provides the minimum iodine concentrations for achieving an SNR fulfilling the *Rose criterion* ( $\text{SNR} \geq 5$ ) for all investigated detector and bin sizes. The values show that the iodine concentration needed to fulfil the Rose criterion can be considerably decreased by increasing the detector size.

As discussed for figure 11.4 the SNRs of the setups with/without HOPG exhibit different decay rates, such that the SNRs  $\geq 15$  keV are larger for the configuration including the HOPG crystal compared to the setup omitting it. This is reflected in the minimal iodine concentration fulfilling the Rose criterion, where for increasing bin sizes the minimum detectable iodine concentration is smaller for the HOPG setup compared to the non-HOPG configuration. The imaging setup including the HOPG leads to low decay rates that for larger bin sizes ( $\approx \geq 20$  keV) stagnate at SNR values which are larger than those for the setup without the HOPG. The advantage of this HOPG effect is that the demands on the bin size can be relaxed. For instance, in order to achieve an  $\text{SNR} \geq 5$ , with a 27000 mm<sup>2</sup> detector, the HOPG setup detects  $\approx 0.082$  mg/ml when the bin size equals 100 keV. In order to achieve a comparable result without HOPG, the same energy range needs to be partitioned into 7 bins, resulting in a bin size of

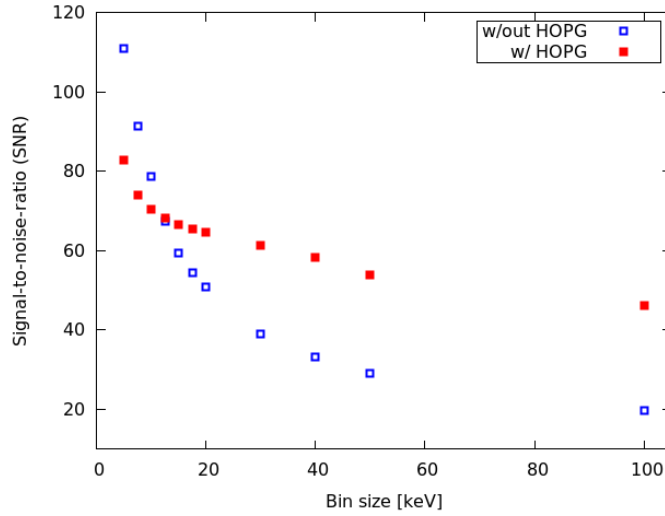


**Figure 11.5:** Comparison of the decline of the SNR with bin size for an experimental setup without (blue squares) and with (red squares) the HOPG crystal (initial spectrum:  $U_A = 160$  kV, iodine concentration: 1.0 mg/ml, detector size: of 9000 mm<sup>2</sup>). For bin sizes  $\geq 12.5$  keV the implementation of the HOPG yields a higher SNR.

15 keV.

The HOPG crystal makes the implementation of large area detectors with reduced intrinsic energy resolution and large binnings for XRF imaging conceivable. This option paves the way for reductions in the X-ray dose by decreasing the time of exposure. The following relation between applied dose and angular detection coverage holds:

$$\Omega \sim d \frac{1}{\text{Dose}}, \quad (11.2)$$

where  $\Omega$  is the solid angle and  $d$  is a constant depending on binning, angular detection configuration and phantom characteristics. Since all results were obtained with the same distance  $r$  between the PMMA/mouse phantom and the detector sensitive area ( $r = 10$  cm), equation 11.2 simplifies (with  $\Omega = (\text{Detector area})/4\pi r^2$ ) to:

$$\text{Detector area} \sim d \frac{1}{\text{Dose}}. \quad (11.3)$$

Maintaining the same amount of iodine concentration, the X-ray dose applied to the phantom can be reduced by increasing the detector sensitive area.



Bin Size	Detector Sizes [mm <sup>2</sup> ]									
	27	90	270	900	2700	9000	27000			
5.0 keV	w/out	4.338 ± 0.390	1.908 ± 0.489	0.864 ± 0.078	0.374 ± 0.034	0.166 ± 0.015	0.074 ± 0.007	0.038 ± 0.003		
	w/	5.430 ± 0.489	2.094 ± 0.188	0.868 ± 0.078	0.389 ± 0.035	0.189 ± 0.017	0.090 ± 0.008	0.048 ± 0.004		
7.5 keV	w/out	7.433 ± 0.669	2.852 ± 0.257	1.232 ± 0.111	0.436 ± 0.039	0.212 ± 0.019	0.081 ± 0.007	0.051 ± 0.005		
	w/	10.636 ± 0.957	2.963 ± 0.267	1.051 ± 0.095	0.426 ± 0.038	0.216 ± 0.019	0.097 ± 0.009	0.053 ± 0.005		
10.0 keV	w/out	9.501 ± 0.855	2.334 ± 0.210	1.379 ± 0.124	0.473 ± 0.043	0.221 ± 0.020	0.091 ± 0.008	0.061 ± 0.005		
	w/	11.157 ± 1.004	2.772 ± 0.249	1.100 ± 0.099	0.443 ± 0.040	0.220 ± 0.020	0.101 ± 0.009	0.059 ± 0.005		
12.5 keV	w/out	12.899 ± 1.161	3.874 ± 0.349	1.737 ± 0.156	0.587 ± 0.053	0.235 ± 0.021	0.106 ± 0.010	0.071 ± 0.006		
	w/	11.639 ± 1.048	2.899 ± 0.261	1.150 ± 0.104	0.457 ± 0.041	0.223 ± 0.020	0.104 ± 0.009	0.061 ± 0.005		
15.0 keV	w/out	15.371 ± 1.383	5.753 ± 0.518	2.060 ± 0.185	0.709 ± 0.064	0.245 ± 0.022	0.118 ± 0.011	0.089 ± 0.008		
	w/	12.018 ± 1.082	2.974 ± 0.268	1.189 ± 0.107	0.467 ± 0.042	0.225 ± 0.020	0.106 ± 0.010	0.063 ± 0.006		
17.5 keV	w/out	18.621 ± 1.676	7.332 ± 0.660	2.440 ± 0.220	0.813 ± 0.073	0.275 ± 0.025	0.135 ± 0.012	0.092 ± 0.008		
	w/	12.355 ± 1.112	3.046 ± 0.274	1.222 ± 0.110	0.477 ± 0.043	0.229 ± 0.021	0.109 ± 0.010	0.064 ± 0.006		
20.0 keV	w/out	22.928 ± 2.064	9.126 ± 0.821	2.791 ± 0.251	0.977 ± 0.088	0.319 ± 0.029	0.147 ± 0.013	0.096 ± 0.009		
	w/	12.706 ± 1.144	3.095 ± 0.279	1.253 ± 0.113	0.487 ± 0.044	0.234 ± 0.021	0.111 ± 0.010	0.065 ± 0.006		
30.0 keV	w/out	26.243 ± 2.362	11.244 ± 1.012	3.808 ± 0.343	1.458 ± 0.131	0.465 ± 0.042	0.230 ± 0.021	0.120 ± 0.011		
	w/	13.616 ± 1.225	3.310 ± 0.298	1.374 ± 0.124	0.511 ± 0.046	0.249 ± 0.022	0.119 ± 0.011	0.069 ± 0.006		
40.0 keV	w/out	31.778 ± 2.860	12.254 ± 1.103	4.432 ± 0.399	1.699 ± 0.153	0.593 ± 0.053	0.279 ± 0.025	0.127 ± 0.011		
	w/	14.369 ± 1.293	3.584 ± 0.323	1.453 ± 0.131	0.531 ± 0.048	0.269 ± 0.024	0.124 ± 0.011	0.070 ± 0.006		
50.0 keV	w/out	34.367 ± 3.093	13.872 ± 1.248	4.958 ± 0.446	1.835 ± 0.165	0.694 ± 0.062	0.292 ± 0.026	0.143 ± 0.013		
	w/	15.390 ± 1.385	3.935 ± 0.354	1.535 ± 0.138	0.546 ± 0.049	0.290 ± 0.026	0.127 ± 0.011	0.074 ± 0.007		
100.0 keV	w/out	40.003 ± 3.600	14.904 ± 1.341	5.580 ± 0.502	2.400 ± 0.216	0.832 ± 0.075	0.379 ± 0.034	0.190 ± 0.017		
	w/	17.001 ± 1.530	5.453 ± 0.491	1.767 ± 0.159	0.613 ± 0.055	0.321 ± 0.029	0.141 ± 0.013	0.082 ± 0.007		

**Table 11.2:** Lower detection limits for fulfilling an SNR  $\geq 5$  (Rose criterion) for all detector and bin sizes (with/without HOPG).

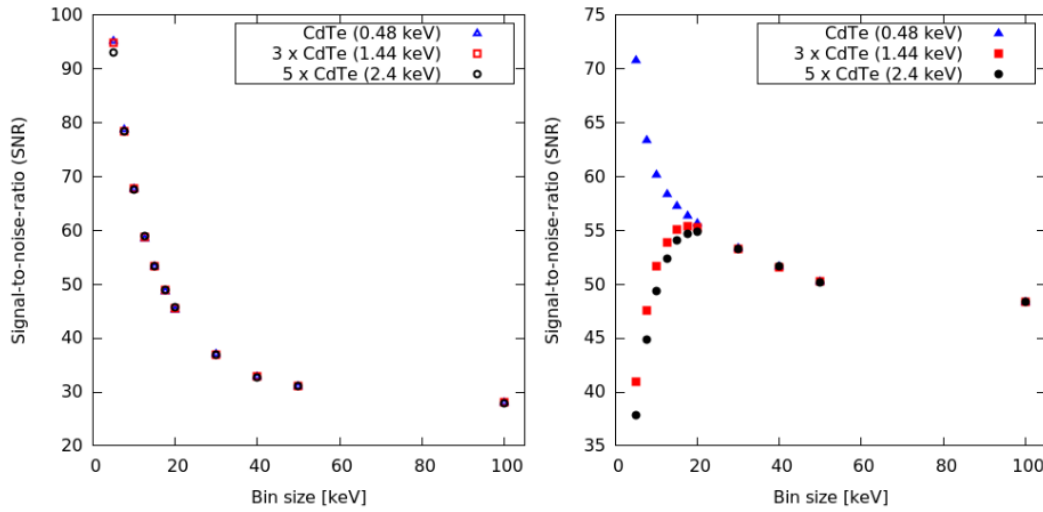


**Figure 11.6:** Comparison of the decline of the SNR with bin size for intrinsic detector resolutions between 0.48 keV and 2.4 keV (FWHM) for a detection setup without (left) and with (right) the HOPG crystal.

## 11.2 Influence of intrinsic detector resolution

Large area detectors generally have fewer bins (resulting in large bin sizes and an inevitable loss of specificity) and a decreased intrinsic detector resolution. The influence of the latter on XRF imaging and how the HOPG crystal alters the result is subject of this section. Figure 11.6 shows the decline of the SNR with increasing bin sizes for simulations without the HOPG (left) and with the HOPG (right) for a detector size of  $9000 \text{ mm}^2$  and intrinsic detector resolutions between 0.48 keV ( $\hat{=}$  CdTe detector) and 2.4 keV ( $\hat{=}$   $5 \times$  CdTe detector) in the EROI. The detector resolution has nearly no effect on the results obtained without HOPG, with the exception of small binnings, where the XRF signal is broadened such that parts of the signal are situated in the neighbouring bins, resulting in a reduced SNR. The same behaviour holds for the SNRs for the HOPG setup (right), with the difference, that for smaller bin sizes, notably more XRF photons are situated in the neighbouring bins, leading to a considerably reduced SNR. Nevertheless, for bin sizes larger than 20 keV, the intrinsic detector resolution has no effect on the SNRs. As has already been discussed in section 11.1, for an intrinsic detector resolution of 0.48 keV the use of the HOPG is advantageous for a bin size  $\geq 15$  keV. In contrast, for a detector resolution of 2.4 keV ( $4 \times$  CdTe) the implementation of the HOPG is advantageous for bin sizes  $\geq 20$  keV. This means that the bin size at which the implementation of the HOPG is advantageous correlates with the intrinsic detector resolution.

### 11.3 Influence of crystal mosaicity

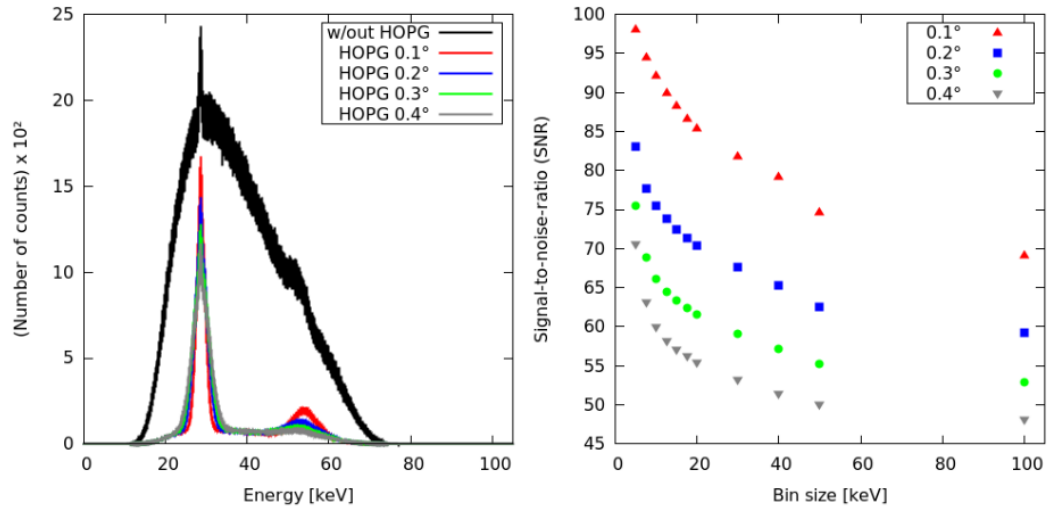


**Figure 11.7:** Influence of the crystal mosaicity on the resulting XRF spectra (left) and the decline with bin size (right).

Implementing crystals with smaller mosaicities ( $< 0.4^\circ$ ) could increase the resulting SNR, since with decreasing mosaic spread the bandwidth of the intrinsic width of Bragg reflection  $\Delta\Theta$  decreases while the peak reflectivity increases. The effect of the crystal mosaicity on recorded XRF spectra and SNRs is shown in figure 11.7 for the mosaicities  $0.1^\circ$ ,  $0.2^\circ$ ,  $0.3^\circ$  and  $0.4^\circ$ . The simulations have been performed with the PMMA/mouse phantom filled with an iodine concentration of 1.0 mg/ml, a detector size of  $9000 \text{ mm}^2$  and an intrinsic detector resolution of 0.48 keV. The left side of figure 11.7 shows the resulting XRF spectra for the respective mosaicities while the right side displays the respective SNR decline with increasing bin size. The increase of peak reflectivity and the decrease of bandwidth for decreasing mosaic spread correlates with a notable increase of the SNR.

For a mosaic spread of  $0.4^\circ$  the use of the HOPG is advantageous over a setup without HOPG at a bin size of  $\geq 15 \text{ keV}$ . A mosaicity of  $0.3^\circ$  improves the SNR such, that at a binning of 12.5 keV the HOPG leads to better results than an implementation omitting it. HOPG crystals with  $0.2^\circ$  mosaic spread improve the SNR for binnings of  $\geq 10 \text{ keV}$  and, for a mosaicity of  $0.1^\circ$ , all bin sizes  $\geq 5 \text{ keV}$  show better results if the HOPG crystal is included in the imaging setup. The exact values of the SNRs for all binnings for a detector size of  $9000 \text{ mm}^2$  and an iodine concentration of 1.0 mg/ml are listed for all investigated mosaicities in Appendix V.B table B.2.

Table 11.3 lists the values for the minimum iodine concentration fulfilling the Rose criterion for each bin size and crystal mosaicity. The percentage in the respective second row indicates the relative decrease of iodine concentration detectable for the respective bin size, compared to the values for the *original* CdTe detector (1st column). A mosaicity of  $0.3^\circ$  reduces the detectable iodine concentration by approximately 7 - 11 % (depending on the bin size) and a mosaicity of  $0.2^\circ$  further decreases the detectable

Bin Size	Mosaicities [°]			
	0.4	0.3	0.2	0.1
5.0 keV	0.090 ± 0.008	0.084 ± 0.008 - 7.07 %	0.076 ± 0.007 - 17.78 %	0.065 ± 0.006 - 38.97 %
7.5 keV	0.097 ± 0.009	0.089 ± 0.008 - 9.02 %	0.079 ± 0.007 - 23.03 %	0.065 ± 0.006 - 49.70 %
10.0 keV	0.101 ± 0.009	0.092 ± 0.008 - 10.35 %	0.080 ± 0.007 - 25.94 %	0.066 ± 0.006 - 53.79 %
12.5 keV	0.104 ± 0.009	0.094 ± 0.008 - 10.98 %	0.082 ± 0.007 - 27.01 %	0.067 ± 0.006 - 54.83 %
15.0 keV	0.106 ± 0.010	0.095 ± 0.009 - 11.11 %	0.083 ± 0.008 - 27.11 %	0.069 ± 0.006 - 54.63 %
17.5 keV	0.109 ± 0.010	0.098 ± 0.009 - 11.15 %	0.086 ± 0.008 - 27.09 %	0.071 ± 0.006 - 54.34 %
20.0 keV	0.111 ± 0.010	0.100 ± 0.010 - 11.17 %	0.087 ± 0.008 - 27.05 %	0.072 ± 0.006 - 54.10 %
30.0 keV	0.119 ± 0.011	0.107 ± 0.010 - 11.20 %	0.094 ± 0.008 - 27.16 %	0.077 ± 0.007 - 53.86 %
40.0 keV	0.124 ± 0.011	0.112 ± 0.010 - 11.07 %	0.098 ± 0.009 - 26.90 %	0.081 ± 0.007 - 53.96 %
50.0 keV	0.127 ± 0.011	0.115 ± 0.010 - 10.52 %	0.102 ± 0.009 - 25.05 %	0.085 ± 0.008 - 49.41 %
100.0 keV	0.141 ± 0.013	0.128 ± 0.012 - 9.86 %	0.115 ± 0.010 - 22.95 %	0.098 ± 0.009 - 43.77 %

**Table 11.3:** Lower detection limits for fulfilling an  $SNR \geq 5$  for crystal mosaicities  $0.4^\circ$ ,  $0.3^\circ$ ,  $0.2^\circ$ ,  $0.1^\circ$  and a detector size of  $9000 \text{ mm}^2$  (with/without HOPG). The percentage in the respective second row indicates the relative decrease of the detectable minimum iodine concentration compared to the CdTe detector (1st column).

---

iodine concentration by 18 - 27 %. An HOPG/HAPG crystal with a mosaic spread of  $0.1^\circ$  can detect an iodine concentration about 39 - 55 % (depending on binning) lower than with a  $0.4^\circ$  crystal.



## Part IV

### Summary and conclusion





## Summary

This chapter summarises the motivation and the objective of this thesis, the main developments done in the scope of this thesis and the most important results.

Diagnostic imaging based on X-ray fluorescence (XRF) is a suitable non-invasive technique with functional and molecular imaging capability. It is of great interest in pre-clinical research due to its high sensitivity and its potential to produce tomographic images, providing morphological and molecular information with superior spatial resolution. However, in order to transfer this method to clinical practice it is crucial to address the remaining drawbacks: i) XRF images are produced at the expense of unacceptably large irradiation times, which lead to high radiation doses and/or large concentrations of contrast agents. The reason for this is that XRF detection devices that are able to meet the high demands on sensitivity, efficiency, and energy resolution, exhibit the smallest sensitive areas of all common X-ray detection systems. The substantial loss of the isotropically emitted XRF signal demands large recording times in order to compensate for reduced counting statistics. ii) XRF spectra suffer from a large amount of spurious background counts, mainly due to Compton scattering, which increasingly impairs the XRF signal yield with increasing phantom sizes. Reducing the fraction of contaminating background counts either requires monochromatic initial X-radiation or an advanced energy-selecting filtering scheme.

In this work the above-mentioned challenges were addressed by investigating large area detectors with decreased intrinsic energy resolution and large bin sizes together with energy-selective mosaic HOPG/HAPG crystals with respect to their feasibility for XRF imaging.

- A proof-of-concept XRF imaging setup was developed and experimentally realised at HMGU. The setup comprised an industrial polychromatic X-ray source, a  $50 \times 50 \times 2 \text{ mm}^3$  HOPG crystal with  $0.4^\circ$  mosaicity, and a small area semiconductor CdTe detector with superior energy resolution of 0.48 keV in the EROI. A simple Eppendorf test tube and a mouse sized PMMA phantom were used for all XRF measurement series with various iodine concentrations. A third PMMA phantom of 10 cm in diameter was used for additional investigations concerning the angular background scatter distribution. The experimental setup was characterised by X-ray dose measurements (air kerma) of the used initial X-ray spectra with two ionisation chambers.
- A spectrum correction method for experimentally derived XRF spectra with the CdTe detector was developed including a *stripping algorithm*, which is indis-

pensable for cleansing the raw data from spurious escape signals and secondary detector effects. This algorithm needs to be applied prior to comparing the experimentally derived results to the Monte Carlo simulations.

- A powerful Monte Carlo code for XRF imaging was built based on the software toolkit **GEANT4**, in order to reproduce the results of the XRF experiments. Since **GEANT4** version 10.00 has no routine for implementing mosaic crystals, an additional *Mosaicity and Resolution* algorithm was implemented in C++. This post-processing code adds the effect of the HOPG/HAPG crystal with arbitrary mosaicities. Moreover, it supplies the resulting XRF spectrum with a realistic intrinsic detector resolution.
- In order to validate the developed Monte Carlo XRF code, it was used to simulate the findings of the experiments. The simulated results are in accordance with the experimentally derived results in that both energy spectra exhibit the same shape and intensity and similarly show the 50 % reduction of the HOPG crystal. However, as opposed to the simulated results, the experimentally derived spectra comprise notable contributions at energy regions below 15 keV. This discrepancy originates from the detector characteristics, which can only be resolved by a suitable stripping algorithm, which however itself exhibits various approximations. Experimentally derived XRF spectra emitted from a mouse-sized PMMA phantom with an iodine concentration of 5.0 mg/ml and recorded with a CdTe detector with  $\approx 0.48$  keV energy resolution in the EROI and a binning of  $\approx 86$  keV, yield an SNR of  $9.81 \pm 2.11$  and  $8.28 \pm 2.12$  for a setup without/with HOPG crystal, respectively. The simulated SNRs are slightly larger with  $12.49 \pm 0.94$  for a non-HOPG configuration and  $9.49 \pm 0.99$  for a setup including the crystal.
- A comprehensive analysis scrutinising the feasibility of large area detectors with decreased intrinsic energy resolution and large bin sizes together with energy-selective HOPG/HAPG crystals was performed using the developed Monte Carlo XRF code. The subjects of investigation were various detector sizes up to 3000 times the size of the CdTe detector and bin sizes ranging from 5 keV to 100 keV ( $\hat{=}$  *no binning*). For a detector size of 9000 mm<sup>2</sup> and an iodine concentration of 1.0 mg/ml, it has been shown that for binnings  $\geq 15$  keV implementing an HOPG crystal with 0.4° mosaicity leads to improved results in terms of SNR and minimum detectable iodine concentration (based on the Rose criterion). At a binning of 15 keV the SNR yield was increased by 7.2 % compared to the non-HOPG setup. For a detector with a binning of 100 keV the crystal improved the SNR by 71.3 %.
- Further simulations were performed investigating the influence of intrinsic detector resolution and mosaicity. Energy resolutions up to 2.4 keV ( $5 \times$  CdTe) in the EROI, and the crystal mosaicities 0.3°, 0.2° and 0.1° were implemented and tested in terms of SNR and minimal detectable iodine concentration. With decreasing intrinsic detector resolutions, the benefit of the HOPG decreases for small bin sizes. However, for a detector size of 9000 mm<sup>2</sup>, an iodine concentration of 1.0 mg/ml, and an energy resolution of 2.4 keV, the implementation of

the HOPG is still beneficial for energy bin sizes larger than 20 keV. Small mosaicities considerably improve the SNR: Compared to a crystal with a mosaicity of  $0.4^\circ$ , a mosaicity of  $0.1^\circ$  improves the SNR by 43.8 % for an intrinsic detector resolution of 0.48 keV and a binning of 100 keV. Implementing HOPG/HAPG crystals with reasonable mosaic spread thus compensates for decreased intrinsic energy resolutions.

## Conclusion and outlook

Large scan times and reduced counting statistics resulting in the need for high X-radiation doses are the main obstacles in XRF imaging research. Increasing the sensitive area of the implemented detection system could solve these challenges while maintaining a high detection sensitivity and superior spatial resolution. However, the detector size generally correlates with a reduced intrinsic energy resolution and a coarse binning, impairing the specificity of the imaging method and leading to a decrease in sensitivity. This work has shown that large area detectors nevertheless have the potential to be implemented in XRF measurements when supported by suitable energy-selecting filtering schemes comprising mosaic crystals. One of the main results is that in particular for large bin sizes, the HOPG crystal yields results that outperform those obtained with imaging setups omitting it. Suitable combinations of intrinsic detector resolution and the lowest reasonable crystal mosaicity further enhance the SNR yield and thus allow for the use of even lower iodine concentrations. Also, this imaging concept exploits the reciprocity between applied X-ray dose and detector area, which verifiably resolves the problem of relatively large doses needed for other existing XRF imaging setups operating with polychromatic X-rays. In addition, the challenge of large scan times and statistically insufficient XRF spectra could be resolved. However, a detector with these characteristics produces spectra with XRF signals that are hardly distinguishable from the continuous background. This work used a workaround by running a set of two simulations, one with contrast agent and one without contrast agent. Via subtraction, the background distribution could be separated from the XRF signal. For the work with more elaborate phantoms and in preclinical animal research, this workaround will not suffice due to two main reasons: First of all, especially in the context of *in vivo* imaging, two successive scans will double the dose applied to the animal/patient. Second, the animal/patient can move between two scans such that the images are no longer comparable. This is why the success of this approach depends on research dealing with tomographic reconstruction methods. Considerable advances in reconstruction techniques have the potential to reconstruct the background distribution from the tomographic absorption image. If they are recorded simultaneously to the XRF images, animal/patient movement would not play a role and no additional radiation dose would be applied to the animal/patient. Yet, currently developed algorithms do not meet these demands. Apart from these obstacles, several steps have to be taken in order to further advance the research in XRF imaging together with large area detectors and push this approach towards clinical practice. Based on the experience obtained in the framework of this thesis, four such steps can be identified:

i) The simulated findings of this work need experimental validation by performing measurements with a large area detector together with a fan construction consisting of a radially aligned array of HOPG and collimator leaves (cp. figure S.1). This construction reduces non-radially directed multiple Compton photons and forces isotropically emitted X-rays to hit the HOPG crystal at the Bragg angle ( $3.7^\circ$ ) of the  $K_\alpha$  emission line of iodine (28.6 keV). Preliminary experiences with a 2000 mm<sup>2</sup> NaI(Tl) scintillator (not included in this thesis) have shown that the relative alignment of the crystal leaves places high demands on precision. This construction is nevertheless necessary for large area detectors in order to force all XRF photons to interact with the energy-selecting HOPG material prior to hitting the detection area.

ii) Another important experimental validation comprises the investigations of various crystal mosaicities and thicknesses. This work has shown that the SNRs of the resulting XRF spectra considerably improve with decreasing crystal mosaicity. However, an experimental validation using various mosaicities and crystal samples from different manufacturers is necessary to capture the uncertainties due to the differing fabrication steps and to develop an improved universal model for simulating crystal mosaicities. This thesis did not consider the influence of the crystal thickness. According to theory, the broadening of the reflection curve caused by attenuation and screening effects (primary and secondary extinction) should reduce with decreasing crystal thickness and thus reduce the bandwidth of the reflection curve and improve the SNR for larger bin sizes. Another positive consequence is that with a reduced crystal thickness, the above-mentioned vertical alignment of crystal leaves would leave enough space between the leaves such that a larger effective detection area could be used. Nevertheless, it has to be noted that the crystal thickness and the thickness of the collimator material are also limited by their absorption capabilities since transmitting X-rays could directly hit the sensitive area of the detector.

iii) The above findings need to be translated to tomographic imaging in order to combine molecular image information from XFCT, with geometric features of absorption based CT. This will require two separate reconstruction codes, one for the absorption image including the reconstruction of the background distribution, and the second for the XRF contributions. Considering this large amount of data and subsequent reconstruction effort, a reduced amount of bins turns out to be beneficial, especially when the imaging system will be expanded towards larger human-sized objects and more elaborate phantoms.

iv) The final step for translating the proposed imaging setup into clinical practice is to implement a contrast agent with a high atomic number  $Z$  in the form of NPs, which enables functionalisation. As has been expounded in the introduction of this thesis, gold, in particular AuNPs, is a suitable and an extensively investigated candidate for XRF imaging with human sized objects. However, the implementation of materials with even higher atomic numbers than iodine introduces new challenges related to the HOPG crystal: The Bragg angle of the characteristic  $K_\alpha$  emission line of gold is  $1.55^\circ$  (less than half of the angle for iodine) for an optimal reflection, thus tremendously increasing the precision demands on the crystal fan construction. Also, the crystal leaves of the fan construction need to be aligned even closer to each other (vertically) to prevent XRF photons from hitting the detector sensitive area without having been

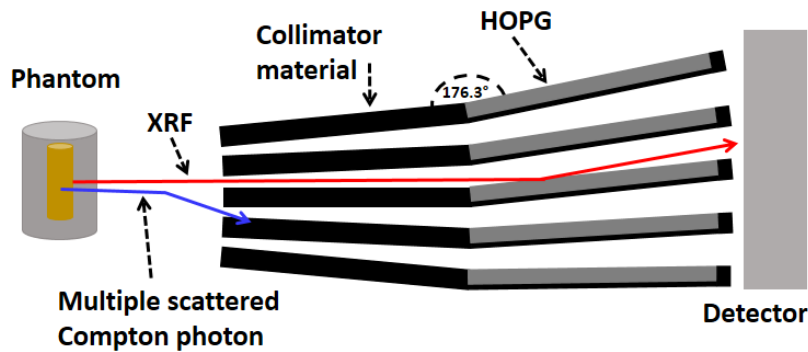


**Figure S.1:** Proposed scheme of an energy-analysing HOPG crystal fan construction as an application for large area detectors. Multiple scattered photons are blocked by the radially aligned collimator, whereas isotropically directed photons (including XRF photons) proceed to the HOPG leaves where they are selected according to their energy value before hitting the detector's sensitive area.

processed by the HOPG crystal. Moreover, implementing gold as a contrast agent considerably increases the problem of transmitting X-rays since an incident X-ray spectrum with a centroid preferably above the K-edge of gold (80.7 keV; the K-edge of iodine is 33.2 keV) is required in order to induce excitation. As a consequence, the crystal leave thickness, comprising HOPG and collimator material, needs to be increased, which additionally reduces the amount of usable sensitive detection area. Another challenge is that the reflection curve has a bandwidth of about 20.0 keV (FWHM), 4 times wider than that for iodine. Also, the reflection intensity of only roughly 24% in the EROI (at  $\approx 67.0$  keV) for the  $K_{\alpha}$  emission line of gold, results in a reduced number of counts in the EROI. Consequently the SNR is expected to be significantly reduced compared to the non-HOPG implementation due to statistical fluctuations. This prospect emphasises the importance of an intensive study of crystal mosaicity, which would considerably improve the situation for the reflection of gold fluorescence: A mosaicity of  $0.1^{\circ}$  generates a reflection curve with a bandwidth of 6 keV and an intensity of about 45% in the EROI of the emission line of gold.

Despite the remaining challenges it is worthwhile to continue the work on XRF imaging with mosaic crystals due to their potential to reduce the still necessary large scan times, which lead to high radiation doses.

# Part V

## APPENDIX





## A. Excerpt of stripping algorithm

```

CDA: # channels  $\mathcal{X}$  corresponding to 23.2 keV,  $\hat{=}$  Cd $_{\alpha}$ 
CDB: # channels  $\mathcal{X}$  corresponding to 26.1 keV,  $\hat{=}$  Cd $_{\beta}$ 
TEA: # channels  $\mathcal{X}$  corresponding to 27.5 keV,  $\hat{=}$  Te $_{\alpha}$ 
TEB: # channels  $\mathcal{X}$  corresponding to 31.0 keV,  $\hat{=}$  Te $_{\beta}$ 

max:  $\hat{=}$  highest photopeak channel  $\mathcal{X}_{\max}$  of spectrum

=====
for (num=0; num<max; ++num)

{
cdalp = 0.025 + exp (-(aa0[max-num]+13)/19); Cd $_{\alpha}$  Polynom for Addition
cdalp2 = 0.025 + exp (-(aa0[max-num+CDA]+13)/19); Cd $_{\alpha}$  Polynom for Subtraction

cdbe = 0.01 + exp (-(aa0[max-num]+46)/20); Cd $_{\beta}$  Polynom for Addition
cdbe2 = 0.01 + exp (-(aa0[max-num+300]+46)/20); Cd $_{\beta}$  Polynom for Subtraction

tealp = 0.011 + exp (-(aa0[max-num]+13)/16); Te $_{\alpha}$  Polynom for Addition
tealp2 = 0.011 + exp (-(aa0[max-num+TEA]+13)/16); Cd $_{\alpha}$  Polynom for Subtraction

tebe = 0.003 + exp (-(aa0[max-num]+50)/20); Te $_{\beta}$  Polynom for Addition
tebe2 = 0.003 + exp (-(aa0[max-num+TEB]+50)/20); Te $_{\beta}$  Polynom for Subtraction

if ((max-num+ CDA)<= max)
{
if ((max-num+ TEB)<= max) Processing Te $_{\beta}$  part
{
Parameters for subtraction
teb_pa = aa1[max-num] - tebe2*aa1[max-num+TEB];
tea_pa = teb_pa - tealp2*aa1[max-num+TEA];
cdb_pa = tea_pa - cdbe2*aa1[max-num+CDB];
cda_pa = cdb_pa - cdalp2*aa1[max-num+CDA];

Parameters for addition
teb_ve = tebe*aa1[max-num];
tea_ve = tealp*aa1[max-num];
cdb_ve = cdbe*aa1[max-num];
cda_ve = cdalp*aa1[max-num];

minus = tebe2*aa1[max-num+TEB] + tealp2*aa1[max-num+TEA]
        + cdbe2*aa1[max-num+CDB] + cdalp2*aa1[max-num+CDA];

if((max-num)>= TEB) Processing energy channels > TEB and < max
{
plus = cdb_ve + cda_ve + tea_ve + teb_ve;
total = cda_pa + cdb_ve + cda_ve + tea_ve + teb_ve;

if(total < 0)
{
total = 0;
}
}
}
else if((max-num)>= TEA) Processing energy channels > TEA and < TEB
{
plus = cdb_ve + cda_ve + tea_ve;
total = cda_pa + cdb_ve + cda_ve + tea_ve;
}
}
}

```

```

        if(total < 0)
        {
            total = 0;
        }
    }
else if((max-num)>= CDB) Processing energy channels > CDB and < TEA
{
    plus = cdb_ve + cda_ve;
    total = cda_pa + cdb_ve + cda_ve;

    if(total < 0)
    {
        total = 0;
    }
}
else if((max-num)>= CDA) Processing energy channels > CDA and < CDB
{
    plus = cda_ve;
    total = cda_pa + cda_ve;

    if(total < 0)
    {
        total = 0;
    }
}
else
{
    plus = 0;
    total = cda_pa;

    if(total < 0)
    {
        total = 0;
    }
}

    out<max-num< «minus« «plus« «total« «aa0[max-num]«endl;
}

else if ((max-num+ TEA)<= max) Processing Teα part
{
    Parameters for subtraction
    tea_pa = aa1[max-num] - tealp2*aa1[max-num+TEA];
    cdb_pa = tea_pa - cdbe2*aa1[max-num+CDB];
    cda_pa = cdb_pa - cdalp2*aa1[max-num+CDA];

    Parameters for addition
    tea_ve = tealp*aa1[max-num];
    cdb_ve = cdbe*aa1[max-num];
    cda_ve = cdalp*aa1[max-num];
    teb_ve = tebe*aa1[max-num];

    minus = tebe2*aa1[max-num+TEB] + tealp2*aa1[max-num+TEA]
            + cdbe2*aa1[max-num+CDB] + cdalp2*aa1[max-num+CDA];

    if((max-num)>= TEB) Processing energy channels > TEB and < max
    {
        plus = cdb_ve + cda_ve + tea_ve + teb_ve;
        total = cda_pa + cdb_ve + cda_ve + tea_ve + teb_ve;

        if(total < 0)
        {
            total = 0;
        }
    }
}
else if((max-num)>= TEA) Processing energy channels > TEA and < TEB
{
    plus = cdb_ve + cda_ve + tea_ve;

```

```

total = cda_pa + cdb_ve + cda_ve + tea_ve;

    if(total < 0)
    {
        total = 0;
    }
}
else if((max-num)>= CDB) Processing energy channels > CDB and < TEA
{
    plus = cdb_ve + cda_ve;
    total = cda_pa + cdb_ve + cda_ve;

    if(total < 0)
    {
        total = 0;
    }
}
else if((max-num)>= CDA) Processing energy channels > CDA and < CDB
{
    plus = cda_ve;
    total = cda_pa + cda_ve;

    if(total < 0)
    {
        total = 0;
    }
}
else
{
    plus = 0;
    total = cda_pa;

    if(total < 0)
    {
        total = 0;
    }
}

    out<max-num< <minus< <plus< <total< <aa0[max-num]<<endl;
}

else if ((max-num+ CDB)<= max) Processing Cdβ part
{
    Parameters for subtraction
    cdb_pa = aa1[max-num] - cdbe2*aa1[max-num+CDB];
    cda_pa = cdb_pa - cdalp2*aa1[max-num+CDA];

    Parameters for addition
    cdb_ve = cdbe*aa1[max-num];
    cda_ve = cdalp*aa1[max-num];
    cdb_ve = cdbe*aa1[max-num];
    teb_ve = tebe*aa1[max-num];

    minus = tebe2*aa1[max-num+TEB] + tealp2*aa1[max-num+TEA]
           + cdbe2*aa1[max-num+CDB] + cdalp2*aa1[max-num+CDA];

    if((max-num)>= TEB) Processing energy channels > TEB and < max
    {
        plus = cdb_ve + cda_ve + tea_ve + teb_ve;
        total = cda_pa + cdb_ve + cda_ve + tea_ve + teb_ve;

        if(total < 0)
        {
            total = 0;
        }
    }
}
else if((max-num)>= TEA) Processing energy channels > TEA and < TEB
{
    plus = cdb_ve + cda_ve + tea_ve;

```

```

total = cda_pa + cdb_ve + cda_ve + tea_ve;

    if(total < 0)
    {
        total = 0;
    }
}
else if((max-num)>= CDB) Processing energy channels > CDB and < TEA
{
    plus = cdb_ve + cda_ve;
    total = cda_pa + cdb_ve + cda_ve;

    if(total < 0)
    {
        total = 0;
    }
}
else if((max-num)>= CDA) Processing energy channels > CDA and < CDB
{
    plus = cda_ve;
    total = cda_pa + cda_ve;

    if(total < 0)
    {
        total = 0;
    }
}
else
{
    plus = 0;
    total = cda_pa;

    if(total < 0)
    {
        total = 0;
    }
}

    out<max-num< <minus< <plus< <total< <aa0[max-num]<endl;
}

else Processing Cdα part
{
    Parameters for subtraction
    cda_pa = aa1[max-num] - cdalp2*aa1[max-num+CDA];

    Parameters for addition
    cda_ve = cdalp*aa1[max-num];
    tea_ve = tealp*aa1[max-num];
    cdb_ve = cdbe*aa1[max-num];
    teb_ve = tebe*aa1[max-num];

    minus = tebe2*aa1[max-num+TEB] + tealp2*aa1[max-num+TEA]
            + cdbe2*aa1[max-num+CDB] + cdalp2*aa1[max-num+CDA];

    if((max-num)>= TEB) Processing energy channels > TEB and < max
    {
        plus = cdb_ve + cda_ve + tea_ve + teb_ve;
        total = cda_pa + cdb_ve + cda_ve + tea_ve + teb_ve;

        if(total < 0)
        {
            total = 0;
        }
    }
    else if((max-num)>= TEA) Processing energy channels > TEA and < TEB
    {
        plus = cdb_ve + cda_ve + tea_ve;
        total = cda_pa + cdb_ve + cda_ve + tea_ve;
    }
}

```



## B. SNRs for 1.0 mg/ml iodine concentration

Bin Size	<i>w/out HOPG</i>	<i>w/ HOPG</i>	% <i>in-/decrease</i>
5.0 keV	95.28 ± 0.18	70.55 ± 0.19	- 35.05 %
7.5 keV	78.72 ± 0.15	63.13 ± 0.17	- 24.70 %
10.0 keV	67.80 ± 0.13	59.95 ± 0.16	- 13.09 %
12.5 keV	58.55 ± 0.11	58.12 ± 0.16	- 0.74 %
15.0 keV	53.25 ± 0.10	57.06 ± 0.16	+ 7.15 %
17.5 keV	48.77 ± 0.10	56.16 ± 0.15	+ 15.15 %
20.0 keV	45.40 ± 0.10	55.41 ± 0.15	+ 22.05 %
30.0 keV	37.01 ± 0.08	53.15 ± 0.15	+ 43.61 %
40.0 keV	32.83 ± 0.07	51.44 ± 0.14	+ 56.69 %
50.0 keV	31.15 ± 0.07	50.01 ± 0.14	+ 60.55 %
100.0 keV	28.09 ± 0.06	48.13 ± 0.13	+ 71.34 %

**Table B.1:** SNRs obtained with an iodine concentration of 1.0 mg/ml and a detector size of 9000 mm<sup>2</sup> (with/without HOPG). The percentage in the third column indicates the relative increase/decrease of the SNR obtained with HOPG compared to the SNR obtained without crystal.

Bin Size	Mosaicities [°]			
	0.4	0.3	0.2	0.1
5.0 keV	70.55 ± 0.19	75.53 ± 0.20 + 7.06 %	83.09 ± 0.20 + 17.77 %	98.05 ± 0.23 + 38.98 %
7.5 keV	63.13 ± 0.17	68.82 ± 0.18 + 9.01 %	77.67 ± 0.19 + 23.03 %	94.51 ± 0.22 + 49.71 %
10.0 keV	59.95 ± 0.16	66.15 ± 0.17 + 10.34 %	75.50 ± 0.19 + 25.94 %	92.19 ± 0.21 + 53.78 %
12.5 keV	58.12 ± 0.16	64.50 ± 0.17 + 10.98 %	73.81 ± 0.18 + 27.00 %	89.99 ± 0.21 + 54.83 %
15.0 keV	57.06 ± 0.16	63.40 ± 0.16 + 11.11 %	72.53 ± 0.18 + 27.11 %	88.24 ± 0.20 + 54.64 %
17.5 keV	56.16 ± 0.15	62.42 ± 0.16 + 11.15 %	71.38 ± 0.18 + 27.10 %	86.69 ± 0.20 + 54.36 %
20.0 keV	55.41 ± 0.15	61.60 ± 0.16 + 11.17 %	70.40 ± 0.17 + 27.05 %	85.38 ± 0.20 + 54.09 %
30.0 keV	53.15 ± 0.15	59.10 ± 0.15 + 11.19 %	67.58 ± 0.17 + 27.15 %	81.78 ± 0.19 + 53.87 %
40.0 keV	51.44 ± 0.14	57.13 ± 0.15 + 11.06 %	65.27 ± 0.16 + 26.89 %	79.19 ± 0.18 + 53.95 %
50.0 keV	50.01 ± 0.14	55.27 ± 0.14 + 10.52 %	62.53 ± 0.16 + 25.03 %	74.72 ± 0.17 + 49.41 %
100.0 keV	48.13 ± 0.13	52.87 ± 0.14 + 9.85 %	59.17 ± 0.15 + 22.94 %	69.19 ± 0.16 + 43.76 %

**Table B.2:** SNRs obtained with an iodine concentration of 1.0 mg/ml for crystal mosaicities 0.4°, 0.3°, 0.2°, 0.1° and a detector size of 9000 mm<sup>2</sup> (with/without HOPG). The percentage in the respective second row indicates the relative increase/decrease of the SNR compared to the CdTe detector (1st column).





# List of figures

1.1	Classification of X-rays within the electromagnetic spectrum. . . . .	12
1.2	Spectra using various acceleration voltages $U_A$ produced by an X-ray tube. . . . .	13
1.3	Basic design of an X-ray tube and scheme of the anode angle. . . . .	14
1.4	Scheme of a radioisotopic X-ray source and spectrum. . . . .	15
1.5	Scheme of a third-generation synchrotron facility and structure of a wiggler/undulator. . . . .	16
2.1	Photon mass attenuation coefficients for water in the energy range between 1 keV and 100 keV. . . . .	20
2.2	Klein-Nishina cross section $\sigma_C$ for photon scattering angles at different incident photon energies $E_\gamma$ . . . . .	21
2.3	Schematic description of the Photoelectric effect (X-ray fluorescence). . . . .	22
2.4	Energy dependence of the mass attenuation coefficient $\mu/\rho$ for iodine. . . . .	23
3.1	Mass attenuation coefficient $\mu/\rho$ for the typical semiconductor detector materials Si, Ge and CdTe. . . . .	26
3.2	Basic scheme of a gas proportional counter. . . . .	31
3.3	Basic scheme of a scintillation detector. . . . .	32
3.4	Basic scheme of a semiconductor detector. . . . .	33
4.1	Example of a monochromatising optic device and energy-selective analyser crystal. . . . .	34
4.2	Schematic description of the process of Bragg diffraction. . . . .	35
4.3	Schematic explanation of mosaic focusing via Bragg reflection. . . . .	37
5.1	Example XRF spectra with fitting functions visualising the removal of the background and the isolation of the XRF signal $\mathcal{S}_{\text{XRF}}$ . . . . .	39
6.1	Top view scheme of the imaging setup for measuring the iodine X-ray fluorescence with and without an energy-selecting HOPG crystal. . . . .	45

6.2	Side view schematic of a basic imaging setup for measuring the iodine X-ray fluorescence with and without implementation of an energy-selecting HOPG crystal. . . . .	46
6.3	Anode focal spot sizes of the used industrial X-ray tube MG 160 (Yxlon) measured on 28.09.2012. . . . .	47
6.4	Example spectra generated with different high voltages and filters. . . . .	48
6.5	Photo of all phantoms used in this work: Eppendorf test tube, PMMA/mouse phantom, large PMMA phantom. . . . .	50
6.6	Photo of the used semiconductor XR-100CdTe X-ray detector . . . . .	51
6.7	Detailed structure and efficiency curve of the used CdTe detector. . . . .	51
6.8	SpekCalc graphical user interface for generating initial X-ray tube spectra. . . . .	54
6.9	Polynomials derived from the ratios between escape peak to photopeak for each escape peak of K-shell electrons of Cadmium and Telluride. . . . .	56
6.10	Illustration of the procedure of the stripping algorithm for a CdTe detector. . . . .	57
6.11	Example of an escape corrected X-ray spectrum including the original spectrum and subtracted parts. . . . .	58
7.1	Recorded XRF spectra with/without HOPG crystal generated with an initial spectrum of 140 keV/(1.0 Al) and an iodine concentration of 5.0 mg/ml. . . . .	60
7.2	SNRs of XRF measurements with/without HOPG crystal produced with various beam qualities with 1.0 mm Al filtration and high voltages from 40 to 160 kV in steps of 20 kV. . . . .	62
7.3	Initial beam qualities and resulting XRF spectra with beam qualities 40 kV/(1.0 mm Al) and 100 kV/N(1.0 mm Al). . . . .	63
7.4	Collection of XRF spectra with/without HOPG crystal recorded with different filter settings and a fixed high voltage of $U_A = 80$ kV. . . . .	65
7.5	Final initial spectrum used for all subsequent XRF measurements of this work. Specifications: $U_A$ 80 kV, $I = 37.5$ mA, 1 mm Al filter. . . . .	66
7.6	Number of counts per angular position of the detector relative to the X-ray source. . . . .	67
7.7	XRF spectra emitted by the PMMA/mouse phantom with/without HOPG crystal. . . . .	69
7.8	SNRs of recorded XRF spectra (with/without HOPG crystal) emitted from the PMMA/mouse phantom, applying various iodine concentrations. . . . .	70
7.9	XRF spectra emitted by the Eppendorf test tube phantom with/without HOPG crystal. . . . .	71

---

7.10	SNRs of recorded XRF spectra (with/without HOPG crystal) emitted from the Eppendorf test tube phantom, applying various iodine concentrations. . . . .	72
8.1	Simplified scheme of the simulated XRF imaging setup visualised with Qt. . . . .	83
9.1	Graphical user interface of X0h with the search form for all crystal planes fulfilling the Bragg condition. . . . .	87
9.2	Reflection pattern of the 002 and 004 plane of the HOPG crystal for a Bragg angle of $3.7^\circ$ . . . . .	88
10.1	Comparison of the simulated and experimental XRF spectra (with/without HOPG crystal) emitted by the PMMA/mouse phantom filled with an iodine concentration of 5.0 mg/ml. . . . .	90
10.2	SNRs of simulated and experimentally recorded XRF spectra (with/without HOPG crystal) emitted from the PMMA/mouse phantom, applying various iodine concentrations. . . . .	92
10.3	Comparison of the simulated and experimental XRF spectra (with/without HOPG crystal) emitted by the Eppendorf test tube phantom filled with an iodine concentration of 5.0 mg/ml. . . . .	93
10.4	SNRs of simulated and experimentally recorded XRF spectra (with/without HOPG crystal) emitted from the Eppendorf test tube phantom, applying various iodine concentrations. . . . .	94
10.5	Simulated XRF spectra with/without HOPG of the PMMA/mouse and Eppendorf test tube phantom filled with an iodine concentration of 5.0 mg/ml . . . . .	95
10.6	Comparison of the simulated background distribution with the measured background for the PMMA/mouse phantom and phantom 3. . . . .	96
11.1	Example spectra and histograms with different bin sizes. . . . .	98
11.2	SNRs of XRF spectra with an iodine concentration of 5.0 mg/ml recorded with various detector sizes. . . . .	99
11.3	SNRs calculated for bin sizes between 5 and 100 keV recorded with a detector size of $9000 \text{ mm}^2$ and various iodine concentrations (without/with HOPG). . . . .	100
11.4	Comparison of the decline of the SNR with bin size for an experimental setup without/with the HOPG crystal and an initial spectrum of $U_A = 80 \text{ kV}$ . . . . .	101
11.5	Comparison of the decline of the SNR with bin size for an experimental setup without/with the HOPG crystal and an initial spectrum of $U_A = 160 \text{ kV}$ . . . . .	102

11.6	Comparison of the decline of the SNR with bin size for various intrinsic detector resolutions with/without HOPG crystal. . . . .	104
11.7	Influence of the crystal mosaicity on the resulting XRF spectra and the decline of the SNR with bin size. . . . .	105
S.1	Proposed scheme of an energy-analysing HOPG crystal fan construction as an application for large area detectors. . . . .	116

# List of tables

2.1	Excerpt of secondary photon labels for the electron transitions between atomic shells. . . . .	22
6.1	All possible filter settings for the industrial X-ray tube MG 160 for generating spectra with various beam qualities. . . . .	48
6.2	The constituents of CdTe, Cadmium and Telluride, with the energies of the K-edges and the characteristic X-ray $K_\alpha$ and $K_\beta$ energies. . . . .	56
7.1	Results of XRF measurements with/without HOPG crystal produced with various beam qualities, a 1.0 mm Al filtration and high voltages from 40 to 160 kV in steps of 20 kV. . . . .	61
7.2	SNRs of recorded XRF spectra (with/without HOPG crystal) recorded with different filter settings and a fixed high voltage of $U_A = 80$ kV. . . . .	64
7.3	Results of XRF measurements with/without HOPG crystal produced with the PMMA/mouse phantom filled with various iodine concentrations. . . . .	68
7.4	Results of XRF measurements with/without HOPG crystal produced with the Eppendorf test tube phantom filled with various iodine concentrations. . . . .	71
7.5	Calibration factors for both ionisation chambers used for calculating the air kerma (Gy). . . . .	73
7.6	Results of the dose measurements with the small (Q16, 0.6 cm <sup>3</sup> ) and the large (Q30, 30 cm <sup>3</sup> ) ionisation chamber. . . . .	74
10.1	SNRs of XRF spectra simulations and measurements (with/without HOPG crystal) produced with the PMMA/mouse phantom, filled with various iodine concentrations. . . . .	91
10.2	SNRs of XRF spectra simulations and measurements (with/without HOPG crystal) produced with the Eppendorf test tube phantom, filled with various iodine concentrations. . . . .	94
11.1	List of investigated sensitive detector areas and bin sizes. . . . .	97
11.2	Lower detection limits for fulfilling an $\text{SNR} \geq 5$ (Rose criterion) for all detector and bin sizes (with/without HOPG). . . . .	103

11.3	Lower detection limits for fulfilling an $\text{SNR} \geq 5$ for various crystal mosaicities $0.4^\circ$ , $0.3^\circ$ , $0.2^\circ$ , $0.1^\circ$ and a detector size of $9000 \text{ mm}^2$ (with/without HOPG). . . . .	106
B.1	SNRs obtained with an iodine concentration of $1.0 \text{ mg/ml}$ and a detector size of $9000 \text{ mm}^2$ (with/without HOPG). . . . .	124
B.2	SNRs obtained with an iodine concentration of $1.0 \text{ mg/ml}$ for various crystal mosaicities $0.4^\circ$ , $0.3^\circ$ , $0.2^\circ$ , $0.1^\circ$ and a detector size of $9000 \text{ mm}^2$ (with/without HOPG). . . . .	125

## List of abbreviations and acronyms

**AuNP** Gold Nano Particle. 2, 117

**CdTe** Cadmium Telluride. iii, v, 26, 33, 45, 50–52, 55–57, 85, 88, 90, 98–100, 104–109, 113–115, 127–129

**CERN** Conseil Européen pour la Recherche Nucléaire (European Council for Nuclear Research). 79, 81

**CPU** Central Processing Unit. 79, 81

**CsI(Tl)** Thallium-doped Cesium Iodide. 31

**CT** Computed Tomography. 1, 2, 117

**ENC** Equivalent Noise Charge. 29

**EROI** Energy Region Of Interest. 62, 65, 66, 97, 98, 101, 104, 113, 114, 118

**EUV** Extreme UltraViolet. 11, 12

**FET** Field-Effect Transistor. 51

**FWHM** Full Width Half Maximum. 3, 27, 35, 47, 48, 50, 51, 88, 104, 118

**GEANT4** GEometry ANd Tracking. iii, v, 5, 59, 68, 77, 79–87, 91, 95, 114

**HAPG** Highly Annealed Pyrolytic Graphite. iii–vi, 3–5, 9, 35, 37, 77, 108, 113–115

**HMGU** Helmholtz Zentrum München GmbH, German Research Center for Environmental Health. 43, 113

**HOPG** Highly Oriented Pyrolytic Graphite. iii–vi, 3–5, 9, 14, 35, 45, 46, 49, 50, 59–72, 77, 85–108, 113–118, 126–128

**IR** InfraRed. 12

**MRI** Magnetic Resonance Imaging. 1

**NaI(Tl)** Thallium-doped Sodium Iodide. 31, 117

- NIST** National Institute of Standards and Technology. 20, 23, 26, 81
- NP** Nano Particle. v, 2, 3, 117
- PBS** Phosphate-Buffered Saline. 49
- PET** Positron Emission Tomography. 1
- PMMA** PolyMethyl MethAcrylate. iii, v, 49, 50, 59, 60, 62, 64, 67–71, 83, 89–92, 95, 96, 98, 99, 101, 102, 106, 113, 114
- PRNG** Pseudo Random Number Generator. 83, 84
- PTW** Physikalisch-Technische Werkstätten, Freiburg Germany. 46
- SNR** Signal to Noise Ratio. 39, 59–64, 66, 69–72, 91, 92, 94, 99–109, 114–118, 126–129
- SPECT** Single Photon Emission Computed Tomography. 1
- UV** UltraViolet. 12
- VIS** Visible Light. 12
- XFCT** X-ray Computed Tomography. 2, 117
- XRF** X-ray fluorescence. iii–vi, 2–5, 9, 11, 14, 15, 17, 19, 22, 24, 34, 38–40, 43, 47, 49, 52, 53, 55, 59–71, 74, 83, 85, 86, 89–92, 94–99, 102, 104, 106, 113, 114, 116–118



# List of symbols

- $DT$  Relative measure of dead time losses [%]. 30, 55
- $E_\gamma$  Initial/primary photon energy [keV]. 18, 20, 21, 24, 27, 28
- $F$  Fano factor. Variance-to-mean ratio of a random process. 28
- $I$  Electric current of the anode [mA]. 13, 47, 54, 61, 66–68, 73, 85, 89, 96, 98, 101
- $K_i$  Air kerma [Gy]. 53, 73, 74
- $M$  Multiplication factor introducing additional broadening to the energy resolution. 29, 30
- $P$  Total irradiated X-ray power [kW]. 13
- $Q$  Electric charge [C]. 24, 52, 53, 73, 74
- $T_D$  Dead time [s]. 30
- $T_L$  Life time [s]. 30
- $T_R$  Real time [s]. 30
- $U_A$  Acceleration/high voltage; positive potential of an X-ray anode [kV]. 11–13, 15, 47, 48, 54, 59–62, 64–68, 73, 85, 89, 96, 98, 101, 102, 131
- $\Delta E$  The energy resolution  $\Delta E$  [keV]. 27–29, 36, 50
- $\Delta\Theta$  Intrinsic width of Bragg reflection. 36, 106
- $\Omega$  Solid angle [sr]. 20, 25, 61, 102
- $\Theta$  Bragg angle [°]. 35, 36
- $\epsilon_c$  Electronic charge conversion factor. 24, 28, 30, 32
- $\eta_{tot}$  Total detection efficiency. Product of various efficiency factors  $\eta_i(E)$ . 25, 55
- $\lambda$  Photon wave length [cm<sup>2</sup>]. 11, 12, 19, 36
- $\mathcal{I}$  X-ray beam intensity. 18, 19
- $\mathcal{X}$  Energy bin. 39, 57, 88

- $\mu/\rho$  Mass attenuation coefficient [ $\text{cm}^2/\text{g}$ ]. 19, 23, 26
- $\nu$  Photon frequency [ $\text{cm}^{-1}$ ]. 11, 12
- $\sigma$  Standard deviation of a distribution. 27, 28, 38–40, 88
- $\sigma_{tot}$  Total cross section [ $\text{cm}^2$ ]. Summation of partial cross sections  $\sigma_i$ . 18
- $c$  Speed of light in vacuum:  $c = 2.998 \cdot 10^8$  m/s. 11
- $e$  Elementary/Electron charge  $e = 1.602 \cdot 10^{-19}$  C. 12
- $h$  Planck's constant:  $h = 6.626 \cdot 10^{-34}$  Js. 11
- $K_\alpha$  X-ray fluorescence line emitted from the L-shell electron filling the K-shell vacancy [keV]. iii, v, 3, 22, 38, 48, 56, 61, 69, 86, 91, 99, 117, 118
- $K_\beta$  X-ray fluorescence line emitted from the M-shell electron filling the K-shell vacancy [keV]. 22, 48, 56, 57, 61, 70, 71, 92, 98, 99
- $Z$  Atomic Number. 2, 13, 18, 19, 21–23, 26, 33, 50, 117

# Bibliography

- [1] Kagadis, G.C. et al., *In vivo small animal imaging: current status and future prospects*, Med. Phys., 37(12), 6421-42 (2010).
- [2] Weissleder, R. and Nahrendorf, M. *Advancing biomedical imaging*, Proc. Natl. Acad. Sci., 112(47), 14424-8 (2015).
- [3] Massoud, T.F. and Gambhir, S.S., *Molecular imaging in living subjects seeing fundamental biological processes in a new light*, Genes Dev., 17(5), 545-80 (2003).
- [4] Schlegel, W., Karger, C., Jäkel, O., [*Medizinische Physik*], Springer Spektrum, Berlin, Heidelberg, 341-364 (2018).
- [5] Mezzanotte, L. et al., *In vivo molecular bioluminescence imaging new tools and applications* Trends Biotechnol., 35(7), 640-52 (2017).
- [6] Hong, G., Antaris, A.L., and Dai, H., *Near-infrared fluorophores for biomedical imaging*, Nat. Biom. Eng., 1, 1-21 (2017).
- [7] Lundström, U. et al., *X-ray phase-contrast CO<sub>2</sub> angiography for sub-10  $\mu$ m vessel imaging*, Phys. Med. Biol., 57(22), 7431-41 (2012).
- [8] Schlomka, J.P. et al., *Experimental feasibility of multi-energy photon-counting K-edge imaging in preclinical computed tomography*, Phys. Med. Biol., 53(15), 4031 (2008).
- [9] Müllner, M. et al., *Feasibility of spectral CT imaging for the detection of liver lesions with gold-based contrast agents - A simulation study*, Physica Medica, 31(8), 875-881 (2015).
- [10] Shilo, M. et al., *Nanoparticles as computed tomography contrast agents: current status and future perspectives*, Nanomedicine, 7(2), 257-69 (2012).
- [11] Daniel, M.-C., Astruc, D., *Gold nanoparticles: Assembly, supramolecular chemistry, quantum-size-related properties, and applications toward biology, catalysis, and nanotechnology*, Chem. Rev., 104(1), 293-346 (2004).
- [12] Connor, E.E. et al., *Gold nanoparticles are taken up by human cells but do not cause acute cytotoxicity*, Small, 1(3), 325-27 (2005).
- [13] Hainfeld, J.F. et al., *Gold nanoparticles: A new x-ray contrast agent*, Br. J. Radiol., 79(939), 248-53 (2006).

- [14] Kim, D. et al., *Antibiofouling polymer-coated gold nanoparticles as a contrast agent for in vivo x-ray computed tomography imaging*, J. Am. Chem. Soc., 129(24), 7661-5 (2007).
- [15] Popovtzer, R. et al., *Targeted gold nanoparticles enable molecular CT imaging of cancer*, Nano Letters, 8(12), 4593-6 (2008).
- [16] Hainfeld, J.F. et al., *Micro-CT enables microlocalisation and quantification of Her2-targeted gold nanoparticles within tumour regions.*, Br. J. Radiol., 84(1002), 526-33 (2010).
- [17] Boisseau, P. and Grodzins, L., *Fluorescence tomography using synchrotron radiation at the NSLS*, Hyperfine Interactions, 33(1), 283-92 (1987).
- [18] Cesareo, R., and Mascarenhas, S., *A new tomographic device based on the detection of fluorescent x-rays*, Nucl. Instrum. Methods Phys. Res., 277(2), 669-72 (1989).
- [19] Ahmad, M. et al., *X-ray luminescence and x-ray fluorescence computed tomography: New molecular imaging modalities*, IEEE Access., 2, 1051-61 (2014).
- [20] Rizk, S.L. and Skypeck, H.H., *Comparison between concentrations of trace-elements in normal and neoplastic human-breast tissue*, Cancer Res., 44(11), 5390-4 (1984).
- [21] Geraki, K., Farquharson, M.J., and Bradley, D.A., *Concentrations of Fe, Cu and Zn in breast tissue: A synchrotron XRF study*, Phys. Med. Biol., 47(13), 2327-39 (2002).
- [22] Geraki, K., Farquharson, M.J., and Bradley, D.A., *X-ray fluorescence and energy dispersive x-ray diffraction for the quantification of elemental concentrations in breast tissue*, Phys. Med. Biol., 49(1), 99-110 (2004).
- [23] Cheong, S.-K. et al., *X-ray fluorescence computed tomography (XFCT) imaging of gold nanoparticle-loaded objects using 110 kVp X-rays*, Phys. Med. Biol., 55(3), 647-62 (2010).
- [24] Jones, B.L. et al., *Experimental demonstration of benchtop x-ray fluorescence computed tomography (XFCT) of gold nanoparticle-loaded objects using lead-and tin-filtered polychromatic cone-beams*, Phys. Med. Biol., 57(23), 457-67 (2012).
- [25] Bazalova, M. et al., *Investigation of x-ray fluorescence computed tomography (XFCT) and K-edge imaging*, IEEE Trans. Med. Imag., 31(8), 1620-7 (2012).
- [26] Cong, W. et al., *X-ray fluorescence tomographic system design and image reconstruction*, J. X-ray Sci. Technol., 21(1), 1-8 (2013).
- [27] Di, W. et al., *A method of measuring gold nanoparticle concentrations by x-ray fluorescence for biomedical applications*, Med. Phys., 40(5), 051901 (2013).
- [28] Ren, W. et al., *Three-dimensional x-ray fluorescence mapping of a gold nanoparticle-loaded phantom*, Med. Phys., 41(3), 031902 (2014).

- [29] Hertz, H.M. et al., *Laboratory x-ray fluorescence tomography for high-resolution nanoparticle bio-imaging*, Opt. Lett., 39(9), 2790-3 (2014).
- [30] Ahmad, M. et al., *Optimized detector angular configuration increases the sensitivity of x-ray fluorescence computed tomography (XFCT)*, IEEE Trans. Med. Imag., 34(5), 1140-7 (2015).
- [31] Grüner, F. et al., *Localising functionalised gold-nanoparticles in murine spinal cords by X-ray fluorescence imaging and background-reduction through spatial filtering for human-sized objects*, Sci. Rep. 8, 16561 (2018).
- [32] Manohar, N. et al., *Quantitative imaging of gold nanoparticle distribution in a tumor-bearing mouse using benchtop x-ray fluorescence computed tomography*, Sci. Rep., 6, 22079 (2016).
- [33] Larsson, L.C. et al., *High-spatial-resolution x-ray fluorescence tomography with spectrally matched nanoparticles*, Phys. Med. Biol., 63(16), 164001 (2018).
- [34] Bazalova, M. et al., *L-shell x-ray fluorescence computed tomography (XFCT) imaging of cisplatin*, Phys. Med. Biol., 59(1), 219-32 (2014).
- [35] Karanfil, C. et al., *A bent Laue analyzer detection system for dilute fluorescence XAFS*, AIP Proc., 521(1), 178-82 (2000).
- [36] Moore, A.W., [*Chemistry and Physics of Carbon Vol. II*], Marcel Dekker, New York, 69-187 (1973).
- [37] Zachariasen, W.H., [*Theory of X-Ray Diffraction in Crystals*], Dover, Meneola N.Y., 159-75 (1945).
- [38] Müller, B.H. et al., *Molecular imaging based on x-ray fluorescent high Z-tracers*, Phys. Med. Biol., 58(22), 8063-76 (2013).
- [39] Müller, B.H. et al., *X-ray fluorescence molecular imaging of high-Z tracers: investigation of a novel analyzer based setup*, Proc. SPIE, 90331J (2014).
- [40] Beckhoff, B. et al., [*Handbook of Practical X-Ray Fluorescence Analysis*], Springer-Verlag, Berlin Heidelberg, (2006).
- [41] Röntgen, W.C., *Ueber eine neue Art von Strahlen*, Annalen der Physik und Chemie, Neue Folge, 64, (1898).
- [42] Duane, W. and Hunt, F.L., *On X-Ray Wave-Lengths*, Physical Review., 6(2), 166-72 (1915).
- [43] Bertin, E.P., [*Principles and Practice of X-ray Spectrometric Analysis*], Plenum Press, New York, 1079 (1975).
- [44] Van Grieken, R.E. and Markowicz A., [*Handbook of X-ray Spectrometry*], Marcel Dekker Inc, New York, 983 (2002).

- [45] Wehnelt, A., *Über den Austritt negativer Ionen aus glühenden Metallverbindungen und damit zusammenhängende Erscheinungen*, Ann. Phys., 4(14), 425-68 (1904).
- [46] Krieger, H., [*Grundlagen der Strahlenphysik und des Strahlenschutzes, 3. Auflage*], Vieweg+Teubner, Wiesbaden, 158-204 (2009).
- [47] Tavernier, S., [*Experimental Techniques in Nuclear and Particle Physics*], Springer-Verlag, Berlin Heidelberg, 1-40 (2010).
- [48] Auger, P., *Sur l'effet photoélectrique composé*, J. Phys. Radium, 6(6), 205-208 (1925).
- [49] Meitner, L. Z., *Über die  $\beta$ -Strahl-Spektren und ihren Zusammenhang mit der  $\gamma$ -Strahlung*, Zeitschrift für Physik, 11(1), 35-54 (1922).
- [50] Fano, U., *Ionization Yield of Radiations. II. The Fluctuations of the Number of Ions*, Physical Review., 72(1), 26 (1947).
- [51] Gedecke, D.A., *ORTEC Application Note AN63, Simply Managing Dead Time Errors in Gamma-Ray Spectroscopy*, www.ortec-online.com (2003).
- [52] Leo, W.R., [*Techniques for Nuclear and Particle Physics Experiments*], Springer-Verlag Berlin Heidelberg, 122-127 (1994).
- [53] Klein, O. and Nishina, Y., *Über die Streuung von Strahlung durch freie Elektronen nach der neuen relativistischen Quantenmechanik nach Dirac*, Zeitschrift für Physik, 52, 853-68 (1929).
- [54] Redus, B., *Charge Trapping in XR-100T-CdTe and -CZT Detectors*, Application Note ANCZT-2 Rev., 3 (2007).
- [55] Beckhoff, B., Kanngiesser, B., and Malzer, W., *New broadband filtering device with rectangular efficiency shape based on x-ray focusing by strongly curved HOPG crystals*, Proc. SPIE, 2859 (1996).
- [56] Legall, H. et al., *High spectral resolution x-ray optics with highly oriented pyrolytic graphite*, Opt. Expr. 14(10), 4570-6 (2006).
- [57] Legall, H. et al., *A new generation of X-ray optics based on pyrolytic graphite*, Proceedings of FEL, FRAAU04, 798-801 (2006).
- [58] Freund, A.K., Munkholm, A., and Brennan, S., *X-ray diffraction properties of highly oriented pyrolytic graphite*, Proc. of SPIE, 2856, 68 (1996).
- [59] Legall, H. et al., *An efficient X-ray spectrometer based on thin mosaic crystal films and its application in various fields of X-ray spectroscopy*, J. Appl. Cryst., 42(4), 572-9 (2009).
- [60] Bragg, W.H. and Bragg, W.L., *The Reflexion of X-rays by Crystals*, Proc. R. Soc. Lond. A. 88(605), 428-38 (1913).

- [61] Cowley, J.M., [*Diffraction Physics, 3rd Edition*], Elsevier Science B.V., Amsterdam, 3-24 (1995).
- [62] Sanchez del Rio, M. et al., *Focusing properties of mosaic crystals*, Proc. SPIE, 3448, 246-55 (1998).
- [63] Ice, G.E. and Sparks C.J., *Mosaic crystal x-ray spectrometer to resolve inelastic background from anomalous scattering experiments*, Nucl. Instrum. Methods Phys. Res., 291(1), 110-6 (1990).
- [64] Rose, A., *Vision - Human and Electronics*, Plenum, New York (1973).
- [65] Sanchez del Rio, M. and Dejus, R.J., *Status of XOP: an x-ray optics software toolkit*, Proc. SPIE, 5536, 171-4 (2004).
- [66] Khusainov, A.K., *Cadmium telluride detectors with thermoelectric cooling*, Nucl. Instrum. Methods Phys. Res. A, 322(3), 335-40 (1992).
- [67] Miyajima, S., *Thin CdTe detector in diagnostic x-ray spectroscopy*, Med. Phys., 30(5), 771-7 (2003).
- [68] Matsumoto, C. et al., *Performance of a new Schottky CdTe detector for hard x-ray spectroscopy*, IEEE Trans. Nucl. Sci., 45(3), 428-32 (1998).
- [69] Takahashi, T. et al., *High-resolution Schottky CdTe diode for hard x-ray and gamma-ray astronomy*, Nucl. Instrum. Methods Phys. Res. A, 436(1-2), 111-9 (1999).
- [70] Redus, B., *CdTe Measurement of X-Ray Tube Spectra: Escape Events*, Application Note ANCDTE1 Rev. 1 (2008).
- [71] Redus, B., *Efficiency and Attenuation in CdTe Detectors*, Application Note AN-CdTe-001 (2010).
- [72] Büermann, L., *Calibration Certificate*, S/N 513 PTB 60035-13 (2013).
- [73] Büermann, L., *Calibration Certificate*, S/N 259, PTB 60037-13 (2013).
- [74] Poludniowski, G.G. et al., *SpekCalc: a program to calculate photon spectra from tungsten anode x-ray tubes*, Phys. Med. Biol., 54(19), N433-8 (2009).
- [75] Birch, R. and Marshall, M., *Computation of bremsstrahlung x-ray spectra and comparison with spectra measured with a Ge(Li) detector* Phys. Med. Biol., 24(3), 505-17 (1979).
- [76] Poludniowski, G.G. and Evans, P.M., *Calculation of x-ray spectra emerging from an x-ray tube. Part I. Electron penetration characteristics in x-ray targets*, Med. Phys., 34(6), 2164-74 (2007).
- [77] Poludniowski, G.G., *Calculation of x-ray spectra emerging from an x-ray tube. Part II. X-ray production and filtration in x-ray targets*, Med. Phys., 34(6), 2175-86 (2007).

- [78] Seelentag, W.W. and Panzer, W., *Stripping of x-ray bremsstrahlung spectra up to 300kVp on a desk type computer*, Phys. Med. Biol., 24(4), 767-80 (1979).
- [79] Redus, R. et al., *Characterization of CDTE detectors for quantitative X-ray spectroscopy*, IEEE Trans. Nuclear Sci., 56(4), 2524-32 (2009).
- [80] Tomal, A., Cunha, D.M., and Poletti, M.E., *Comparison of beam quality parameters computed from mammographic X-ray spectra measured with different high-resolution semiconductor detectors*, Radiat. Phys. Chem., 95, 217-20 (2014).
- [81] Tomal, A., Cunha, D.M., and Poletti, M.E., *Establishment of the mammographic radiation qualities in industrial equipment: spectra determination*, Nuclear Instruments and Methods A, 652(1), 883-7 (2011).
- [82] Tomal, A. et al., *Response functions of Si(Li), SDD and CdTe detectors for mammographic x-ray spectroscopy*, Appl. Radiat. Isot., 70(7), 1355-9 (2012).
- [83] Agostinelli, S. et al., *Geant4: A simulation toolkit*, Nucl. Instrum. Meth. A, 506(3), 250-303 (2003).
- [84] Allison, J. et al., *Geant4 Developments and Applications*, IEEE Trans. Nucl. Sci., 53(1), 270-8 (2006).
- [85] Allison, J. et al., *Recent developments in Geant4*, Nucl. Instrum. Meth. A, 835(1), 186-225 (2016).
- [86] *GEANT - Detector Description and Simulation Tool*, CERN Program Library Long Write-up W5013, CERN Geneva, (1993).
- [87] Backus, J., *The History of Fortran I, II, and III*, IEEE Ann. Hist.Comput., 20(4), 68-78 (1998).
- [88] Stroustrup, B., [*The C++ Programming Language*], Addison-Wesley Longman Publishing Co., Inc., Boston, MA, USA, 3rd edition (2000).
- [89] Cosmo, G., *Software process in Geant4*, Proc. Computing in High Energy and Nuclear Physics, Beijing, China, 469-72 (2001).
- [90] GEANT4 Collaboration, *GEANT4 Physics Reference Manual*, Version 10.0, (2013).  
<https://geant4-userdoc.web.cern.ch/UsersGuides/PhysicsReferenceManual/BackupVersions/V10.0/fo/PhysicsReferenceManual.pdf>
- [91] GEANT4 Collaboration, *GEANT4 User's Guide: For Application Developers*, Version 10.0, (2013).  
<https://geant4-userdoc.web.cern.ch/UsersGuides/ForApplicationDeveloper/BackupVersions/V10.0/html/index.html>
- [92] Linstrom, P.J. and Mallard, W.G., *NIST Chemistry WebBook, NIST Standard Reference Database Number 69, National Institute of Standards and Technology, Gaithersburg MD, 20899*, (retrieved September 8, 2018).



- [93] Ivantchenko, V. et al., *Recent improvements in geant4 electromagnetic physics models and interfaces*, Progress in NUCLEAR SCIENCE and TECHNOLOGY, 2, 898-903 (2011).
- [94] Apostolakis, J. et al., *Geometry and physics of the geant4 toolkit for high and medium energy applications*, Radiation Physics and Chemistry, 78(10), 859-73 (2009).
- [95] Seltzer, S.M., Perkins, S.T., and Cullen, D.E., *Tables and graphs of electron-interaction cross-sections from 10 ev to 100 gev derived from the lnl evaluated electron data library (eedl), z=1-100*, Technical Report UCRL-50400, 31, Lawrence Livermore National Laboratory (1989).
- [96] Kissel, L., Cullen, D., and Hubbell, J.H., *Epdl97: the evaluated photon data library*, 1997 version. UCRL-50400, 6(5) (1989).
- [97] Perkins, S.T. et al., *Tables and graphs of atomic subshell and relaxation data derived from the lnl evaluated atomic data library (eadl), z=1-100*, Technical Report UCRL-50400, 30 (1991).
- [98] Scofield, J.H., *Radiative Transitions*, in: [Atomic Inner-Shell Processes], Ed. B.Crasemann, Academic Press, New York (1975).
- [99] OpenGL: [www.opengl.org](http://www.opengl.org)
- [100] Qt: [www.qt.io](http://www.qt.io)
- [101] Barker, E. and Kelsey, J., *Recommendation for Random Number Generation Using Deterministic Random Bit Generators*, NIST Special Publication 800-90A (2012).
- [102] James, F., *A review of pseudorandom number generators*, Comput. Phys. Comm. 60(3), 329-44 (1990).
- [103] Lönnblad, L., *CLHEP: a project for designing a C++ class library for high energy physics*, Comput. Phys. Commun. 84(1-3), 307-16 (1994).
- [104] Message Passing Forum, *MPI: A Message-Passing Interface Standard*, Technical report, Knoxville, TN, USA, (1994).
- [105] Gabriel, E. et al., *Open MPI: Goals, Concept, and Design of a Next Generation MPI Implementation*, In Proceedings, 11th European PVM/MPI Users' Group Meeting, Budapest, (2004).
- [106] Sanchez del Rio, M. and Dejus, R.J., *Status of XOP: v2.4: recent developments of the x-ray optics software toolkit* Proc. SPIE, 8141, 814115 (2011).
- [107] IDL (Interactive Data Language), Research Systems, Inc., 2995 Wilderness Place, Suite 203, Boulder, CO, 80301.
- [108] X-Ray Server URL: <http://x-server.gmca.aps.anl.gov>

- [109] Stepanov, S., *X-ray server: an online resource for simulations of X-ray diffraction and scattering*, in: [*Advances in Computational Methods for X-ray and Neutron Optics*], Ed. M.Sanches del Rio, Proc. SPIE, 5536, 16-26 (2004).





# Declaration of Honor

I hereby declare that I prepared this thesis without impermissible help of third parties and that none other than the indicated tools have been used; all sources of information are clearly marked, including my own publications.

In particular I have not consciously:

- Fabricated data or rejected undesired results
- Misused statistical methods with the aim of drawing other conclusions than those warranted by the available data
- Plagiarized external data or publications
- Presented the results of other researchers in a distorted way

I am aware that violations of copyright may lead to injunction and damage claims of the author and also to prosecution by the law enforcement authorities.

I hereby agree that the thesis may be reviewed for plagiarism by means of electronic data processing.

This work has not yet been submitted as a doctoral thesis in the same or a similar form in Germany or in any other country. It has not yet been published as a whole.

München, 13.06.2020

Tanja Rosentreter